



UNIVERSITY OF
LIVERPOOL

Investigating Shape Coexistence and the Onset of
Deformation in the $A \approx 100$ Region with Laser
Spectroscopy

Thesis submitted in accordance with the requirements of
the University of Liverpool for the degree of Doctor in Philosophy
by

Charlie Stuart Devlin

November 16, 2021

Abstract

This thesis presents new measurements of the hyperfine splitting in the electronic structure for six nuclear states: ^{98m}Y , ^{99}Y , ^{100}Nb , ^{100m}Nb , ^{102}Nb and ^{102m}Nb . The measurements were taken over a week-long beam time at the IGISOL-IV facility at the University of Jvaskylä Accelerator Laboratory using the technique of high-resolution laser spectroscopy on a bunched, radioactive ion beam. Whilst held inside an ion cooler-buncher, the atomic energy state of the beam was manipulated, via the technique of optical pumping, such that spectroscopy could be performed from a metastable energy level. In all cases, this allowed for an unambiguous spin assignment of the nucleus and extraction of the magnetic dipole and electric quadrupole moments, as well as the difference in mean-square charge radii from a reference nucleus.

A remeasurement of ^{99}Y allowed for a recalibration of both the atomic F and M factors (used in the extraction of the mean-square charge radii) and the ratios of the hyperfine parameters for the atomic $J = 2 \rightarrow J = 1$ transition in yttrium. This in turn allowed for the spin assignment of ^{98m}Y to be confirmed as $I = 7$ and for a correction to the previously quoted values of the electromagnetic moments of the state, due to both the new spin value and a peak reassignment in the hyperfine structure of the $J = 0 \rightarrow J = 1$ atomic transition compared to the previous analysis. The complementary measurements of the spectroscopic quadrupole moment and the changes in mean-square charge radii allow for a full characterisation of the shape change and shape coexistence at ^{98}Y since they allow the extraction of the magnitude and sign of the deformation and a measure of its rigidity.

In the niobium chain, we present the first successful laser spectroscopic measurements of ^{100}Nb , the isotone of ^{98}Y , and its isomer. These measurements demonstrate that a shape coexistence is not present between these states as it is in ^{98}Y . Furthermore, the measurements show a high level of dynamic deformation in both of these states. After the shape change, two states of ^{102}Nb have also been measured for the first time through the technique of laser spectroscopy.

These states take on an prolate shape, compared with the oblate shape of ^{100}Nb and hence follow the trend of the onset of deformation observed at $N = 60$ (and in the prolate deformed isomer of ^{98m}Y). They do, however, maintain their dynamic nature, unlike the $N \geq 60$ isotopes in the Y chain.

Acknowledgements

First and foremost, my thanks go to my supervisor Professor Bradley Cheal without whom none of this would have been possible. Bradley: thanks for supporting me throughout my studies and for being so kind and generous with your time and knowledge. It has been a real pleasure to work with you these last four years.

I would also like to acknowledge the team at JYFL: Paul, Agi, Ruben, Sarina, Wouter, Iain and all the others at IGISOL, thanks for all you have done, the help you have given and the time we have spent together. Thanks also to Markus who performed the DFT calculations shown in this work. My gratitude extends to the COLLAPS collaboration too, it was an honour to work with and learn from a team of such great scientists.

Next, I would like to thank those of you who have made my time at Liverpool so great. My fellow PhD students with our coffees and crosswords, the Outreach team and the events we have run, and the societies I have been a part of (Re-enactment, Beekeeping and Postgrad) have all made my time as a student very special.

To my parents, Paula and Nick: thank you for supporting me in everything and for giving me every opportunity. I never could have got here without you.

Finally, my thanks to my girlfriend Ellie for her support, her kindness and for putting up with me talking about nuclear physics every day for four years. Thank you for being there for me all the way through.

In the beginning the Universe was created. This made a lot of people very angry and has been widely considered to be a bad move.

- *Douglas Adams*

Contents

Abstract	i
Acknowledgements	iii
List of Publications	xv
1 Introduction	1
2 Nuclear Theory	4
2.1 The Shell Model	5
2.2 The Magnetic Dipole Moment	7
2.3 Nuclear Deformation	10
2.3.1 Electric Quadrupole Moments	10
2.3.2 Nuclear Charge Radii	12
2.3.3 Nilsson Diagrams	13
2.3.4 Shape Coexistence	16
2.4 Modern Nuclear Theories	16
2.4.1 Energy Density Functional Calculations	18
3 Hyperfine Interaction	20
3.1 Hyperfine Splitting	21
Hyperfine Splitting due to the Magnetic Dipole Moment	21
Hyperfine Splitting due to the Electric Quadrupole Moment	22
3.1.1 Total Hyperfine Splitting	23
3.2 Transitions Between Hyperfine States	23
3.2.1 Hyperfine Selection Rules	24
3.2.2 Extracting Nuclear Spin	25
3.2.3 Extracting Nuclear Moments	26
3.3 Isotope Shift	27
3.3.1 The Mass Shift	28
3.3.2 The Field Shift	30
3.3.3 Total Isotope Shift	32
3.4 King Plot Technique	32

4	Laser Spectroscopy	35
4.1	Line Shapes	36
4.1.1	Homogeneous Line Broadening	36
4.1.2	Inhomogeneous Line Broadening	37
	Doppler Broadening	37
	Power Broadening	38
	Pressure Broadening	39
4.2	An Overview of the Technique of Laser Spectroscopy	39
4.2.1	Fast-Beam Collinear Laser Spectroscopy	39
4.2.2	Fitting Process	41
4.2.3	Other Forms of Laser Spectroscopy	44
5	The IGISOL Facility	46
5.1	IGISOL-IV	46
5.2	The IGISOL Method	46
5.2.1	The SPIG	47
5.2.2	Mass Separation	48
5.3	Stable Ion Source	49
5.4	The Ion Cooler-Buncher	50
5.5	Beam Optics	52
6	The Laser Spectroscopy Station	54
6.1	Light Collection Region	54
6.2	DAQ	55
6.2.1	Scanning Across Zero Tuning Volts	59
6.3	Laser Systems for Performing Spectroscopy	62
6.3.1	High-Precision Continuous Wave Lasers	62
	Unidirectional Device	64
	Mode selection	64
6.3.2	Laser Stabilisation	65
6.3.3	Pulsed Lasers	67
6.3.4	Second Harmonic Generation	67
7	Collinear Laser Spectroscopy of Yttrium Isotopes	69
7.1	Experimental Setup	73
7.2	Initial Predictions	75
7.3	Measurement of ^{98m}Y on the 321 nm Line	78
7.4	Remeasurement of ^{99}Y	82
7.5	Re-analysis of ^{98m}Y on the 321 nm Line	85
7.6	Extraction of Nuclear Properties	87
7.7	Calculating Deformation	90
7.8	Comparison to Energy Density Functional Calculations	92
7.9	Conclusions	95
8	Collinear Laser Spectroscopy of Niobium Isotopes	97

8.1	Setup	98
8.2	Preparatory Work	99
8.2.1	Revisiting the Previous Study of Niobium	99
8.2.2	Empirical Estimates	101
8.3	Measurement and Analysis	103
8.3.1	^{100}Nb	103
	Final Extraction of ^{100}Nb Hyperfine Parameters	106
8.3.2	^{102}Nb	107
	Final Extraction of ^{102}Nb Hyperfine Parameters	110
8.4	Nuclear Properties	111
8.5	Systematics of the $Z = 40$ Region	113
8.6	Conclusions	115
9	Summary and Future Work	117
9.1	Conclusion	117
9.2	Outlook	118
A	Potential Energy Surfaces From EDFs	121
	References	125

List of Figures

1.1	A chart of all known isotopes at the time of writing.	2
2.1	The Woods-Saxon, Harmonic Oscillator and Square Well potentials for a theoretical nucleus of diffuseness $a = 0.65$ fm and nuclear radius ($R = r_0 A^{1/3}$, $r_0 = 1.25$ fm) $R = 5.8$ fm.	6
2.2	An example of the ordering of nuclear shells before and after the spin-orbit correction. The nuclear magic numbers up to 126 are shown in the shell gaps.	7
2.3	A diagram depicting the system used to define the quadrupole moment. This figure is adapted from a figure in Ref [1]	11
2.4	An oblate ($Q_0 < 0$) shape and a prolate ($Q_0 > 0$) shape.	12
2.5	A Nilsson diagram for protons and neutrons below $Z, N = 50$	14
2.6	A Nilsson diagram for neutrons between $N = 50$ and $N = 82$	15
3.1	The splitting of atomic levels in ^{99}Y ($I = 5/2$) on a $J = 0 \rightarrow J = 1$ transition. Effects from magnetic and quadrupole interactions cause the splitting and shifting of energy levels.	24
3.2	A many-electron atom can experience a distribution of orbiting charge. Electrons may have momenta in the opposite (left) or the same (right) direction.	30
3.3	The electric potential a nucleus would experience from a Coulomb potential (red) and in the case of a spherical charge (blue).	31
4.1	The basic geometry of the laser-ion interaction in anti-collinear laser spectroscopy. Ions are accelerated to high velocities and meet the laser beam head on.	40
4.2	The effect of increasing the velocity on the velocity spread under electrostatic acceleration.	42
5.1	A diagram of the IGISOL-IV facility	47
5.2	A schematic of the IGISOL front end.	48
5.3	The potential throughout the cooler when the gate is raised and lowered according to the bunching signal being on or off.	51
6.1	A schematic of the laser spectroscopy line at JYFL in plan. *The Charge Exchange Cell is removable and is only present in the beam line during experiments in which spectroscopy takes place on the atom, rather than the ion.	55

6.2	An example linear calibration for a scan of ^{99}Y	56
6.3	An example of a time gate applied offline to data taken for ^{98}Y . Here, only data within the shaded region - corresponding to the time of flight of the ion bunch - is accepted. A large portion of data is disregarded since it contains only background counts.	58
6.4	The fitted values for the centroid for ^{98}Mo (an $I = 0$ state) as the scanning range is changed in voltage. Note that for some of these data points the scanning range crosses 0 V. The shaded region shows the weighted average value of the centroids and its appropriate error. . . .	59
6.5	The measured spectra of ^{95}Mo	61
6.6	The fitted values for the centroid and A_u values for ^{95}Mo as the scanning range is changed in voltage. For all data points except $V_{\text{scan}}=600$ V, the scanning range crosses 0 V.	62
6.7	The laser cavity of a Matisse 2 DS Dye Laser. This figure is based off the figure from the Matisse User's Guide	63
6.8	An example transmission profile of a reference cavity. The laser frequency can be 'locked' to the side of a transmission peak, shown in red.	66
7.1	The radii of the Y isotopic chain as previously measured. The dashed lines represent the expected charge radii for $\beta_2 = 0$ and $\beta_2 = 0.43$	70
7.2	The previously measured spectra of Y isotopes on the $J = 0 \rightarrow J = 1$ line. It is important to note the sudden shift in centroid between ^{98}Y and its isomer, clearly demonstrating the shape coexistence.	72
7.3	The pumping scheme for yttrium. Electrons are excited on the 363 nm line before relaxing in to the 3D_2 state for spectroscopy. All hyperfine parameters quoted are measured in MHz.	74
7.4	The calculated hyperfine spectra for ^{98m}Y for $I = 4 - 9$. It is clear that a confirmation of the nuclear spin is viable from the measurement of the left hand peak only.	77
7.5	The measured spectra of ^{98m}Y showing no discernable counts where the peak was expected to occur.	79
7.6	The previously measured ^{98m}Y spectrum from 2007.	80
7.7	A comparison of the measured hyperfine spectra for ^{98m}Y to the calculated spectra which replaces Figure 7.4. The result shows ambiguity in the nuclear spin, which could align with $I = 7$ or 8.	81

7.8	The previously measured ^{99}Y spectrum as measured on the 321 nm line. The blue stars indicate the approximate position of the two not yet fully measured peaks.	83
7.9	The previously measured ^{99}Y spectrum on the 321 nm line (a) compared to the 321 nm spectrum which was measured in late 2019 (b).	83
7.10	The King plot for the computation of the F and M factors of the 321 nm atomic transition.	84
7.11	The fully corrected simulation of the hyperfine structure of ^{98m}Y , created using the newly measured F and M factors and B ratio from ^{99}Y , all from this work. Solid vertical lines indicate the locations of the peaks.	86
7.12	The extracted nuclear parameters of ^{98m}Y for various nuclear spins as measured on two different atomic lines. The extracted parameters agree best for $I = 7$	88
7.13	The ratios of A parameters (a), B parameters (b) from the 3P_1 and 1P_1 states, and isomer shifts (c) for varying spins of ^{98m}Y on the 321 nm and the 363 nm lines, shown relative to the known ratios and gradient of the King plot.	89
7.14	The measured and expected change in charge radii for the yttrium chain. The difference between the two values shows the extent of dynamic deformation present in the nucleus. The values for ^{98m}Y presented here are a correction to the values in literature. The lower and upper dashed lines are the isodeformation lines for $\beta_2 = 0$ and $\beta_2 = 0.43$, respectively.	91
7.15	The charge radii of the Y chain compared to the theoretical predictions from DFT calculations.	93
7.16	The β_2 deformation parameter of the Y chain compared to the theoretical predictions from DFT calculations.	94
8.1	The chosen optical pumping scheme for niobium isotopes.	99
8.2	The previously measured spectrum of ^{93}Nb (black) with the new fit (red).	101
8.3	The measured data for $^{100,102}\text{Nb}$. Peaks identified with an l are from the low-spin state, with a h the high-spin state and the peak labelled with l, h contains a contribution from both states.	104

8.4	Assigning the spin of the low-spin state in ^{100}Nb . In Panel a) , the peaks are fit with a spectrum as generated with $I = 1$. Panel b) shows the same measured spectrum, only fit with $I = 2$. It is evident that all peaks cannot be fit simultaneously unless $I = 1$. Note that in Panel b) , the intensity of the left-most peak has been manually increased from the fitted value to demonstrate its position.	105
8.5	Assigning the spin of the high-spin state in ^{100}Nb where the peak indicated by a blue star contains a contribution from the low-spin state. In Panel a) , the peaks are fitted with a spectrum as generated with $I = 6$. Panel b) shows the same measured spectrum, only fitted with $I = 5$ and Panel c) with $I = 4$. It is evident that all peaks cannot be fit simultaneously unless $I = 5$. Note that in Panels a) and c) , the intensity of the right-most peak has been manually increased from the fitted value to demonstrate its position.	107
8.6	Examples of measured peaks of both states in ^{100}Nb and their fits. The example structures underneath are calculated from Racah intensities to show the locations of the peaks of each structure.	108
8.7	The measured spectrum of ^{102}Nb and the fitted spectra for $I = 1$ and $I = 2$. Panel b) shows the fit when $I = 2$, the inset shows the location of the leftmost peak has not been correctly fit. It is important to note that the intensity of this peak has been manually increased from the fitted value as a demonstration of its location.	109
8.8	The measured spectrum of ^{102m}Nb and the fitted spectra for $I = 4$ (Panel a)) and $I = 5$ (Panel b)). It is important to note that the intensity of the leftmost red peak in Panel b) has been manually increased from the fitted value as a demonstration of its location, whereas intensities of the other peaks are taken from the fitting routine. The spectrum also includes one peak from the $I = 1$ state which overlaps in frequency which is signified by a blue star.	111
8.9	Examples of measured peaks of both states in ^{102}Nb and their fits. The example structures underneath are calculated from Racah intensities to show the locations of the peaks of each structure.	112
8.10	The measured charge radii of the Nb isotopes compared to the values expected from the liquid drop model. The lower and upper dashed black lines represent the isodeformation lines for $\beta_2 = 0$ and $\beta_2 = 0.4$ respectively.	114
8.11	The measured charge radii of isotopic chains in the $Z = 40$ region.	115

A.1	The potential energy surface with respect to the deformation parameter β_2 for $^{78-108}\text{Zr}$ as calculated by the $\text{Fy}(\Delta r, \text{HFB})$ functional.	122
A.2	The potential energy surface with respect to the deformation parameter β_2 for $^{78-108}\text{Zr}$ as calculated by the UNEDF0 functional.	122
A.3	The potential energy surface with respect to the deformation parameter β_2 for $^{78-108}\text{Zr}$ as calculated by the UNEDF2 functional.	123
A.4	The potential energy surface with respect to the deformation parameter β_2 for $^{74-104}\text{Sr}$ as calculated by the $\text{Fy}(\Delta r, \text{HFB})$ functional.	123
A.5	The potential energy surface with respect to the deformation parameter β_2 for $^{74-104}\text{Sr}$ as calculated by the UNEDF0 functional.	124
A.6	The potential energy surface with respect to the deformation parameter β_2 for $^{74-104}\text{Sr}$ as calculated by the UNEDF2 functional.	124

List of Tables

7.1	A table of the fitted hyperfine parameters for ^{98m}Y on the 363 nm $^1S_0 \rightarrow ^1P_1$ transition for nuclear spins ranging from $I = 4 - 9$. Hyperfine parameters are quoted in MHz.	76
7.2	The fitted values for all six permutations of the peaks (the spectrum on which these fits were performed is shown in Figure 7.6) for a spin of $I = 7$ as suggested by Urban <i>et al.</i> , possibilities for other spins with Scenario d) can be found in Table 7.3. The ν values are relative to an arbitrary constant. Peak 0 represents the $F = 7 \rightarrow F = 6$ transition, Peak 1 represents the $F = 7 \rightarrow F = 7$ and Peak 2: $F = 7 \rightarrow F = 8$. . .	80
7.3	The newly fitted hyperfine parameters for ^{98m}Y on the 363 nm $^1S_0 \rightarrow ^1P_1$ transition which replaces Table 7.1. All hyperfine parameter values are quoted in MHz.	81
7.4	The previously and newly measured hyperfine parameters of ^{99}Y . All values for hyperfine parameters are in MHz.	84
7.5	LHS: The fitted hyperfine parameters of ^{98m}Y for possible spins $I = 6 - 9$ for measurements on the 321 nm line. RHS: The parameters calculated for the 321 nm line from the measurements taken on the 363 nm line (with updated calibration) and the known ratios of hyperfine parameters. All hyperfine values are quoted in MHz.	86
7.6	The newly extracted hyperfine parameters of the upper states in ^{98m}Y on the 363 nm and 321 nm lines from this work. The isotope shift for ^{98m}Y is measured against its ground state.	87
7.7	The measured nuclear properties of ^{98m}Y . The spectroscopic quadrupole moment of ^{90}Y acted as a reference for the value extracted for ^{98m}Y . . .	88
8.1	The measured hyperfine parameters in ^{93}Nb . The errors shown are derived from the statistical errors which are taken from the fitting process.	100
8.2	The measured hyperfine ratios for the high-spin state in ^{100}Nb , the errors shown are derived from the statistical errors from the fitting process. The known values are $A_l/A_u = -0.9610(1)$ and $B_l/B_u = +0.440(22)$	106
8.3	The measured hyperfine parameters for ^{100}Nb . The errors shown are derived from the statistical errors from the fitting process. The hyperfine parameters for the lower atomic state can be extracted from the fixed ratios of $A_l/A_u = -0.9610(1)$ and $B_l/B_u = +0.440(22)$	106

8.4	The measured hyperfine ratios for the high-spin state in ^{102}Nb . The errors shown are derived from the statistical errors from the fitting process. The known values are $A_l/A_u = -0.9610(1)$ and $B_l/B_u = +0.440(22)$	108
8.5	The measured hyperfine parameters for ^{102}Nb . The errors shown are derived from the statistical errors from the fitting process. The hyperfine parameters for the lower atomic state can be extracted from the fixed ratios of $A_l/A_u = -0.9610(1)$ and $B_l/B_u = +0.440(22)$	110
8.6	The nuclear moments for Nb extracted from the hyperfine parameters of its atomic states. The errors shown are derived from the statistical errors from the fitting process and the quoted error on the reference values of $\mu_{93} = +6.1705(3) \mu_N$, $Q_{s,93} = -0.32(2) \text{ b}$, $A_{u,93} = +1197.5(2) \text{ MHz}$ and $B_{u,93} = +52.9(8) \text{ MHz}$	112

List of Publications

- **C.S. Devlin**, O. Beliuskina, P. Campbell, L. Canete, B. Cheal, C. Delafosse, T. Eronen, S. Geldhof, W. Gins, R.P. de Groote, A. Jokinen, Á. Koszorús, M. Laatiaoui, R. Mathieson, I.D. Moore, M. Reponen, S. Rinta-Antila, A. de Roubin, and S. Zardvornaya. New studies on the shape transition at $N \approx 60$ and shape co-existence in ^{98}Y . *Manuscript in preparation*
- H. Heylen, **C.S. Devlin**, W. Gins, M.L. Bissell, K. Blaum, B. Cheal, L. Filippin, R.F. Garcia Ruiz, M. Godefroid, C. Gorges, J.D. Holt, A. Kanelakopoulos, S. Kaufmann, Á. Koszorús, K. König, S. Malbrunot-Ettenauer, T. Miyagi, R. Neugart, G. Neyens, W. Nörtershäuser, R. Sánchez, F. Sommer, L.V. Rodríguez, L. Xie, Z.Y. Xu, X.F. Yang and D.T. Yordanov. High-resolution laser spectroscopy of $^{27-32}\text{Al}$. *Physical Review C*. 103:014318, 2021
- R.P. de Groote, A. de Roubin, P. Campbell, B. Cheal, **C.S. Devlin**, T. Eronen, S. Geldhof, I.D. Moore, M. Reponen, S. Rinta-Antila, and M. Schuh. Upgrades to the collinear laser spectroscopy experiment at the IGISOL. *Nuclear Instruments and Methods in Physics Research Section B: Beam Interactions with Materials and Atoms*, 463:437 - 440, 2020.
- A. Kanellakopoulos, X.F. Yang, M.L. Bissell, M.L. Reitsma, S.W. Bai, J. Billowes, K. Blaum, A. Borschevsky, B. Cheal, **C.S. Devlin**, R. F. Garcia Ruiz, H. Heylen, S. Kaufmann, K. König, Á. Koszorús, S. Lechner, S. Malbrunot-Ettenauer, R. Neugart, G. Neyens, W. Nörtershäuser, T. Ratajczyk, L.V. Rodríguez, S. Sels, S.J. Wang, L. Xie, Z.Y. Xu, and D.T. Yordanov. Nuclear moments of germanium isotopes near $N = 40$. *Physical Review C*. 102:054331, 2020.
- Á. Koszorús, L.J. Vormawah, R. Beerwerth, M.L. Bissell, P. Campbell, B. Cheal, **C.S. Devlin**, T. Eronen, S. Fritzsche, S. Geldhof, H. Heylen, J.D. Holt, A. Jokinen, S. Kelly, I.D. Moore, T. Miyagi, S. Rinta-Antila, A. Voss,

C. Wraith. Proton-neutron pairing correlations in the self-conjugate nucleus ^{42}Sc . *Physics Letters B.*, 819:136439, 2021.

- S. Lechner, Z.Y. Xu, M.L. Bissell, K. Blaum, B. Cheal, G. De Gregorio, **C.S. Devlin**, R.F. Garcia Ruiz, A. Gargano, H. Heylen, P. Imgram, A. Kanelakopoulos, Á. Koszorús, S. Malbrunot-Ettenauer, R. Neugart, G. Neyens, W. Nörtershäuser, P. Plattner, L.V. Rodríguez, X.F. Yang, D.T. Yordanov. Probing the single-particle behaviours above ^{132}Sn via electromagnetic moments of $^{133,134}\text{Sb}$ and $N = 82$ isotones. *Physical Review C.* 104:014302, 2021
- M. Reponen, R.P. de Groote, L. Al Ayoubi, O. Beliuskina, M.L. Bissell, P. Campbell, L. Cañete, B. Cheal, K. Chrysalidis, C. Delafosse, A. de Roubin, **C.S. Devlin**, T. Eronen, R.F. Garcia Ruiz, S. Geldhof, W. Gins, M. Hukkanen, P. Imgram, A. Kankainen, M. Kortelainen, Á Koszorús, S. Kujanpää, R. Mathieson, I.D. Moore, D.A. Nesterenko, I. Pohjalainen, M. Vilén, and A. Zadvornaya. Evidence of a sudden increase in the nuclear size of proton-rich silver-96. *Nature Communications*, 12(1):4596, 2021
- S. Geldhof, M. Kortelainen, O. Beliuskina, P. Campbell, L. Caeres, L. Cañete, B. Cheal, K. Chrysalidis, **C.S. Devlin**, R.P. de Groote, T. Eronen, Z. Ge, W. Gins, Á Koszorús, D. Nesterenko, A. Ortiz-Cortes, I. Pohjalainen, I.D. Moore, A. Raggio, M. Reponen, J. Romero, A. de Roubin and F. Sommer. Impact of nuclear deformation and pairing on the charge radii of palladium isotopes. *Manuscript in preparation*.

Chapter 1

Introduction

The study of nuclear physics is an investigation into the forces that govern the interaction between the protons and the neutrons inside of an atom. As several bodies are introduced into this system, the calculations required to solve it become increasingly complex. To ease this complexity, many theories have been developed in order to calculate nuclear properties with a finite amount of computing power. To test these theories across the nuclear chart, it is critical to gather as much information on the nuclear landscape as possible. In particular, the technique of laser spectroscopy gives access to model-independent measurements of the nuclear magnetic moment, the sign and magnitude of the spectroscopic quadrupole moment, the change in mean-square charge radius (relative to another isotope) and, in many cases, can unambiguously assign the nuclear spin [2]. Measuring these quantities therefore provides an excellent benchmark for many nuclear theories.

To date, over 3000 nuclei have been discovered (with nearly 2000 isomeric states) [3], but only a few hundred of these are stable (Figure 1.1). Since many of these radioactive nuclei live for only a few short moments, they must first be produced at radioactive isotope factories, or by reactions with stable beams, before they can be measured. Many such facilities exist around the world and have made

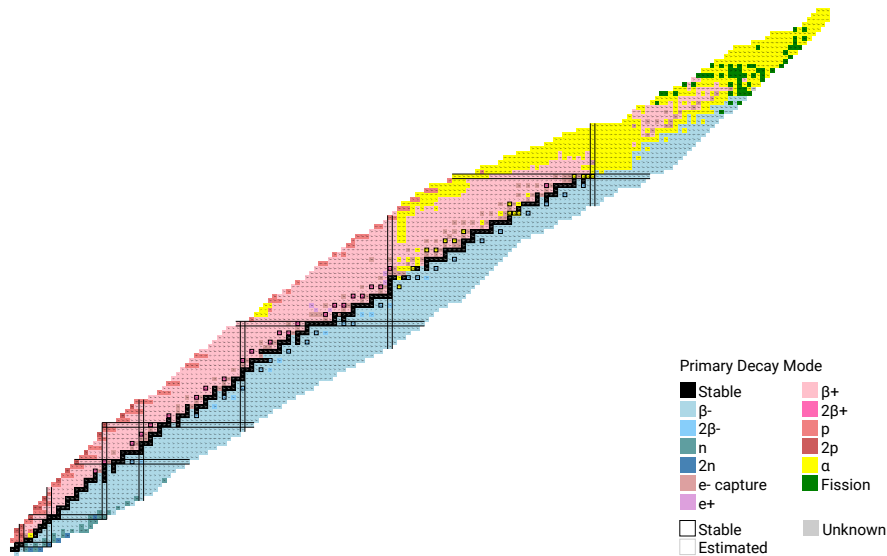


FIGURE 1.1: A chart of all known isotopes at the time of writing [4].

great progress in developing techniques to produce large enough quantities of nuclei across the nuclear chart that they can be measured. Of particular importance to this work is the development of the radioactive ion beam (RIB) facility. RIB facilities enable not only the production of these short-lived states but also the ability to form them into a beam and transport them across an experimental hall, through various types of apparatus (such as mass-selecting magnets, ion coolers, purification traps, charge breeders and more) and deliver them to a detection station for their measurement. The technique is particularly beneficial to collinear laser spectroscopy since formation into a beam allows the ions to be accelerated to high speeds and reduces the width of the measured hyperfine line shapes due to a decrease in Doppler broadening. The use of ion bunchers also means that ions can be delivered to the spectroscopy station in discrete packets, allowing for measurements to be time correlated with the arrival of the bunch. This method allows for a background reduction factor of $\approx 10^4$, hence permitting the measurement of nuclei which cannot be produced at high rates.

Nuclear structure studies across the nuclear landscape, taken at many facilities around the globe, have shed light on many new effects in these nuclear systems

such as halo nuclei [5], proton emitters [6] and highly deformed states [7]. This work focuses on an effect called shape coexistence wherein several competing energy levels of the same nucleus can take on vastly different shapes. The shape coexistence in the system of ^{98}Y ($Z = 39, N = 59$) was first measured in a study which took place around 2007 at the IGISOL facility, located at the JYFL Accelerator Laboratory, Jyväskylä, Finland [8]. The study showed a large jump in the measured isotope shift of the hyperfine structure between the ground state and its isomer, indicative of a large shape change. Unfortunately, this work was unable to measure the nuclear spin due to the use of a $J = 0 \rightarrow J = 1$ atomic transition and so the values of the nuclear properties could only be extracted using either one of the alternative spins suggested in literature at the time. This work provides a new measurement of ^{98}Y using a different atomic transition and confirming a new spin assignment (Chapter 7). From this, the nuclear properties are extracted and compared to theoretical calculations from Energy Density Functional theory. To further investigate the region, measurements of the neighbouring niobium chain have also been taken. In particular, ^{100}Nb , the isotone of ^{98}Y , and its low lying isomeric state have been measured to see if this phenomenon also occurs in this system (Chapter 8).

Chapter 2

Nuclear Theory

In the early days of atomic structure physics, J.J. Thompson proposed that the atom consisted of a ball of positive charge mixed in with other, negatively charged particles (electrons). The famous ‘plum pudding’ model of the atom was among one of the most popular until Ernest Rutherford (alongside Geiger and Müller at the University of Manchester) proposed an experiment to probe the structure of the atom by firing a beam of alpha particles at a sheet of gold foil. In perhaps one of the most startling discoveries of the 20th century, Rutherford discovered that the particles did not travel directly through the foil (as they would if the atom were indeed a ‘plum pudding’) but, in fact, many recoiled at multiple angles including straight back to the source. It was from these findings that Rutherford postulated the existence of the ‘nucleus’ of an atom that constituted a bulk of its mass and all of its positive charge with the negative electrons orbiting far away [9].

Not long after, James Chadwick discovered the existence of the neutron by measuring the recoil products of collisions between alpha particles and many light nuclei [10]. At a similar time, the first attempts were made to describe the forces within a nucleus by comparing it to a liquid drop. The liquid drop model (first proposed by Gamow [11]) considered the attraction between nucleons from a strong force and repulsion from the Coulomb force within the body of the nucleus as well

as the difference in those terms at the surface where nucleons are not fully surrounded. Furthermore, the liquid drop model accounts for the difference between protons and neutrons by means of an asymmetry term which accounts for protons and neutrons filling different shells as they are added to the nucleus. Perhaps most importantly, the model included an interaction due to the pairing between the nucleons. Whilst this theory was an important step in the direction of understanding the nucleus, it could not explain the stability of the ‘magic’ nuclei. In order to reproduce these, Maria Goeppert-Meyer suggested the shell model of atomic nuclei [12].

2.1 The Shell Model

The prevailing theory in nuclear physics is the shell model. In this picture, nuclei inhabit orbitals in much the same way as atomic electrons do where each orbital has a set occupancy defined by a set of quantum numbers. The energy of each nuclear shell is computed from a mean-field potential with both surface and spin-orbit corrections. Calculations of this type are known to accurately describe the so-called ‘magic numbers’ where effects such as an increase in two-neutron separation energy, nuclei taking on more spherical shapes and, in some cases, an increase in natural abundance of specific nuclei occur. The known nuclear magic numbers are 2, 8, 20, 28, 50 and 82 (as well as 126 for neutrons). Various forms of the mean-field potential exist, the most realistic being the Woods-Saxon potential. Unfortunately, the Woods-Saxon potential does not allow an analytical calculation and so other potentials must be used for such purposes. Commonly utilised potentials for these purposes are the square well potential and the harmonic oscillator potential, a comparison of which may be found in Figure 2.1.

In parallel with atomic physics, the nuclear shells are labelled with ‘spectroscopic notation’. In this way, each state can be referred to uniquely whilst giving

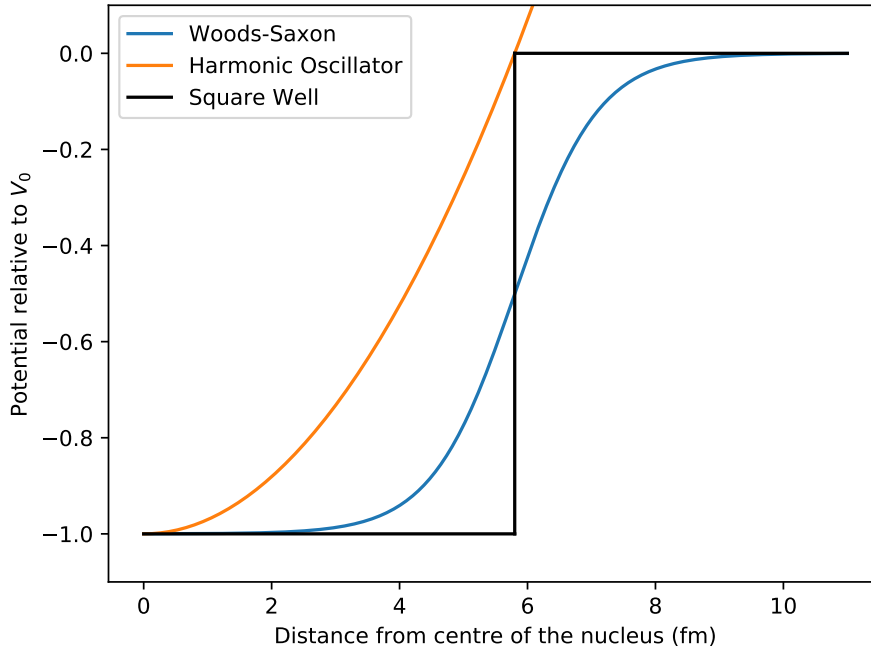


FIGURE 2.1: The Woods-Saxon, Harmonic Oscillator and Square Well potentials for a theoretical nucleus of diffuseness $a = 0.65$ fm and nuclear radius ($R = r_0 A^{1/3}$, $r_0 = 1.25$ fm) $R = 5.8$ fm.

all the information that describes the quantum state. Such a label is written in the form Nl_j , where N is the principal quantum number (which is commonly omitted), l is the orbital angular momentum and j is the spin. The value of l is, by convention, noted by letters rather than numbers. The first four momenta are denoted by s ($l = 0$), p ($l = 1$), d ($l = 2$) and f ($l = 3$) which stand for *sharp*, *principal*, *diffuse* and *fundamental* respectively, echoing their atomic origins, and orbitals of higher values of l continue in alphabetical order.

It can be seen, however, that the mean-field potential does not by itself reproduce the observed nuclear magic numbers. Additional terms such as the spin-orbit term and the surface correction term must be added in order to complete the model. Analogous once again to the spin-orbit interaction observed in atomic structure (causing the fine structure of the atom), the nuclear spin-orbit term is generated from the spin \vec{s} of the nucleon and its angular momentum \vec{l} . The total

angular momentum is then $\vec{j} = \vec{l} + \vec{s}$. The expectation value of the product of \vec{l} and \vec{s} is given by $\langle \vec{l} \cdot \vec{s} \rangle = \frac{\hbar^2}{2} [j(j+1) - l(l+1) - s(s+1)]$ and the occupation of each level is $2j + 1$. This correction causes a splitting of the energy states as can be seen in Figure 2.2.

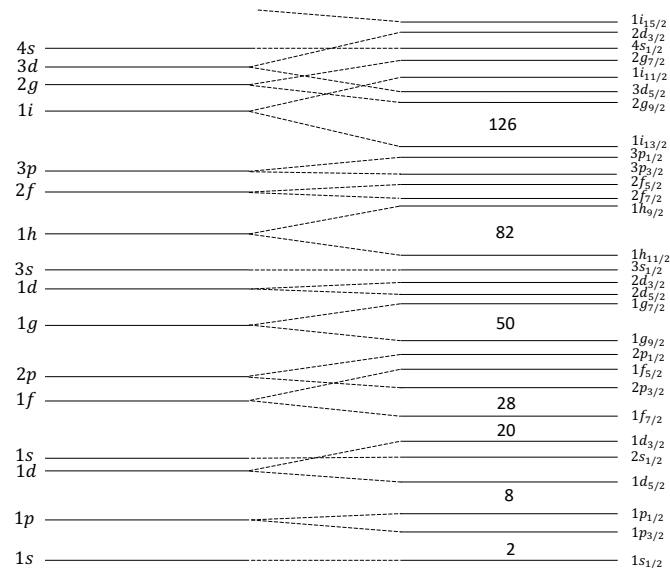


FIGURE 2.2: An example of the ordering of nuclear shells before and after the spin-orbit correction. The nuclear magic numbers up to 126 are shown in the shell gaps. This figure is based off a figure in Ref. [1].

2.2 The Magnetic Dipole Moment

A magnetic moment is, in a classical sense, caused by the movement of charge in a loop. Inside the nucleus, protons move through the nuclear volume creating a contribution to the nuclear magnetic moment. The nucleus, however, is a quantum object with spin, a phenomenon that does not exist in the classical picture and through this both protons and neutrons contribute further towards the total nuclear magnetic moment.

By first considering only the angular momentum of a proton, the magnetic moment is defined as

$$\mu = \frac{e\hbar}{2m}\ell, \quad (2.1)$$

where ℓ is the angular momentum of the nucleonic orbit. The quantity $\frac{e\hbar}{2m}$ is named the ‘magneton’ and, with m as the mass of a proton, the ‘nuclear magneton’ can be defined as $\mu_N = 3.1525 \times 10^{-8}$ eV/T and is adopted as a unit of measurement for the magnetic moment.

In a more useful form, Equation 2.1 may be written as

$$\mu = g_\ell \ell \mu_N, \quad (2.2)$$

where g_ℓ is the ‘free g-factor’ for a free nucleon in orbit. g_ℓ is defined as 1 for a proton and 0 for a neutron. In the case of a bound system, an ‘effective g-factor’ is introduced which accounts for changes created by such a system [1].

By continuing the image of the magnetic moment to analogously contain a contribution from the intrinsic spin of the nucleon, the magnetic moment of a nucleon can be expressed by

$$\vec{\mu} = (g_\ell \vec{\ell} + g_s \vec{s}) \mu_N, \quad (2.3)$$

where g_s is the ‘spin g-factor’ and \vec{s} is the spin of the nucleon [13]. The summation of the magnetic moments of all nucleons within the nucleus gives us the overall magnetic moment

$$\mu_I = g_I I \mu_N, \quad (2.4)$$

where μ_I is the nuclear magnetic dipole moment, g_I is the g-factor of the nucleus and I is the maximum projection of $\vec{I} = \sum_i \vec{j}_i = \sum_i \vec{l}_i + \vec{s}_i$, the sum of all total

angular momenta of the nucleons.

In the simple case of a single bound proton outside of an inert core the only contribution to the overall magnetic moment is the moment of the unbound nucleon and so the magnetic moment of the nucleus can be described by

$$\mu = \begin{cases} j - \frac{1}{2} + \mu_p, & \text{if } j = l + \frac{1}{2}, \\ \frac{j}{j+1} \left(j + \frac{3}{2} - \mu_p \right), & \text{if } j = l - \frac{1}{2}. \end{cases} \quad (2.5)$$

Likewise, for a single bound neutron

$$\mu = \begin{cases} \mu_n, & \text{if } j = l + \frac{1}{2}, \\ -\frac{j}{j+1} \mu_n, & \text{if } j = l - \frac{1}{2}. \end{cases} \quad (2.6)$$

Here, the values μ_p and μ_n are the free proton and neutron moments, respectively. Using their accepted values $\mu_p = +2.793\mu_N$ and $\mu_n = -1.913\mu_N$, one may calculate the so called ‘Schmidt moments’ which are first-order approximations to the magnetic moment [14]. Within the many-body nucleus, effects from the other particles which are present cause changes to the Schmidt moments and therefore the magnetic moment becomes much more difficult to calculate.

Estimating the magnetic moment for an odd-odd nucleus (which contains both unpaired protons and unpaired neutrons) is a non-trivial task. In the cases where the magnetic moment is known from experimental measurements for the lone proton and lone neutron which occupy the orbits in question, an empirical calculation of the magnetic moment of a nucleus with spin I may be performed using [14]

$$\mu(I) = \frac{I}{2} \left[\frac{\mu(I_\pi)}{I_\pi} + \frac{\mu(I_\nu)}{I_\nu} + \left(\frac{\mu(I_\pi)}{I_\pi} - \frac{\mu(I_\nu)}{I_\nu} \right) \frac{I_\pi(I_\pi + 1) - I_\nu(I_\nu + 1)}{I(I + 1)} \right], \quad (2.7)$$

where $\mu(I_\pi)$ and I_π are the magnetic moment and spin of the nucleus containing the lone proton respectively and $\mu(I_\nu)$ and I_ν are that of the nucleus with the lone neutron.

2.3 Nuclear Deformation

2.3.1 Electric Quadrupole Moments

In all but a few particular cases (for example at the so-called magic numbers), the nucleus assumes a non-spherical shape. The ‘electric quadrupole moment’ is a measure of this shape and contains information on its geometry and the scale of non-sphericity.

For a point at a sufficiently large distance from the nuclear volume, the electric potential generated by the nucleus may be described by [1]

$$V(\vec{r}) = \frac{1}{4\pi\epsilon_0} \int_V \frac{\rho(\vec{r}')}{|\vec{r} - \vec{r}'|} dv', \quad (2.8)$$

where $\rho(\vec{r}')$ is the nuclear charge density, \vec{r} is the vector from the origin to the point of observation and \vec{r}' is the vector from the origin to a point on the charge distribution as seen in Figure 2.3. An expansion of the quantity $\frac{1}{|\vec{r} - \vec{r}'|}$ gives the form of the electric potential as

$$V(\vec{r}) = \frac{1}{4\pi\epsilon_0} \left[\frac{1}{r} \int \rho(\vec{r}') dv' + \frac{1}{r^2} \int \rho(\vec{r}') r' \cos(\theta) dv' + \frac{1}{r^3} \int \rho(\vec{r}') r'^2 \frac{1}{2} (3 \cos^2(\theta) - 1) + \dots \right]. \quad (2.9)$$

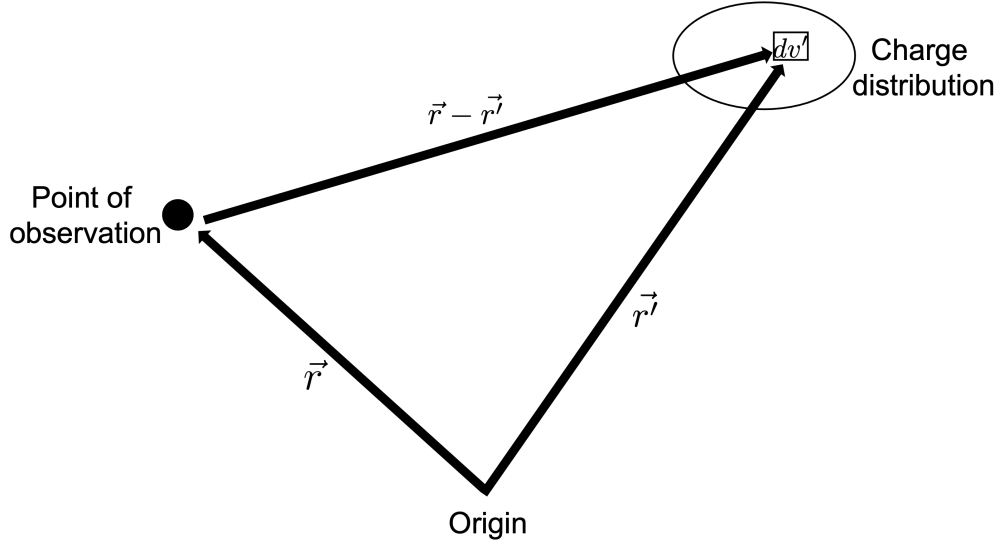


FIGURE 2.3: A diagram depicting the system used to define the quadrupole moment. This figure is adapted from a figure in Ref [1]

Due to the symmetry of nuclei, the second term in Equation 2.9 vanishes over an infinite integral since the integral is an odd function of the coordinates. The first integral is simply the total charge Ze . The electric quadrupole moment is then defined as

$$eQ_0 = \int \rho(\vec{r}') r'^2 (3 \cos^2(\theta) - 1) dv', \quad (2.10)$$

which, by choice of reference axis (choosing to measure the angle θ between \vec{r} and \vec{r}' from the axis corresponding to the maximum projection of spin), may be expressed as

$$eQ_0 = \int \rho(\vec{r}') (3z^2 - r'^2) dv', \quad (2.11)$$

where Q_0 is known as the ‘intrinsic quadrupole moment’ and z is the distance along the axis of symmetry. Should Q_0 be exactly zero, the nucleus takes a spherical shape. Otherwise, the shape may either be prolate ($Q_0 > 0$) or oblate ($Q_0 < 0$) as shown in Figure 2.4 [1].

The intrinsic quadrupole moment, however, cannot be directly measured through experimental means. Instead, the technique of laser spectroscopy probes a quantity

named the ‘spectroscopic quadrupole moment’, a quantity which will be discussed in more detail later in this work.

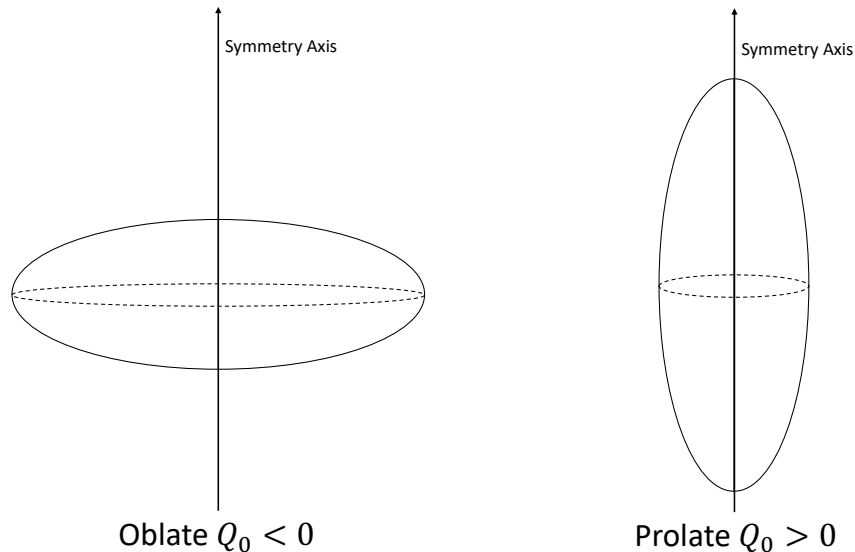


FIGURE 2.4: An oblate ($Q_0 < 0$) shape and a prolate ($Q_0 > 0$) shape.

2.3.2 Nuclear Charge Radii

The nuclear mean-square charge radius is a property of the nucleus which contains information of its size and shape. It is defined in terms of the nuclear charge density $\rho(\vec{r})$ and integrating across the nuclear volume v as [15]

$$\langle r^2 \rangle = \frac{\int \rho(\vec{r}) r^2 dv}{\int \rho(\vec{r}) dv}. \quad (2.12)$$

A point on the surface of a deformed nucleus may be described by

$$R(\theta, \phi) = R_{\text{av}} \left(1 + \sum_{i=2}^{\infty} \beta_i Y_0^i(\theta, \phi) \right), \quad (2.13)$$

where R_{av} is the average value of R and Y_0^i are the spherical harmonics. The terms β_i ensure volume conservation and as such are parameters including information on the deformation. Of particular interest to this work is β_2 which describes the

quadrupole deformation and is defined as $\beta_2 = \frac{4}{3} \sqrt{\frac{5}{\pi}} \frac{\Delta R}{R_{av}}$ where ΔR is the difference between the semimajor and semiminor axes of the ellipse [1].

For a nucleus which is deformed away from sphericity, the mean-square charge radius can be parametrised by [2]

$$\langle r^2 \rangle = \langle r_{sph}^2 \rangle \left(1 + \frac{5}{4\pi} \sum_{i=2}^{\infty} \langle \beta_i^2 \rangle \right) + 3\sigma^2, \quad (2.14)$$

where $\langle r_{sph}^2 \rangle$ is the mean-square charge radius of a spherical nucleus with the same volume and σ is the nuclear diffuseness parameter (approximately 0.99 fm). Equation 2.14 shows that there are two contributions towards the size of the nucleus.

Firstly, as the size increases (by adding more nucleons) the volume will be expected to increase similarly. Secondly, the appearance of the $\langle \beta_i^2 \rangle$ terms shows that should nuclear deformation increase, so too will the mean-square charge radius of the nucleus.

2.3.3 Nilsson Diagrams

The shell model discussed so far is only applicable for nuclei in which deformation is low. When deformation becomes more substantial, the mean-field potential must be modified in order to account for the anisotropy introduced by the nuclear shape. The Nilsson diagram (see Figures 2.5 and 2.6) shows the change in shell model energy levels for varying deformations. Where deformation, given in Figures 2.5 and 2.6 only by the parameter ϵ_2 , is zero, the standard shell model can be seen. However, as deformation is increased, degeneracies from the shell model are lifted as the levels split, though they still retain a two-fold degeneracy.

More than this, as the deformation increases energy levels can shift dramatically causing not only a change in the order of the states but in some cases a

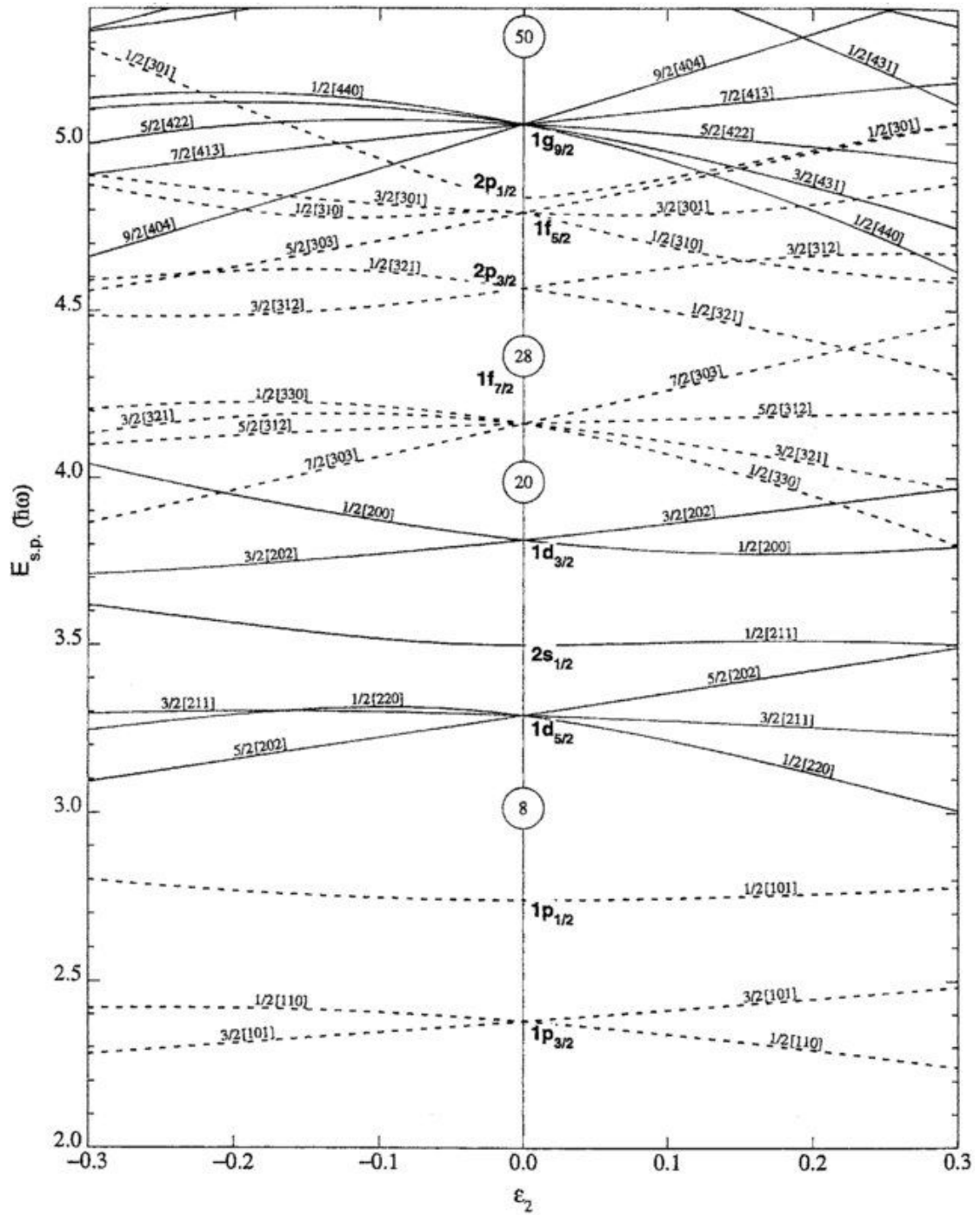


FIGURE 2.5: A Nilsson diagram for protons and neutrons below $Z, N = 50$ [16].

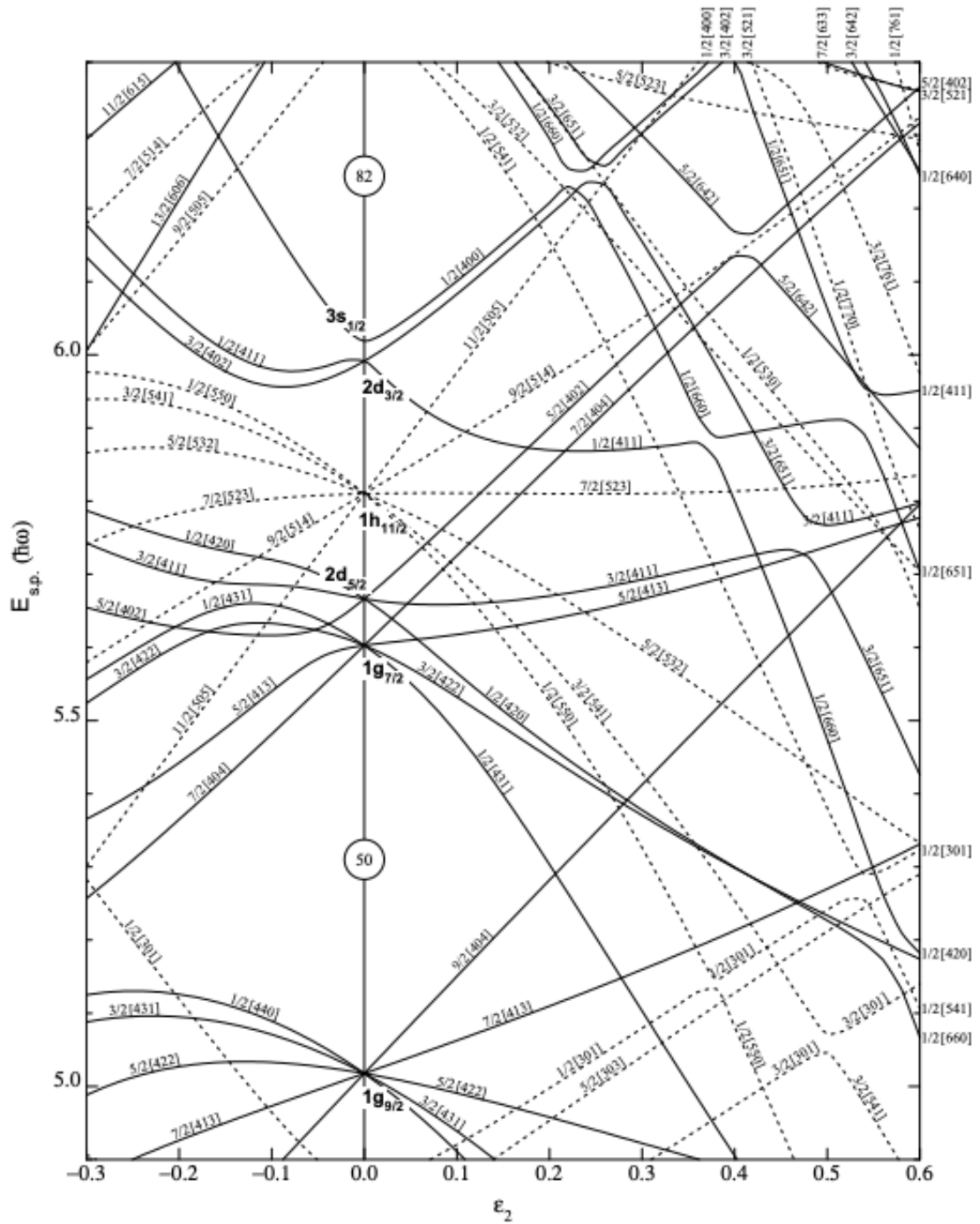


FIGURE 2.6: A Nilsson diagram for neutrons between $N = 50$ and $N = 82$ [17].

change in the nuclear magic numbers due to large increases (enough to create new shell gaps) or decreases (enough to close the shell gaps) in the state's energy. The new gaps caused by the raising and lowering of these levels can become large enough that new shell effects appear.

2.3.4 Shape Coexistence

Of particular interest to this work is an effect named shape coexistence. This phenomenon occurs when two or more states in a nucleus existing at different excitation energies take on vastly different shapes. Such a transition is indicative of a large reconfiguration of the constituent nucleons and cannot thus far be fully explained by nuclear theory [18]. Perhaps one of the most widely used examples of the phenomenon is the shape coexistence studied in ^{186}Pb which exhibits three competing energy states with spherical, oblate and prolate shapes, explained by three minima in the potential-energy surface [19]. Whilst it was originally thought to occur in specific areas of the nuclear chart, it is now postulated that shape coexistence may occur in all nuclei, though there are many in which it is yet to be observed [18].

2.4 Modern Nuclear Theories

As the nuclear chart has been measured more widely, many phenomena have been measured which cannot be explained by simple nuclear models. To improve our understanding of the nuclear force, many new techniques for calculating the properties of the nucleus have been proposed. One such technique is the interacting shell model. In this model, nucleons in one orbital are allowed to interact with those in another, leading to the attraction and repulsion of states. In this picture, the nucleons are no longer treated independently of each other but instead the

population of each shell may have a resounding effect on the energies of another [20]. To calculate these energies, one may make use of a so-called ‘model space’ in which the orbitals that have the greatest influence on the nucleus are chosen. Ideally, such a model space would lie atop a doubly magic nucleus which acts as a core. The core is expected to contribute minimally to the properties of the nucleus and hence make the calculation much less computationally demanding. As nuclei get further away from the core, the addition of more nuclear orbitals in the model becomes more complicated and hence this technique is poorly suited to nuclei that lie away from closed shells.

As computing power increases, ‘*ab-initio*’ theories become more widely accessible to different regions of the nuclear chart. These theories aim to solve the nuclear many-body problem by treating each nucleon as a fundamental degree of freedom through the use of effective field theories. With infinite computing power, it could be expected that such calculations would show remarkable agreement with experimentally measured nuclear properties. In practice however, truncation of operators is necessary. In order to make computation viable, the model independence of nuclear properties measured by certain experimental techniques is therefore of great importance to the development of such theories since they allow for the study of these operators and the extent to which they can be approximated [21].

Due to the increase in complexity of *ab-initio* calculations with the addition of extra nucleons, they were initially limited to the computation of nuclear parameters only at the lowest masses. The development of the Similarity Renormalisation Group has, at first, allowed access to nuclear properties of light magic nuclei and, later, to the nuclei surrounding these regions. Most recently, the developments of *ab-initio* shell model calculations has vastly increased the range of the technique and allowed for calculations of nuclear properties as high as the Sn ($Z = 50$) region

[22].

One other possible method of solving the nuclear many-body problem is the use of energy density functionals. In such a calculation, the energy of a many-fermion system can be written as a functional of the fermion density. This density is in turn described by the single-particle wave functions of each of the fermions present in the system [23]. The interactions between these states are usually described by some effective nucleon-nucleon interaction with free parameters which require inputs acquired from fits to experimental data such as binding energies, charge radii and surface thicknesses [24]. The aim of these energy density functional calculations is to develop a functional theory that is applicable across the whole nuclear chart.

2.4.1 Energy Density Functional Calculations

In Nuclear Density Functional Theory, the energy of a nucleus is described by its energy density through [25]

$$E = \int \mathcal{H}(\vec{r}) d^3\vec{r}, \quad (2.15)$$

where \mathcal{H} is the Hamiltonian containing all of the information of the chosen effective nucleon-nucleon interaction. The UNEDF (Universal Nuclear Energy Density Functional) framework makes use of a Skyrme energy that takes the form (e.g. Ref. [26])

$$E = E_{\text{kin}} + \int (\varepsilon_{\text{Sk}} + E_{\text{Coul}} + E_{\text{pair}}) d^3\vec{r} \quad (2.16)$$

where E_{kin} is the kinetic energy of the nucleons, E_{Coul} is the Coulomb energy and E_{pair} is the pairing energy. The time-even part of the Skyrme energy density, ε_{Sk} is [27]

$$\varepsilon_T^{\text{even}} = C_T^{\rho} \rho_T^2 + C_T^{\Delta\rho} \rho_T \Delta\rho_T + C_T^{\tau} \tau_T + C_T^J J_T^2 + C_T^{\nabla J} \rho_T \nabla \vec{J}_T, \quad (2.17)$$

while the time-odd part (which is not active in the functionals discussed in this chapter but described here for completeness) is

$$\begin{aligned} \varepsilon_T^{\text{odd}} = & C_T^{s} \vec{s}_T^2 + C_T^{\Delta s} \vec{s}_T \Delta \vec{s}_T + C_T^{sT} \vec{s}_T \vec{T}_T + \\ & + C_T^{\nabla s} (\nabla \vec{s}_T)^2 + C_T^j \vec{j}_T^2 + C_T^{\nabla j} \vec{s}_T \nabla \times \vec{J}_T, \end{aligned} \quad (2.18)$$

with \vec{s} , \vec{j} , \vec{J} and \vec{T} as the spin, current, spin current and spin kinetic densities respectively and $\varepsilon_{\text{Sk}} = \sum_{T=0,1} (\varepsilon_T^{\text{even}} + \varepsilon_T^{\text{odd}})$ (where T is the isospin). The parameters C_T^i are adjusted to various properties of finite nuclei chosen to give sensitivity to the parameter of study. The UNEDF0 functional was originally developed to provide a framework that could be used to universally predict nuclear masses, radii and deformations [26]. The UNEDF1 functional was later developed in order to optimise the parameters for large deformation [28] whilst the UNEDF2 functional built on this result by adding sensitivity to shell structure [24].

Another form of EDF is the Fayans functional [29]. These EDFs contain terms relating to the density gradient and Coulomb-nuclear interaction meaning that their dependence on the nuclear density is more complex than the previously mentioned Skyrme-like functionals [30]. In particular, the F(Δr , HFB) functional has recently been developed in the full Hartree-Fock-Bogolyubov formalism and has already been shown to accurately describe the charge radii of Ca [31]. EDF calculations using three functionals (UNEDF0 and UNEDF2 [24, 26] and Fayans) were performed for this work by M. Kortelainen and are discussed in more detail in Chapter 7.

Chapter 3

Hyperfine Interaction

In this work, the technique of laser spectroscopy is used to probe the properties of the atomic nucleus. This method makes use of the interaction between the total angular momentum of the nucleus and its surrounding electrons which becomes apparent when the atomic energy levels are measured at high resolution and is named the ‘hyperfine interaction’. The hyperfine interaction lifts degeneracies in these energy levels by causing a splitting due to the magnetic moment and the shape of the nucleus. Measurements of such quantities are vital probes of the underlying structure across the nuclear chart, shedding light on nucleon occupation of shells and the interactions between them. By comparing atomic spectra across an isotopic chain, one may also infer the difference in the nuclear mean-square charge radii between different nuclei. This allows for an observation of the rigidity (or otherwise) of the deformation and acts as a complementary measurement to the electric quadrupole moment even for nuclei of total angular momentum $I = 0, 1/2$ where the spectroscopic quadrupole moment is zero.

3.1 Hyperfine Splitting

Hyperfine Splitting due to the Magnetic Dipole Moment

The magnetic field produced by the orbiting electrons at the site of the nucleus couples to the nuclear magnetic dipole moment. This interaction leads to a perturbation of the electronic energy levels, given by

$$\Delta E_\mu = A \langle \vec{I} \cdot \vec{J} \rangle, \quad (3.1)$$

where A is the ‘hyperfine A coefficient’ which determines the magnitude of the dipole splitting and is defined by

$$A = \frac{\mu_I B_e(0)}{IJ}, \quad (3.2)$$

where μ_I is the magnetic moment of the nucleus as described in Section 2.2, $B_e(0)$ is the magnetic field created by the orbiting electrons at the point of the nucleus and I and J are the nuclear and atomic angular momenta or ‘spins’, respectively.

To evaluate Equation 3.1 the quantity \vec{F} , the vector addition of the nuclear and atomic total orbital angular momenta, is defined. This ‘hyperfine angular momentum’ is

$$\vec{F} = \vec{I} + \vec{J}. \quad (3.3)$$

The associated quantum number, F , may take on the values

$$F = |I - J|, |I - J| + 1, \dots, I + J - 1, I + J, \quad (3.4)$$

and the scalar product of \vec{I} and \vec{J} can be calculated as

$$\begin{aligned}\vec{F}^2 &= (\vec{I} + \vec{J})^2 = \vec{I}^2 + 2(\vec{I} \cdot \vec{J}) + \vec{J}^2 \\ \implies \vec{I} \cdot \vec{J} &= \frac{1}{2} [\vec{F}^2 - \vec{I}^2 - \vec{J}^2].\end{aligned}\tag{3.5}$$

The expectation value of $\vec{I} \cdot \vec{J}$ is

$$\langle \vec{I} \cdot \vec{J} \rangle = \frac{\hbar^2}{2} [F(F+1) - I(I+1) - J(J+1)].\tag{3.6}$$

For convenience, the quantum number ‘ K ’ is defined as

$$K = F(F+1) - I(I+1) - J(J+1),\tag{3.7}$$

to simplify the equation and hence we may describe the splitting according to the A coefficient in terms of the new quantum number

$$\Delta E_\mu = \frac{K}{2} A.\tag{3.8}$$

Hyperfine Splitting due to the Electric Quadrupole Moment

The quadrupole moment of a nucleus, as described in Section 2.3.1, also contributes to a change in energy splitting of atomic states through interaction with the electric field gradient created by the orbiting electrons. In this case, the change manifests itself in the form of a further shift in the hyperfine levels.

The shift in energy levels by the quadrupole moment of a nucleus is given by [2]

$$\Delta E_Q = \frac{3K(K+1) - 4I(I+1)J(J+1)}{8I(2I-1)J(2J-1)} B,\tag{3.9}$$

where B is known as the ‘hyperfine B parameter’ and is given by

$$B = eQ_s \left\langle \frac{\partial^2 V_e}{\partial z^2} \right\rangle. \quad (3.10)$$

Here, $\left\langle \frac{\partial^2 V_e}{\partial z^2} \right\rangle$ is the electric field gradient created by the atomic electrons.

3.1.1 Total Hyperfine Splitting

By combining the descriptions of the splitting according to the hyperfine A and B parameters from Equations 3.8 and 3.9, the total hyperfine splitting for a component with nuclear spin I and electronic angular momentum J is [2]

$$\Delta E_{hfs} = \frac{K}{2} A + \frac{3K(K+1) - 4I(I+1)J(J+1)}{8I(2I-1)J(2J-1)} B. \quad (3.11)$$

The effects of the splitting from the magnetic moment and the quadrupole moment can be seen in Figure 3.1.

3.2 Transitions Between Hyperfine States

In the measurements taken during this work, electrons are excited from a lower energy state with total angular momentum J_l a higher energy state with total angular momentum J_u and the decay from the state u is then detected by observing the emitted photon. Any peak in a hyperfine spectrum may be defined according to the energy difference between the two states from Equation 3.11. That is

$$\gamma = \nu + \alpha_u A_u + \beta_u B_u - \alpha_l A_l - \beta_l B_l, \quad (3.12)$$

where, for the sake of convenience,

$$\alpha = \frac{K}{2}, \quad (3.13)$$

$$\beta = \frac{3K(K+1) - 4I(I+1)J(J+1)}{8I(2I-1)J(2J-1)}. \quad (3.14)$$

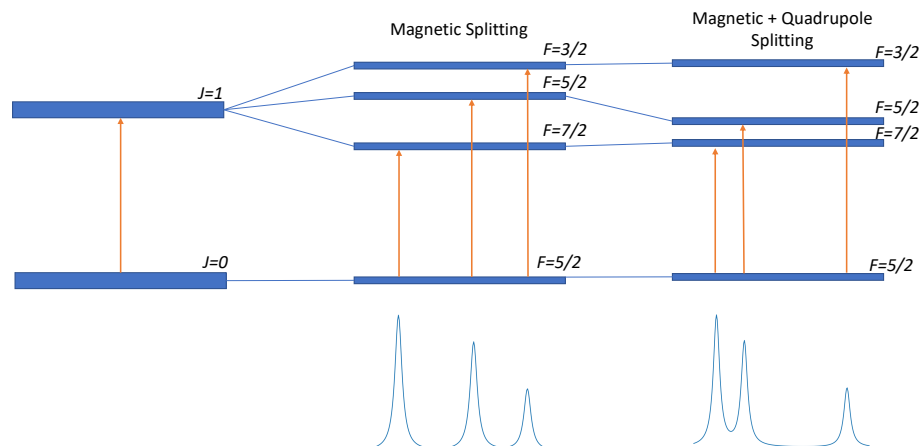


FIGURE 3.1: The splitting of atomic levels in ^{99}Y ($I = 5/2$) on a $J = 0 \rightarrow J = 1$ transition. Effects from magnetic and quadrupole interactions cause the splitting and shifting of energy levels.

The quantity ν refers to the centroid of the transition and is the point in frequency at which the splitting takes place.

3.2.1 Hyperfine Selection Rules

During a transition between two F states, the electrons must follow the hyperfine transitions rules. They are

$$\Delta F = 0, \pm 1, \quad (3.15)$$

$$F = 0 \nrightarrow F = 0. \quad (3.16)$$

In this way, the peaks of a hyperfine spectrum are formed. It is clear then that it is possible for the number of peaks in a hyperfine spectrum to give some information about the nuclear spin and in some cases the number of hyperfine peaks in a spectrum allows a spin identification without question. For example, when a $I = 1/2$ nuclear state is measured on a $J = 1/2 \rightarrow J = 1/2$ transition, there will be only three peaks in the hyperfine spectrum. However, when such

distinctions cannot be made, other methods must be used in order to extract the spin from the hyperfine spectra.

3.2.2 Extracting Nuclear Spin

Where the so-called ‘hyperfine anomaly’ (which occurs due to the non-pointlike nature of the nucleus) may be considered to be negligible, the ratios of A_l/A_u and B_l/B_u should remain constant across an isotopic chain. For the A parameter, this is the case since both the magnetic moment and the nuclear spin are properties of the nucleus, rather than the electronic state (and therefore take the same value for both A_u and A_l),

$$\frac{A_l}{A_u} = \frac{B_{e,l}(0)J_u}{B_{e,u}(0)J_l}. \quad (3.17)$$

It is also assumed that $B_{e,l}(0)/B_{e,u}(0)$ remains constant across the isotopic chain.

Likewise, for the B parameter, Q_s is a nuclear (rather than electronic) property and so the ratio

$$\frac{B_l}{B_u} = \frac{\left\langle \frac{\partial^2 V_{e,l}}{\partial z^2} \right\rangle}{\left\langle \frac{\partial^2 V_{e,u}}{\partial z^2} \right\rangle}, \quad (3.18)$$

also remains constant.

Extraction of these ratios is possible through fitting the hyperfine spectrum and can be performed for multiple nuclear spins. In cases where the ratios differ by a higher magnitude than is explicable by a hyperfine anomaly, the assumed spin can usually be falsified.

The relative spacing of hyperfine peaks is intrinsically related to the nuclear spin. In order to confirm a spin through laser spectroscopy, it is necessary for all of the measured peaks (this needn’t be a peak for every allowed transition but

should be enough that the system is well defined) from one isotope to be fitted by the routine simultaneously. In some cases, certain nuclear spins will not allow for the correct peak spacing in the spectrum, regardless of the values used for A and B . When this happens, these spins too can be discounted.

A less reliable way of extracting the nuclear spin is to observe the relative intensities of the peaks. Peaks corresponding to different hyperfine transitions will share differing amounts of the total resonant counts according to the angular momenta of the states involved. If it can be considered that hyperfine states have not been ‘pumped’ out of by multiple excitations (which may not return to their original state under de-excitation) then these peak intensities can aid in the assignment of the nuclear spin [32].

3.2.3 Extracting Nuclear Moments

Where $I, J \geq 1/2$, it is possible to extract the magnetic dipole moment from the hyperfine spectrum by means of the hyperfine A parameter. Furthermore, if $I, J > 1/2$ we may also extract Q_s . In cases where the magnetic and/or quadrupole moments are already known for a (usually stable) reference isotope, ratios of hyperfine parameters may be used in order to simplify the extraction of the moments of interest. This is possible since

$$\mu = \mu_{\text{ref}} \frac{IA}{I_{\text{ref}}A_{\text{ref}}}, \quad (3.19)$$

$$Q_s = Q_{s,\text{ref}} \frac{B}{B_{\text{ref}}}. \quad (3.20)$$

Knowledge of the magnetic and quadrupole moments for many isotopes are documented in readily available databases and tables (see, for example, Ref. [33]).

Once the nuclear moments are known, nuclear parameters of interest may be extracted. From the magnetic moment, the nuclear g-factor is extracted easily as

$$g = \frac{\mu}{I}, \quad (3.21)$$

and from the quadrupole moment, it is also possible to extract the β_2 deformation parameter. For the spectroscopic quadrupole moment, one must first calculate the ‘intrinsic quadrupole moment’ in order to extract the expectation value of quadrupole deformation parameter $\langle\beta_2\rangle$. This process is discussed in further detail in Section 7.7.

3.3 Isotope Shift

The change in mass, size and shape of the atomic nucleus has a profound effect on the measurement of the hyperfine structure. One finds that the addition or subtraction of neutrons to a nucleus causes a change in the centroid of an atomic resonance. This shift in centroid position is known as the isotope shift. It can be written as [15]

$$\delta\nu^{A,A'} = \delta\nu^{A'} - \delta\nu^A, \quad (3.22)$$

where ν^A and $\nu^{A'}$ are the centroid positions of isotopes with masses A and A' respectively. It is the result of two contributing phenomena from changes in the electric field observed by the atomic electrons and in the mass of the atomic nucleus itself. In such a way, the difference in centroid position may be expressed as

$$\delta\nu^{A,A'} = \delta\nu_{\text{MS}}^{A,A'} + \delta\nu_{\text{FS}}^{A,A'}, \quad (3.23)$$

where $\delta\nu_{\text{MS}}$ is known as the ‘mass shift’ and $\delta\nu_{\text{FS}}$ is known as the ‘field shift’.

3.3.1 The Mass Shift

The mass shift contribution to the isotope shift arises from the finite mass of the nucleus. As nucleons are added to, or removed from, the nucleus, this finite nuclear mass will change and hence alter the recoil motion of the nucleus. This causes an alteration of the kinetic energy of the system and hence a perturbation in the electronic structure [34].

The kinetic energy of the atom with A nucleons can be written as a summation of the energies of the nucleus and electrons [35]

$$T_A = \frac{\vec{P}_A^2}{2Am_u} + \sum_i \frac{\vec{P}_i^2}{2m_e}, \quad (3.24)$$

where m_u and m_e are the mass of a nucleon and an electron respectively and \vec{P}_A and \vec{P}_i are the momenta of the nucleus and of each electron. Since the atom is assumed to be stationary,

$$\vec{P}_A = - \sum_i \vec{P}_i, \quad (3.25)$$

and hence Equation 3.24 may be rewritten as

$$T_A = \sum_i \frac{\vec{P}_i^2}{2m_e} + \frac{1}{Am_u} \left(\sum_i \frac{\vec{P}_i^2}{2} + \sum_{i<j} \vec{P}_i \cdot \vec{P}_j \right). \quad (3.26)$$

Likewise, the kinetic energy of an atom with A' nucleons may be written as

$$T_{A'} = \sum_i \frac{\vec{P}_i^2}{2m_e} + \frac{1}{A'm_u} \left(\sum_i \frac{\vec{P}_i^2}{2} + \sum_{i<j} \vec{P}_i \cdot \vec{P}_j \right). \quad (3.27)$$

The difference in kinetic energy of the two atoms is then

$$\begin{aligned}\delta T^{A',A} &= T_A - T_{A'} \\ &= \frac{1}{m_u} \frac{A' - A}{A'A} \left(\sum_i \frac{\vec{P}_i^2}{2} + \sum_{i < j} \vec{P}_i \cdot \vec{P}_j \right).\end{aligned}\quad (3.28)$$

The term in Equation 3.28 containing \vec{P}^2 gives rise to the ‘normal mass shift’ while the term containing $\vec{P}_i \cdot \vec{P}_j$ is the origin of the ‘specific mass shift’. The change in the transition frequencies may then be written as [34]

$$\delta \nu_{\text{MS}}^{A,A'} = \delta \nu_{\text{NMS}}^{A,A'} + \delta \nu_{\text{SMS}}^{A,A'} = N \frac{A' - A}{A'A} + S \frac{A' - A}{A'A}.\quad (3.29)$$

The quantity N is simple to calculate and is defined as

$$N = \nu_0 \frac{m_e}{m_u},\quad (3.30)$$

where ν_0 is the transition frequency of an infinitely massive nucleus.

The specific mass shift term may be considered a correction to the normal mass shift for the case where more than one electron is present inside the atom (i.e. any element other than hydrogen). In this case, it is obvious that electrons can be distributed asymmetrically around the atomic nucleus (see Figure 3.2) and this distribution will cause a shift in the centre of mass of the system. For example, if electrons orbit on the same side of the atomic nucleus then the centre of mass of the system will be shifted towards the orbiting electrons. Where the electrons orbit on opposite sides of the nucleus, these contributions will somewhat cancel and cause the centre of mass of the system to exist closer to the centre of the nucleus.

It is clear then that the computation of the value S is far from trivial especially for the many-electron atom. However, empirical estimates for the specific mass

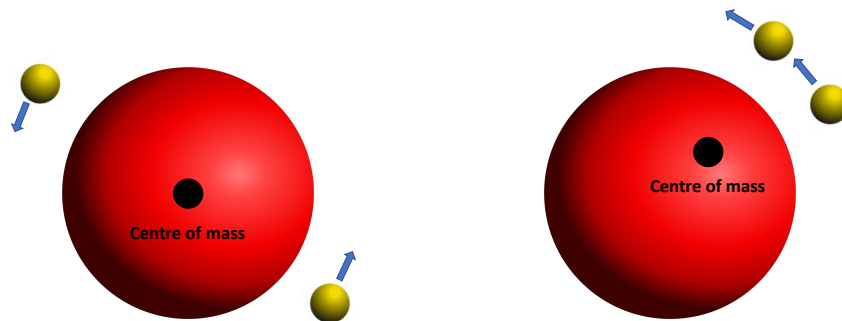


FIGURE 3.2: A many-electron atom can experience a distribution of orbiting charge. Electrons may have momenta in the opposite (left) or the same (right) direction.

shift exist in terms of the magnitude of the normal mass shift for that element. They are [36]

$$\delta\nu_{\text{SMS}}^{A,A'} = (0.3 \pm 0.9)\delta\nu_{\text{NMS}}^{A,A'} \text{ for } ns - np \text{ transitions,} \quad (3.31)$$

$$\delta\nu_{\text{SMS}}^{A,A'} = (0.0 \pm 0.5)\delta\nu_{\text{NMS}}^{A,A'} \text{ for } ns^2 - nsnp \text{ transitions.} \quad (3.32)$$

3.3.2 The Field Shift

An electron orbiting a nucleus will experience an electrostatic potential, arising from the electric charge distributed across the volume of the atomic nucleus (see Figure 3.3). The nucleus is not a point-like object and so as neutrons are added to this nucleus, the volume (and therefore the charge distribution across it) changes, leading to a change in energy of the atomic electrons and therefore an alteration of the energy of the atomic transitions. Due to this, laser spectroscopy provides a method by which the size of a nucleus, relative to the size of another isotope in its chain, may be measured. Through measurement of the isotope shift, combined

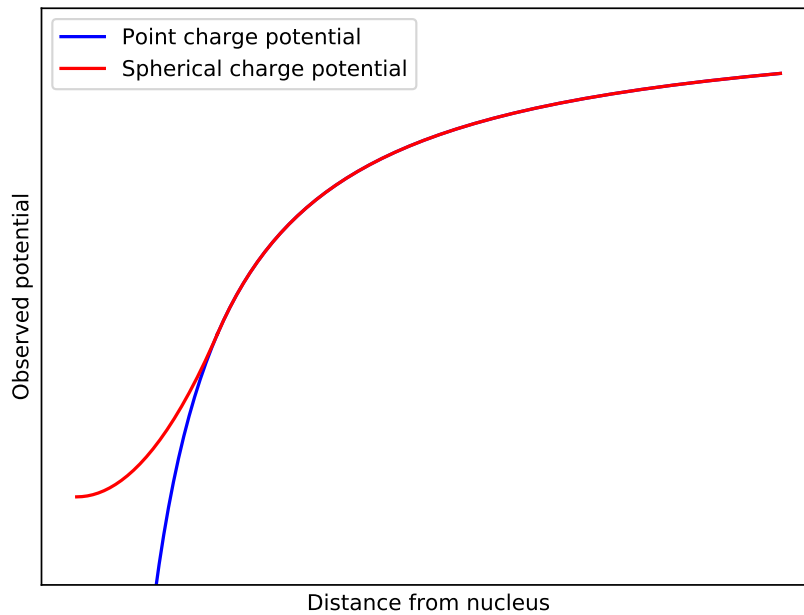


FIGURE 3.3: The electric potential a nucleus would experience from a Coulomb potential (red) and in the case of a spherical charge (blue).

with the knowledge of the mass shift, the technique is sensitive to the mean-square charge radius of a nucleus.

The electrostatic potential experienced by the electrons when orbiting a nucleus of mean-square charge radius $\langle r^2 \rangle$ is

$$E = \frac{Ze^2}{6\epsilon_0} |\psi_e(0)|^2 \langle r^2 \rangle, \quad (3.33)$$

where $|\psi_e(0)|^2$ is the electronic charge density generated by the atomic electrons at the position of the nucleus [15].

The difference in energy between the same transition in two isomers (the field shift component of the isotope shift) may hence be written as

$$\delta\nu_{\text{FS}}^{A,A'} = \frac{Ze^2}{6h\epsilon_0} \Delta |\psi_e(0)|^2 \delta \langle r^2 \rangle^{A,A'}. \quad (3.34)$$

For simplicity, $\frac{Ze^2}{6h\epsilon_0} \Delta |\psi_e(0)|^2$ is defined as F and is referred to as the ‘field factor’ where $\Delta |\psi_e(0)|^2$ is the change in charge density between two states, evaluated at the origin.

3.3.3 Total Isotope Shift

By combining the two contributions to the shift in frequency of a given atomic transition, a complete picture of the isotope shift is constructed. That is

$$\delta\nu^{A,A'} = \delta\nu_{\text{MS}}^{A,A'} + \delta\nu_{\text{FS}}^{A,A'} = M \frac{A' - A}{A'A} + F \delta \langle r^2 \rangle^{A,A'}, \quad (3.35)$$

and enables the technique of laser spectroscopy to probe not only magnetic and quadrupole moments of the nucleus of interest but also the evolution of nuclear size and shape across an isotopic (or even isomeric, where $\frac{A'-A}{A'A} \approx 0$) chain.

For cases where isotope shifts have been measured, the ‘King plot’ technique may be used where the charge radius of three or more isotopes in the chain are known as well as the electronic factors for another transition.

3.4 King Plot Technique

The linearity of the form of the isotope shift may be exploited through the King plot [34]. By applying a linear fit to the measured isotope shifts of two atomic transitions, the F and M factors can be extracted when the factors for one of the transitions are known. This becomes particularly useful when no good theoretical estimates exist and measurements must rely on solely quantitative techniques.

By introducing a modification factor $\zeta = \frac{A'A}{A'-A}$ to Equation 3.35 (for a transition i), the expression may be written as

$$\zeta \delta \nu_i^{A,A'} = M_i + \zeta F_i \delta \langle r^2 \rangle^{A,A'}. \quad (3.36)$$

Likewise, the isotope shift for a transition j is

$$\zeta \delta \nu_j^{A,A'} = M_j + \zeta F_j \delta \langle r^2 \rangle^{A,A'}. \quad (3.37)$$

Since $\delta \langle r^2 \rangle^{A,A'}$ must be the same in both Equations 3.36 and 3.37 (as it is a property of the nucleus, rather than the transition), the expressions are equated to yield

$$\frac{1}{F_j} \left[\zeta \delta \nu_j^{A,A'} - M_j \right] = \frac{1}{F_i} \left[\zeta \delta \nu_i^{A,A'} - M_i \right], \quad (3.38)$$

which, in turn, leads to the useful relation

$$\zeta \delta \nu_j^{A,A'} = \frac{F_j}{F_i} \zeta \delta \nu_i^{A,A'} + M_j - \frac{F_j}{F_i} M_i. \quad (3.39)$$

A ‘King plot’ of the modified isotope shifts yields a straight line with gradient $\frac{F_j}{F_i}$ and an intercept of $M_j - \frac{F_j}{F_i} M_i$. Therefore, the factors for one transition (which may be chosen for efficiency) can be related to those of another transition if the factors of one are known.

Should the mean-square charge radii be known from non-optical techniques then the King plot technique may still be utilised by considering a hypothetical transition with electronic factors of $F_i = 1$ and $M_i = 0$. In this case, the gradient of the plot directly gives the field factor of the transition of interest and the intercept, the mass factor.

In cases where no information is yet known about the chain, empirical techniques can be used to generate F and M factors whereby the factors are used alongside measured isotope shifts and varied to match the systematic trends of the region.

Chapter 4

Laser Spectroscopy

The method of laser spectroscopy is a powerful tool for measuring the shape and size of atomic nuclei as well as the magnetic g-factors of the occupying nucleons and is adopted by many facilities around the world covering a range of techniques. The resolution of the measurements is strongly related to the type of measurement taking place. For example, in-source measurements (where measurements are performed on atoms as they are released from the target material) tend to have a large amount of Doppler broadening due to the large range of velocities of the sample [37]. Techniques such as fast-beam laser spectroscopy have provided large enhancements on this resolution, though usually at the cost of a loss in sensitivity of the measurement of short-lived states. There is, of course, a hard limit on the resolution of a laser spectroscopic measurement since the non-zero lifetime of the excited atomic state causes a natural line width of the hyperfine resonances. Typically, these line widths are of the order of tens of MHz - a small number compared to the transition frequencies which are typically in the order of THz.

4.1 Line Shapes

4.1.1 Homogeneous Line Broadening

The existence of a finite lifetime of a given atomic state leads to a natural line width of a profile in a laser spectroscopic measurement. This can be shown by first describing the system as a damped oscillator

$$e(t) = \frac{E_0}{2} \left[\exp \left(i \left(\omega_0 + \frac{i\sigma}{2} \right) t \right) + \exp \left(-i \left(\omega_0 - \frac{i\sigma}{2} \right) t \right) \right], \quad (4.1)$$

where $\frac{\sigma}{2}$ is the field decay rate. A Fourier transform of $e(t)$ ($E(\omega) = \int_0^\infty e(t)e^{i\omega t} dt$) gives

$$E(\omega) = \frac{E_0}{2} \left(\frac{i}{\omega_0 - \omega + \frac{\sigma}{2}i} - \frac{i}{\omega_0 + \omega - \frac{\sigma}{2}i} \right), \quad (4.2)$$

where ω is the angular frequency. This in turn leads to the general line shape description of

$$|E(\omega)|^2 \propto \frac{1}{\omega - \omega_0 + \left(\frac{\sigma}{2}\right)}, \quad (4.3)$$

when $\omega \approx \omega_0$. Defining $\Delta\nu_H = \sigma/2\pi$ and normalising, Equation 4.3 becomes

$$g(\nu)_H = \frac{\Delta\nu_H}{2\pi \left((\nu - \nu_0)^2 + \left(\frac{\Delta\nu_H}{2}\right)^2 \right)}. \quad (4.4)$$

where ν is the frequency and $g(\nu)_H$ is the line shape. This is a Lorentzian line shape and the effect is known as homogeneous broadening as it applies to all atoms in the same way [38].

4.1.2 Inhomogeneous Line Broadening

Departures from the natural Lorentzian line shape are possible where experimental conditions cause a ‘broadening’ of the line width. Mostly, these contributions are Gaussian in nature and so the overall line shape of the hyperfine resonance is, in these cases, observed as a Voigt profile - a convolution of the Gaussian and Lorentzian line shapes. Such a line shape is defined by

$$V(x, \gamma, \sigma) = \int_{-\infty}^{\infty} G(x', \gamma) L(x - x', \sigma) dx', \quad (4.5)$$

where $G(x', \gamma)$ is the Gaussian component with FWHM of γ and $L(x - x', \sigma)$ is the Lorentzian component with FWHM of σ [35].

Doppler Broadening

A common cause of line broadening within the technique of laser spectroscopy is Doppler broadening. This occurs since the excited atoms/ions naturally exhibit a range of velocities according to a Maxwell-Boltzmann distribution which can be described by

$$f(v_x, v_y, v_z) = \left(\frac{M}{2\pi kT} \right)^{\frac{3}{2}} \exp \left(-\frac{M}{2kT} (v_x^2 + v_y^2 + v_z^2) \right), \quad (4.6)$$

where M is the atomic mass, k is the Boltzmann constant, T is the temperature of the atom and v_x, v_y and v_z are the velocities in x, y and z respectively. Since these velocities are independent of each other and the only dimension of interest is that in the direction of the laser beam axis, we may express the probability of the transition frequency (between ν and $\nu + d\nu$), $g(\nu)d\nu$, as

$$g(\nu)d\nu = \left(\frac{M}{2\pi kT} \right)^{\frac{3}{2}} \int_{-\infty}^{\infty} \int_{-\infty}^{\infty} \exp \left(-\frac{M}{2kT} (v_y^2 + v_z^2) \right) dv_y dv_z \times \left(\frac{c}{\nu_0} \right) \exp \left(-\frac{Mc^2}{2kT\nu_0^2} (\nu - \nu_0)^2 \right) d\nu. \quad (4.7)$$

Here, the velocity in the direction of the laser axis, v_x , has been expressed in terms of the rest frame frequency, ν_0 , and the frequency observed in the frame of the atom, ν .

Since

$$\int_{-\infty}^{\infty} \exp\left(-\frac{M}{2kT}v_z^2\right) dv_z = \left(\frac{2\pi kT}{M}\right)^{\frac{1}{2}}, \quad (4.8)$$

Equation 4.7 may be written as

$$g(\nu) = \frac{c}{\nu_0} \left(\frac{M}{2\pi kT}\right)^{\frac{1}{2}} \exp\left(-\frac{Mc^2}{2kT\nu_0^2}(\nu - \nu_0)^2\right). \quad (4.9)$$

Equation 4.9 describes a Gaussian line shape and hence any broadening that takes place from the range of velocities within a sample will take on Gaussian properties [38]. Fast-beam laser spectroscopy has been developed to decrease the effect of Doppler broadening below that of the natural line width of the peak. This is discussed in more detail in Subsection 4.2.1.

Power Broadening

In the case of an ion beam being continuously excited with continuous-wave laser radiation, the population of the excited state in the ion beam is dependent on the process of excitation and on the spontaneous and stimulated emission from those states. In the equilibrium state, the population $\langle P_2 \rangle$ of the excited state (which is proportional to the measured signal) is given by [39]

$$\langle P_2 \rangle = \frac{1}{2} \frac{(I/I_{sat})}{1 + (\Delta/\beta)^2 + (I/I_{sat})}, \quad (4.10)$$

where $\Delta = \omega_0 - \nu$, the difference between the atomic Bohr frequency ω_0 and the laser frequency β is the width parameter in the weak-excitation limit, ν , I_{sat} is the saturation intensity and I is the intensity of the incoming beam. An increase in

the intensity of the laser will then cause an increase in the width of the profile. This broadening has a Lorentzian dependence on Δ .

Pressure Broadening

Pressure broadening (sometimes referred to as collisional broadening) takes place when the ions (or atoms) of study are in a gas of sufficiently high pressure. Collisions with neighbouring molecules cause a termination of the excited state of the ion. The decreased lifetime of the state leads to an increase in the uncertainty in the energy of the transition and hence a wider line shape due to the uncertainty principle $\Delta E \Delta t \approx \frac{\hbar}{2}$ [40].

4.2 An Overview of the Technique of Laser Spectroscopy

4.2.1 Fast-Beam Collinear Laser Spectroscopy

In order to probe the hyperfine structure of the ion in this work, the technique of collinear laser spectroscopy is employed. In this technique, radioactive ions must first be formed in to a beam and accelerated towards the laser beam. Through applying a secondary (much smaller) tuning voltage, fast ion beams are brought in to resonance with narrowband laser light, which is locked to a certain wavelength, by the Doppler effect. A basic diagram of the anti-collinear geometry can be found in Figure 4.1. This technique allows for very high precision since high velocities of ion beams allow for the reduction of the aforementioned Doppler broadening to below the natural line width and the laser does not have to change frequency throughout the experiment.

An accelerated ion beam observes a shift in the frequency of the laser light as governed by the laws of Doppler. The frequency of the laser light observed by the

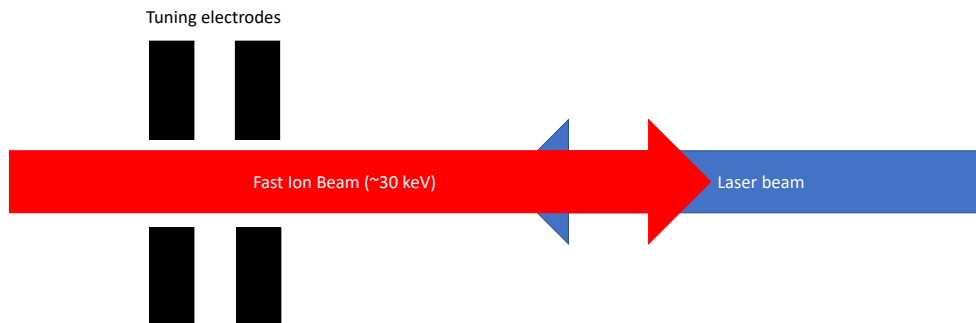


FIGURE 4.1: The basic geometry of the laser-ion interaction in anti-collinear laser spectroscopy. Ions are accelerated to high velocities and meet the laser beam head on.

ion beam ν_{obv} can be calculated from the wavelength of the laser ν_{las} in the rest frame by [2]

$$\nu_{\text{obv}} = \nu_{\text{las}} \left(1 + \alpha \pm \sqrt{2\alpha + \alpha^2} \right). \quad (4.11)$$

In this description, the quantity α is defined as

$$\alpha = \frac{qV}{M_A c^2}, \quad (4.12)$$

where q is the charge of the ion in the beam, V is the acceleration voltage experienced by the ion and M_A is the mass of the atom in question. The \pm refers to anti-collinear (where the sign is positive) and collinear setups (where the sign is negative). For an example of a collinear set-up, see Ref. [21].

By changing the acceleration voltage, the experimental set up has the ability to scan over a range of observed frequencies without the need to change the frequency of the laser and therefore removing any associated systematic uncertainties. By stepping the acceleration voltage and measuring the number of resonant counts

detected by the photomultiplier tubes, a full hyperfine spectrum may be built up.

Another benefit of fast-beam collinear laser spectroscopy is its further allowance for high-resolution spectroscopy by means of manipulating the Doppler broadening phenomenon. An ion beam has energy

$$E = \frac{1}{2}M_A v^2, \quad (4.13)$$

which gives a spread of velocities (and therefore observed frequencies) described by

$$\Delta E = M_A v \Delta v. \quad (4.14)$$

Such energy spreads appear due to differing energies of the ions emerging from the ion source during production, a process through which experimenters have only limited control.

Since the spread in energy of an ion beam must remain constant under electrostatic acceleration, as all ions experience the same acceleration voltage, an increase in velocity of the ion beam must decrease the spread of velocities (see Figure 4.2) Typical acceleration voltages at the collinear laser spectroscopy setup at JYFL are around 30 kV, which is enough to bring the effect of the energy spread to below the natural line width of a transition.

4.2.2 Fitting Process

In this work, the hyperfine spectra are fitted using a Python routine implementing the SciPy *least_squares* package [41]. Within this routine, a model hyperfine spectrum with Lorentzian peaks is generated by the user using initial estimates for the starting parameters. Voigt profiles were considered for the fitting routine but

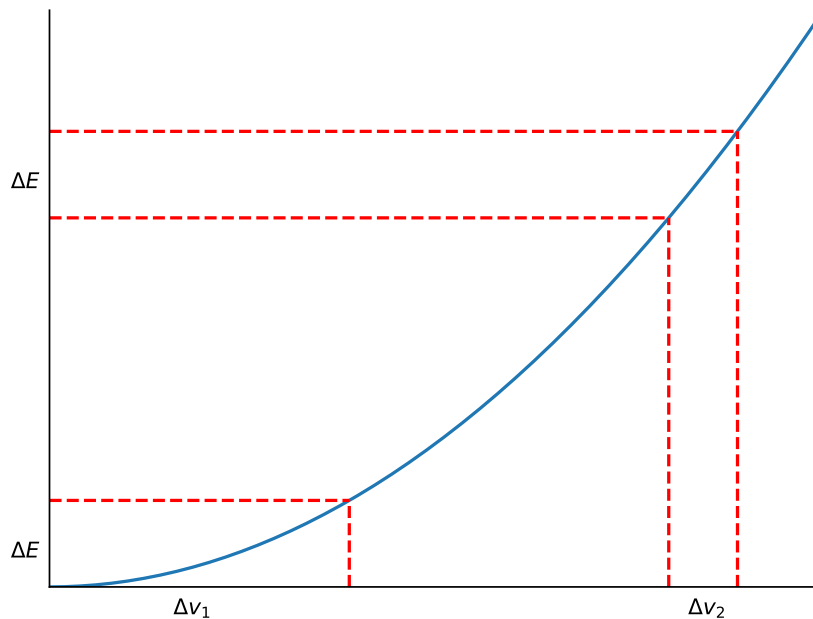


FIGURE 4.2: The effect of increasing the velocity on the velocity spread under electrostatic acceleration.

were ultimately not used in favour of the simpler Lorentzian line shape since the latter was found to describe the experimentally measured line shape well. These starting estimates include background, FWHM of the hyperfine peaks (which is shared across all peaks), an intensity for each peak (which allows the intensity of each peak to vary freely) and values for the hyperfine A and B parameters and the centroid of the structure. If necessary, extra constraints can be placed on these values within the routine. For example, it is possible to hold the ratio of hyperfine constants within the routine.

This model can also be extended to fit multiple files at the same time. In this technique, spectra are fitted with shared parameters which describe the hyperfine A and B parameters but the centroid of each spectrum is allowed to vary in order to account for experimental drifts which may occur between separate runs. Each spectrum is also allowed its own background count and, as before, peak intensities

are allowed to vary freely.

The χ^2 minimisation is provided by the *least_squares* package, which works to minimise a cost function based off many iterations from the user-provided starting estimates. In order to prevent the possibility of the routine ending in a false minimum, it is important to provide starting estimates close to the true values. Once the minimum has been found, *least_squares* returns the fitted values for each parameter along with a Jacobian matrix, evaluated at the solution. The covariance matrix is then calculated by

$$C = J^T \cdot J, \quad (4.15)$$

where C is the covariance matrix and J is the returned Jacobian matrix. The errors are then taken as the diagonal elements of C and scaled by the square root of the χ_r^2 of the fit. This value is determined by first finding the χ^2 value

$$\chi^2 = \sum_{i=0}^n \frac{(x_i - x'_i)^2}{\sigma_i^2}, \quad (4.16)$$

where n is the number of data points, x_i is the fitted number of counts to the i th data point, x'_i , and σ_i is the associated error defined by $\sigma_i = \sqrt{x'_i + 1}$. The reduced χ^2 is therefore this value divided by the number of degrees of freedom in the fit, ν , i.e. the number of data points minus the number of fitting parameters. That is

$$\chi_r^2 = \frac{\chi^2}{\nu}. \quad (4.17)$$

The statistical errors extracted from the fit in this way may then be used alongside the errors from the reference values of previously measured isotopes in order to extract the error on the measured electromagnetic moments.

The *least_squares* package used in this routine also allows for bounds to be placed on the parameters such that they will not be allowed to minimise outside a selected range. For example, a peak intensity cannot be less than zero and so it is unphysical to have a peak intensity fit to negative counts. To avoid this, it is possible to set a lower bound of zero to the appropriate parameters.

4.2.3 Other Forms of Laser Spectroscopy

As well as the technique of collinear laser fluorescence spectroscopy (as used in this work), many other laser spectroscopic techniques are used at nuclear structure facilities across the globe. The most similar technique to that described previously is Collinear Resonance Ionisation Spectroscopy (CRIS). This approach uses many of the same methods as standard collinear laser spectroscopy with the biggest difference being that instead of allowing electrons to de-excite after interaction with the spectroscopic laser beam and counting the resultant photons, one or more lasers are used to excite the electron past its ionisation potential. The newly created ion is then guided towards an ion counter or decay detection station by electric fields and counted towards a hyperfine spectrum for each set laser frequency [42]. Due to the nature of this setup, spectroscopy must be performed on the atom only but the technique has the advantage of very low background signal since it is not subject to the same laser scatter as fluorescence spectroscopy. One such example of this technique is the RAPTOR beam line, which is currently in commission at the IGISOL facility.

Another noteworthy technique is the method developed by the RADRIS collaboration for the study of the heaviest elements [43]. The RAdiation Detected Resonance Ionisation Spectroscopy (RADRES) setup is located at the GSI facility, Darmstadt, Germany and is designed to perform laser spectroscopy on the heaviest

elements which can only be produced at the rate of a few ions per second and as such requires zero background techniques for their study. The element of interest is produced in an ionised state by fusion evaporation reactions and selected by the SHIP velocity filter before being guided in to a gas cell where the ion is attracted to an electrically charged filament. After a pre-determined collection time, the beam is shut off and the filament heated to a high temperature, releasing the reaction products and producing a cloud of neutral atoms. This cloud is then hit by several laser beams in order to perform the spectroscopic and ionisation steps of the chosen scheme. Successfully ionised atoms (which are only of the element of study due to the sensitivity of the ionisation) are then guided to a PIPS detector where a number of α -decay events are counted. The spectroscopic laser frequency is then changed and the process repeated, building a spectrum of laser frequency and α particle counts. This technique has so far been successfully utilised to study several isotopes of nobelium and, more recently, a campaign is underway to further the technique to the study of lawrencium.

Chapter 5

The IGISOL Facility

5.1 IGISOL-IV

IGISOL-IV is an experimental setup located at the University of Jyväskylä in central Finland. Although housed in its own hall, IGISOL-IV is a section of the wider JYFL Accelerator Laboratory. Other major setups include MARA (Mass Analysing Recoil Apparatus) and RITU (Recoil Ion Transfer Unit). Unlike these other setups, IGISOL allows for the creation of monoenergetic (around 30 keV) radioactive ions, a feature paramount to high-resolution laser spectroscopy as well as other techniques such as high-precision mass measurements. A diagram of the IGISOL-IV facility is shown in Figure 5.1.

5.2 The IGISOL Method

To create the necessary radioactive nuclei for measurement, 30 MeV protons from a K-130 cyclotron are fired at a thin-foil target material. The use of a thin-foil target, as opposed to a thick target, gives IGISOL its advantage over other facilities. Reaction products recoil directly from the target meaning surface or laser ionisation from the target is unnecessary. Further to this, the immediate removal of ions from the target opens up the possibility of measuring isotopes with shorter

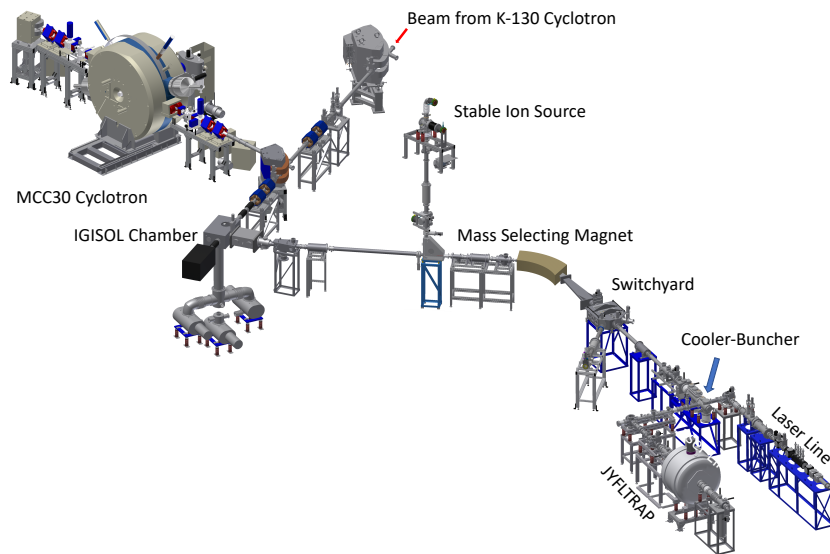


FIGURE 5.1: A diagram of the IGISOL-IV facility [44].

half lives inaccessible to facilities that use thick targets since they tend to have longer extraction times for the products of interest. This is particularly true of the refractory elements (such as Y and Nb) where removal from a thick target would not be possible. The fast removal of products from the target area provides considerably smaller losses through decay.

Since reaction products leave the target at high speed, they must be caught by a helium buffer gas, where the ions are thermalised. This He gas (of typical pressures around 250 mbar within the gas volume) is ejected through a 1 mm exit nozzle as a supersonic gas jet, moving the reaction products towards the sextupole ion guide (see below) before itself being pumped away by Roots pumps. A schematic of the IGISOL front end is shown in Figure 5.2.

5.2.1 The SPIG

The SPIG (Sextupole Ion Guide) is made of six metal rods, arranged in a circle [45]. In order to form an ion beam from the IGISOL reaction products, these rods are supplied with a potential which oscillates between polarities. To ensure symmetry, each rod is in antiphase with adjacent rods. The resulting electric

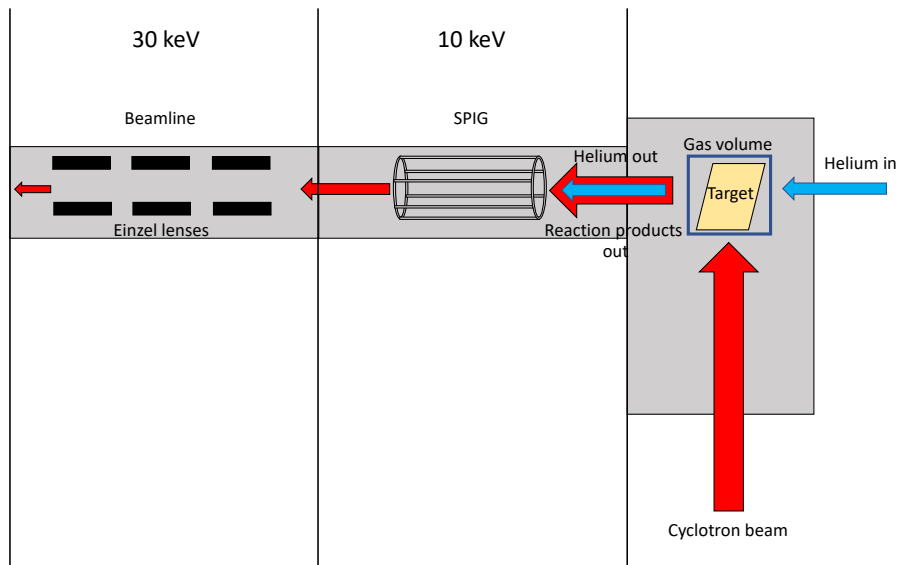


FIGURE 5.2: A schematic of the IGISOL front end.

field focuses the ions in to the centre of the SPIG (which itself operates by the application of an RF frequency of around 3-4 MHz and an RF amplitude of 0-600 V_{pp} [45]) and hence a beam is created and then accelerated to 30 keV (due to the +30 kV potential of the IGISOL chamber) towards the experimental area whilst being focused with Einzel lenses.

5.2.2 Mass Separation

Just before entering the experimental area, the ion beam passes through a 55° dipole magnet for selection by atomic mass. The magnetic force experienced by the ions as they pass through the magnet is described by

$$F = qvB = \frac{mv^2}{r} \implies r = \frac{mv}{qB}, \quad (5.1)$$

where B is the strength of the magnetic field created by the magnet, v is the velocity of the beam, and q and m are the charge and the mass of the ion, respectively.

The energy of the ions is supplied through the acceleration voltage, V , so

$$E_k = \frac{1}{2}mv^2 = qV \implies v = \sqrt{\frac{2qV}{m}}. \quad (5.2)$$

By utilising Equations 5.1 and 5.2, it can be shown that

$$B = \sqrt{\frac{2Vm}{r^2q}}, \quad (5.3)$$

hence by varying the magnetic field strength of the dipole magnet, a ratio of $\frac{m}{q}$ for a given r can be selected. It is normally assumed that a majority of the ions leave the IGISOL front end in a singly charged state, however since selection occurs via $\frac{m}{q}$ it is also possible to select a charge state as well as a mass. One notable example is the work which has taken place on doubly charged yttrium [44].

5.3 Stable Ion Source

Access to an ‘offline source’ for the production of stable isotopes is available at the IGISOL facility for the purposes of beam tuning and stable reference measurements during an online experiment. The beam enters the main experimental area through a 90° bender from the vertical shortly before the mass-selecting magnet. There are two offline sources present at the IGISOL facility, a surface ion source and a spark source [46].

The surface ion source creates an ion beam by means of heating the source material to such a point that its energy exceeds that of the work function of the surface. Once this threshold has been surmounted, the ions are desorbed and lose an electron to the surface, forming a cloud of ions [47].

The principle of the spark ion source is to induce high-voltage discharge sparks which ionise the helium buffer gas surrounding a cathode. The ionised particles

are then attracted to the cathode at high velocity and cause fragmentation of the source material. The spark source can therefore provide an offline source of many metallic elements by simply changing the cathode to the material of choice.

In either case, ions are formed in to an ion beam by a skimmer electrode after production, before being focused by an Einzel lens and injected in to the main beam pipe before the magnet by an extractor electrode, accelerating the ions to 30 kV [46].

5.4 The Ion Cooler-Buncher

The use of ion coolers for the purposes of laser spectroscopy was pioneered by the IGISOL group in the early 2000s [48]. By decreasing the spread of kinetic energies within the beam the Doppler broadening effect is reduced, further improving the resolution to to the natural line width. Moreover, the addition of a buncher to the end of the cooling unit can allow for time gating on the arrival of an ion beam. This time gating allows for a background reduction by a factor of ten thousand.

The Cooler

When leaving the ion guide, ions have a range of energies due to random collisions with helium during the acceleration process. This spread in energy leads to a spread of velocities of the ions as described by a Maxwell-Boltzmann distribution, explained in more detail in Section 4.1.

By cooling the ions to the point where they are thermalised, the energy of the ions is, in a sense, ‘reset’ and will therefore have a much lower spread of energy than those leaving the IGISOL since they all leave the cooler in a similar energy state.

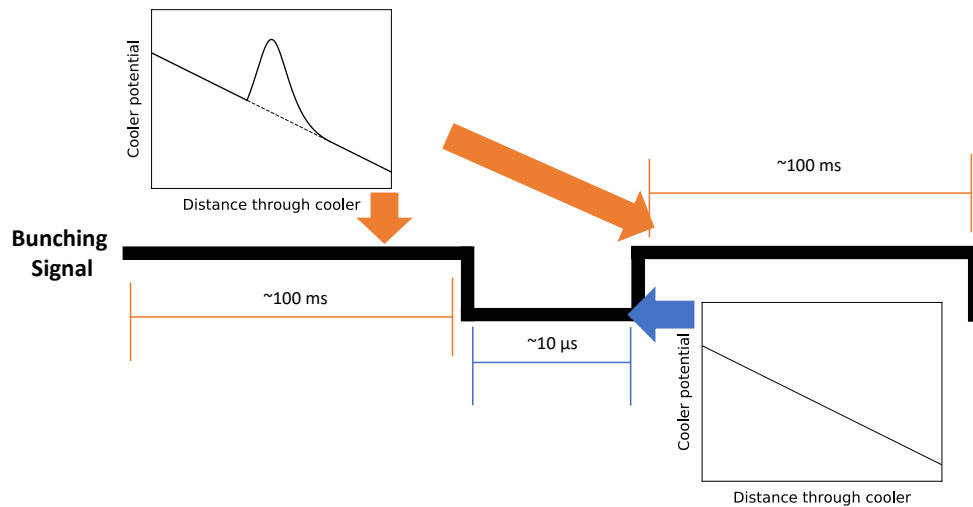


FIGURE 5.3: The potential throughout the cooler when the gate is raised and lowered according to the bunching signal being on or off.

Cooling is made possible through a deceleration of the ions (by the 30 kV platform of the cooler) followed by repeated collisions with helium atoms within the cooler whilst the ions are confined radially by the use of a segmented radio frequency quadrupole. A potential gradient down the cooler is also applied to guide the ions towards the end of the line. With each collision, the ion beam loses kinetic energy until the point that the ions become thermalised. Typical He pressures within the cooler are ≈ 0.1 mbar.

The Buncher

By applying a potential gate to the end of the cooler, the ions become trapped within the volume of the device. This gate can be raised and lowered as required through the DAQ (Data Acquisition) controls. Typical cycles of this bunching last for around 100 ms with the gate raised, followed by 10 μs of the gate lowered (see Figure 5.3, which shows the potential at the end of the cooler region).

The raising and lowering of the gate leads to ions being released in to the laser line in discrete temporal bunches. This allows for a gating procedure to be applied whereby only the photons which are measured at the time of arrival of the ion bunch are counted. This method means that background photons, which are present due to other phenomena such as scattered laser light, are for the most part ignored in the measurement. Compared to the method where the ion beam is continuous, the background level is a factor of $\approx 10^4$ lower which means that much more difficult measurements are made instantly possible [48].

The cooler also has optical access at many points allowing for ‘optical pumping’ whilst the ions are within the cooler. The technique of optical pumping (which will be discussed further in Chapters 7 and 8) allows experimentalists access to previously unreachable atomic transitions from metastable states. The cooler is the ideal place to do this since the ions spend more time in the cooler than anywhere else in the beam line and therefore have a higher chance of being excited in to a new metastable state by a secondary laser. As discussed later in Section 8.1, optical pumping within the cooler has been found to successfully depopulate the ground state of yttrium [49].

5.5 Beam Optics

For high beam currents, the beam can be tuned by the use of various tuning elements down the line and monitored on a removable Faraday cup. Several such devices are present throughout the beam line in order to create a good tune down the whole line. Where beam currents decrease below the range of these devices (for example when using radioactive beams) the user can make use of the several MagneTOF devices. These fast timing counting detectors are ideal for measurements of beam currents on the sub-pA scale. Furthermore, if an isotope of interest

has a short-lived radioactive state then it is possible to make use of a silicon detector which can be lowered in to the line at the switchyard (see Figure 5.1 for reference) in order to ensure the highest possible beam transport efficiency out of the IGISOL and in to the experimental hall. The observed half-life on these detectors can also help with identification of the contents of the beam.

Chapter 6

The Laser Spectroscopy Station

6.1 Light Collection Region

The Light Collection Region (LCR) is the point of measurement for the setup and is shown schematically in Figure 6.1. At this point, the ion/atom beam (depending on the experimental setup) overlaps with the spectroscopic laser beam. The ions are accelerated through a tuning voltage, applied through a x1000 TREK 609E-6 high-voltage amplifier so as to Doppler shift them in to resonance with the laser. Should the experiment require a measurement on the atomic state of the isotope, the ion beam then passes through a charge exchange vapour (usually potassium or sodium) which neutralises the beam. The fluorescence photons from the de-excitation of hyperfine states are measured by a segmented photomultiplier tube which sits at 90° to the propagating ion/atom beam. To ensure a high level of detection efficiency, photons are collected by a lensing system which focuses them on to the photomultiplier tube. Upon detection, the photomultiplier tube generates a logic pulse which is sent to the data acquisition system and processed as described in Subsection 6.2.

In order to ensure correct alignment of the ion beam with the laser, there is a 1 mm aperture in the light collection region which can be placed in to the beam

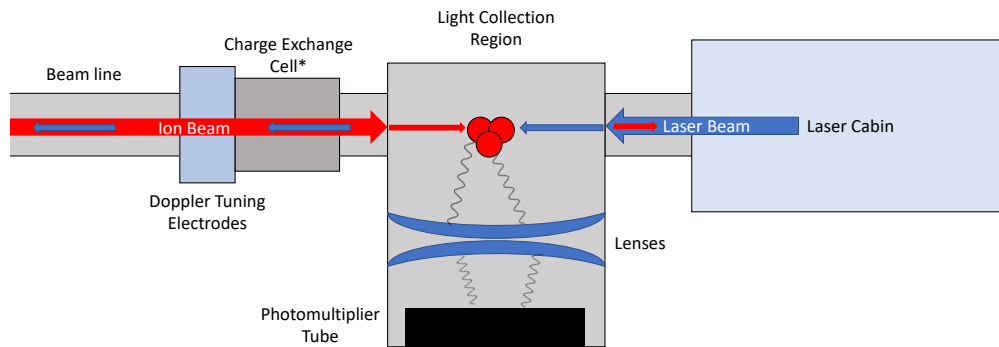


FIGURE 6.1: A schematic of the laser spectroscopy line at JYFL in plan. *The Charge Exchange Cell is removable and is only present in the beam line during experiments in which spectroscopy takes place on the atom, rather than the ion.

line. Tuning both the ion and laser beams through this aperture guarantees good alignment and therefore maximises spectroscopic efficiency.

The largest contribution towards background counts is scattered photons from laser light entering the photomultiplier tube. In order to decrease the amount of detected laser scatter, the laser line contains baffles either side of the LCR which reduces the amount of contaminating photons incident in the photomultiplier tube.

6.2 DAQ

In 2017, a new data acquisition system was installed in the laser spectroscopy beam line at JYFL. Unlike the previous data acquisition, which relied on hardware gating in order to gate on the time of arrival of an ion bunch, this new data acquisition saves information for each and every count registered in the photomultiplier tube. The signals from the photomultiplier are passed through a Fast Timing Amplifier and the resultant pulses are processed by a Constant-Fraction Discriminator so that only pulses occurring due to detection events are recorded. The pulses are

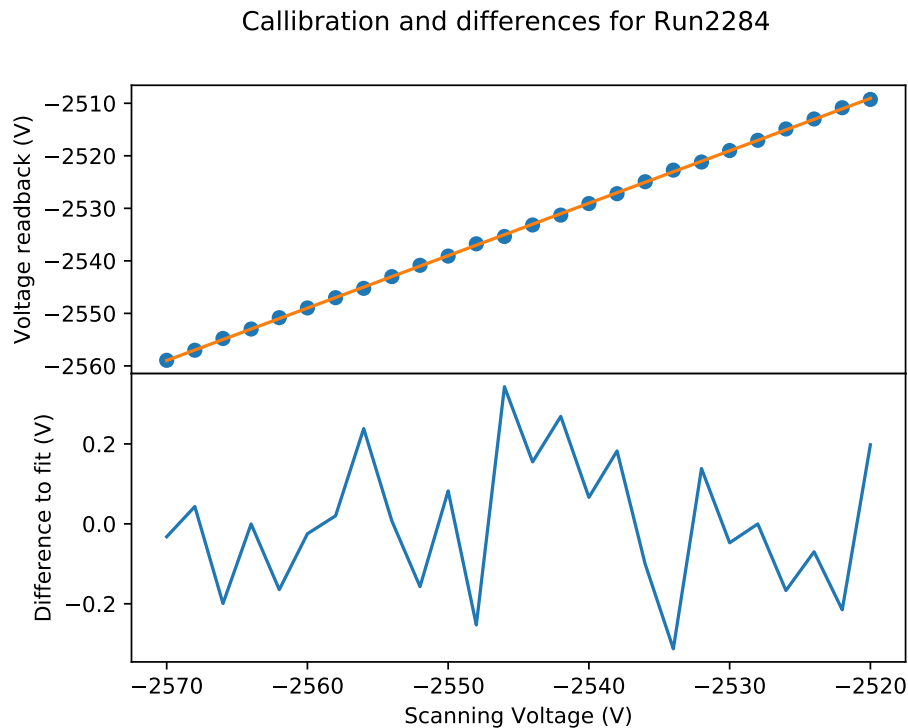


FIGURE 6.2: An example linear calibration for a scan of ^{99}Y

then time-stamped by a Cronologic TimeTagger 4-2G Time-to-Digital-Converter with a 500 ps single-shot resolution [50].

In order to scan over a hyperfine structure, the data acquisition applies a tuning voltage to the line by sending a voltage between -4 V and 4 V which is then amplified by a 1:1000 voltage amplifier. To ensure correct calibration, a scan over all voltage steps is performed before each measurement and the actual applied voltage for each step is read out through a 1:1000 voltage divider and a Keysight 34465 digital multimeter. A linear calibration can then be applied to each voltage channel during offline analysis, ensuring a high accuracy in the calculated Doppler shifts (see Figure 6.2).

Similarly, the voltage of the cooler is recorded using a Keysight 34465 digital multimeter used in tandem with a 1:10000 voltage divider. This value is recorded alongside the wavemeter readout of the laser frequency in the calibration files. As

explained in Section 5.4, the data acquisition also controls the cooler release. This enables one bunch (or otherwise, if chosen by the user) to be released for each voltage step. The setup is able to change the voltage applied to the laser line by 5 kV in less than 200 μ s, meaning that the normal ≈ 2 V steps used online are applied quickly enough to ensure no issues within the experimental requirements [50]. For each voltage step, a bunch is released in to the laser line from the cooler and accelerated towards the LCR for fluorescence detection. The program will then change the voltage applied to the line and repeat.

Once the program has reached the final voltage of its cycle, the voltage returns to the first value and the scan repeats. Unlike the previous data acquisition system, the new DAQ is capable of scanning multiple voltage regions within the same run. This ‘track’ system allows the user to select multiple scanning ranges which can be hundreds of volts apart and will skip over any voltages which are not selected whilst it performs its sweep. This is extremely helpful to the running of an experiment since it can allow multiple scanning regions to be measured within the same run file, hence decreasing any effect in experimental drifts when taking these measurements separately which could occur when taken hours apart.

For each photon detected, a line of data is written to a .csv file containing an absolute time stamp, the line voltage which was applied to the LCR (or CEC if using) at the time of detection, the bunch number, the segment of the photomultiplier tube in which the photon was detected and the time it was detected relative to the release of the bunch from the cooler. By creating a plot of the counts observed across all channels with respect to the time they were measured after cooler release, one may establish a time of flight (TOF) for the ion bunch (as seen in Figure 6.3). The benefit of this new software gating means that the user may optimise the time gates in the post-experiment analysis with more flexibility than before. Counts outside of such a TOF gate are disregarded, since there is no

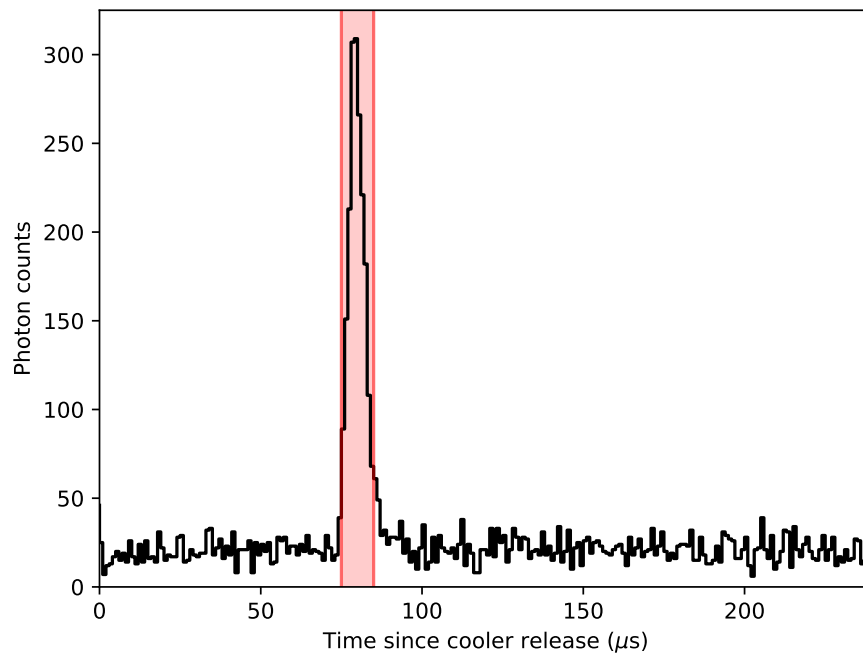


FIGURE 6.3: An example of a time gate applied offline to data taken for ^{98}Y . Here, only data within the shaded region - corresponding to the time of flight of the ion bunch - is accepted. A large portion of data is disregarded since it contains only background counts.

ion bunch in front of the photomultiplier tubes and therefore these contain only background counts.

To this end, a program has been written as part of this work which converts this raw data in to voltage-counts or frequency-counts column data which can then be used for the purposes of fitting and, thus, the extraction of hyperfine parameters. The program accounts for the calibration of the set voltages (as recorded in the calibration file) as well as the voltage of the cooler and the set point of the laser (which are both read separately at the start of each run in order to negate effects due to experimental drifts). The user may alter the TOF gates within the program in order to find the optimum values for signal to background reduction. For use in the Doppler shift calculations, the program reads in a database of precisely measured atomic masses as published in the Atomic Mass Evaluation 2016

[51] which, alongside the voltage calibration, ensures a precise Doppler shift is calculated for each set voltage.

6.2.1 Scanning Across Zero Tuning Volts

With the upgrades to the new data acquisition system, it is now possible to perform scans of hyperfine structure on different polarities. As a test of any systematic effects caused by changing polarity, offline measurements of the hyperfine structures of stable molybdenum isotopes were performed such that by changing the frequency of the laser for each run, the spectra could be measured across different voltage ranges.

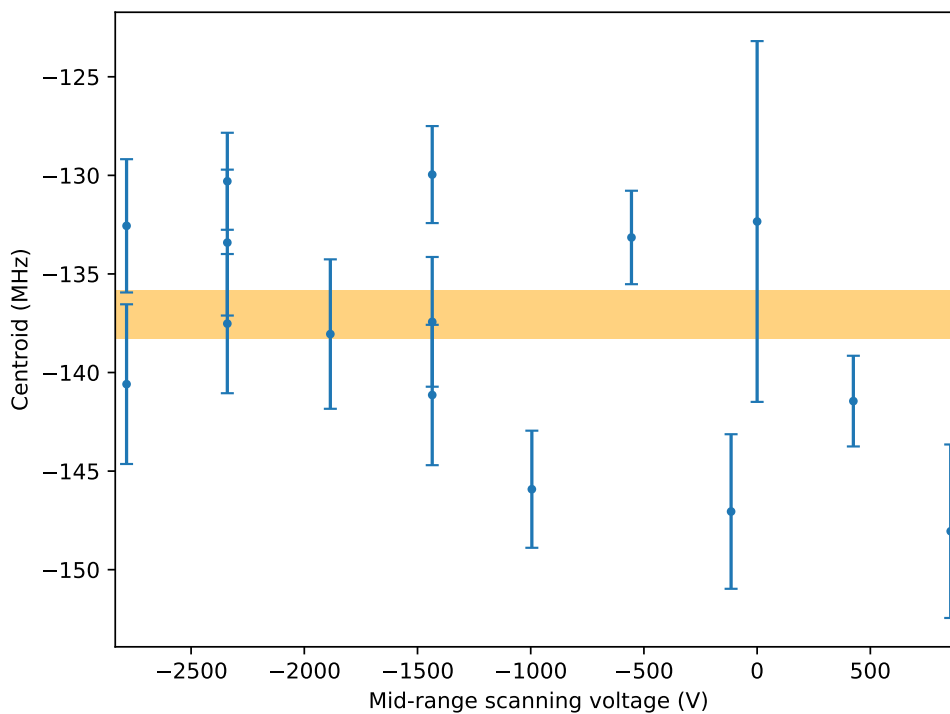


FIGURE 6.4: The fitted values for the centroid for ^{98}Mo (an $I = 0$ state) as the scanning range is changed in voltage. Note that for some of these data points the scanning range crosses 0 V. The shaded region shows the weighted average value of the centroids and its appropriate error.

To begin, the single peak structure of ^{98}Mo ($I = 0$) was measured as a simple test for any evidence of a shift in the centroid of the peak for varying voltages. Figure 6.4 shows the fitted peak position in ^{98}Mo for different scanning voltages, either side of 0 V. The shaded orange band shows the error margin on the weighted average of the fitted centroid positions. Since only few measurements were taken for positive volts, a conclusion on the presence of any systematic changes on centroid positions due to scanning on opposite polarities is inconclusive. Furthermore, drifts in experimental conditions can cause changes in the observed frequency of the peaks and so to combat this ^{95}Mo was measured since it exhibits hyperfine splitting and so any changes of peaks relative to each other may be examined.

The hyperfine structure of ^{95}Mo ($I = 5/2$) on the $J = 1/2 \rightarrow 1/2$ transition at 293 nm was measured for positive and negative scanning voltages. As well as measurements of the structure where the whole scanning range lies on one polarity, several measurements were taken in such a way that the scanning range would cross 0 V. For these scans, any effects from the change in polarity would manifest in an alteration of the hyperfine splitting. Figures 6.5 and 6.6 show the measured spectra of ^{95}Mo and the fitted hyperfine parameters, respectively. No apparent effect in either the fitted A_u parameter or the centroid of the structure is seen for these tests, giving good confidence in the ability to scan structures on either side of 0 V.

For some of these measurements, the scanning voltage was set up in such a way that the frequency location of one of the hyperfine peaks coincided with zero scanning volts as part of a second test of these effects. When a resonant peak occurs at $V_{\text{tune}} = 0$, the ion beam is on resonance for the whole journey down the laser line and hence, in some cases, was pumped out before photon detection could occur. Whilst the peaks were fitted with free intensities (rather than forced to Racah intensities), the lower statistics on these peaks could have some effect on

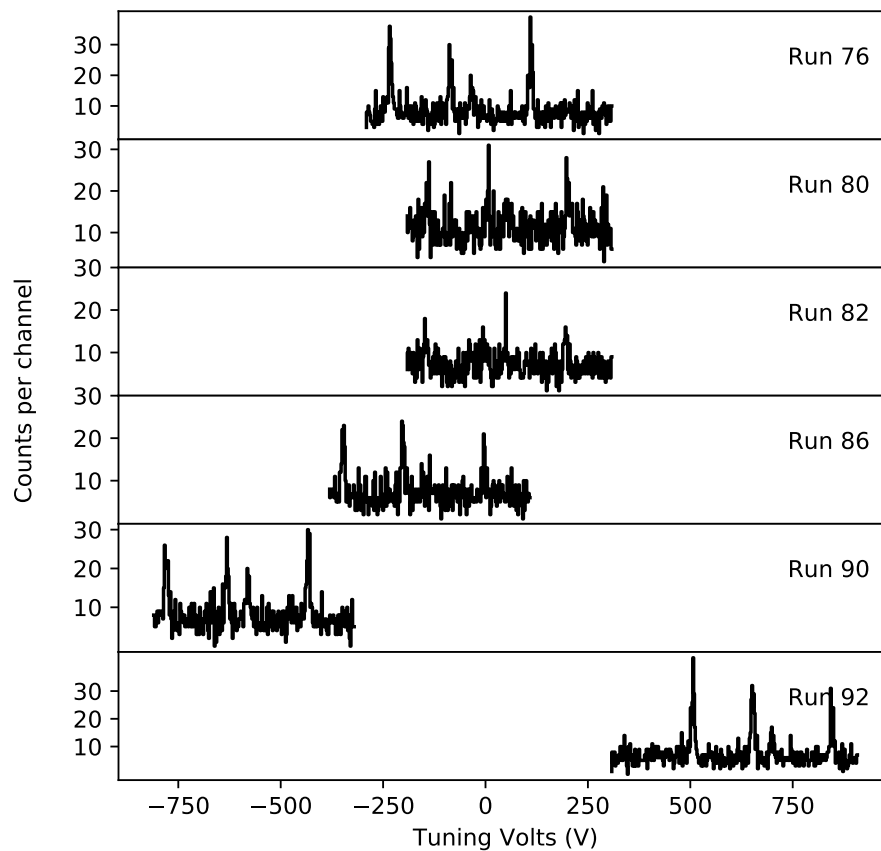


FIGURE 6.5: The measured spectra of ^{95}Mo .

the fitted values.

In summary, the possibility of scanning hyperfine structures on either side of 0 V seems promising and would be of great use to experimental measurements since this enables the possibility to scan large ranges without relocking a laser, allowing for both better accuracy and faster measurements. Whilst so far this possibility looks promising, it is recommended that more systematic investigations of the effect of such scans, particularly on simpler structures in order to be conclusive.

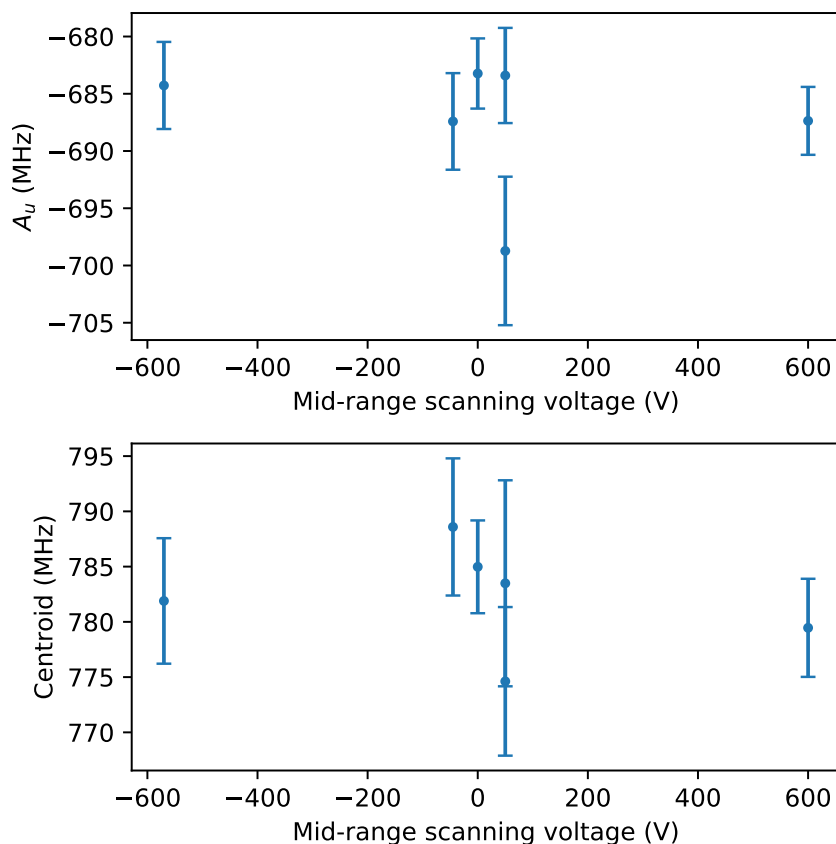


FIGURE 6.6: The fitted values for the centroid and A_u values for ^{95}Mo as the scanning range is changed in voltage. For all data points except $V_{\text{scan}}=600$ V, the scanning range crosses 0 V.

6.3 Laser Systems for Performing Spectroscopy

6.3.1 High-Precision Continuous Wave Lasers

The spectroscopic laser light for this work was provided by a Matisse 2 DS dye laser, which was recently added to the group's laser lab. The large range of tunability provided by dye lasers alongside their long-term stability to within MHz is essential for running online laser spectroscopy experiments. In this subsection, the basic operation principles of the dye laser are discussed.

The dye laser is pumped by a Verdi diode-pumped solid-state laser which acts to excite the molecules within a liquid dye. The pumping laser light repeatedly

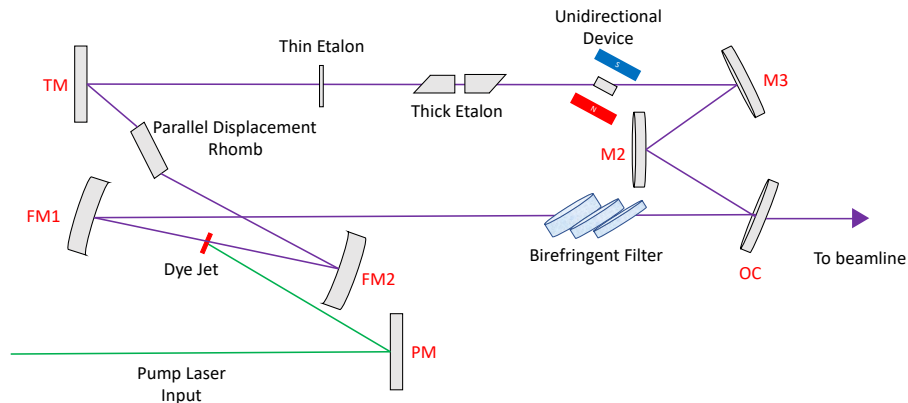


FIGURE 6.7: The dye laser cavity of a Matisse 2 DS Dye Laser. This figure is based off the figure from Ref [52].

promotes electrons from the ground state in to a level of higher energy until a population inversion is achieved. For each experiment, the laser dye is chosen in such a way to maximise the emission of light in the required frequency range. The absorption and emission profiles of several dyes are readily available in the technical data sheets provided by their production companies. One major drawback of the use of a dye as a gain medium inside of a laser is the instability of the dye molecules when exposed to high-powered light for a long period of time. For this reason, the dye (which is dissolved into a solvent) is repeatedly pumped through the laser in the form of a thin jet on to which the laser light is focused. Within the cavity of the laser (see Figure 6.7), the mirrors are placed to create the bow-tie arrangement which allows for the light to make multiple passes through the gain medium. Appropriate mirror sets must be selected for each wavelength range since their reflectivity is dependent on the wavelength of the incident light.

Unidirectional Device

The cavity is arranged in a ring configuration allowing the generation of travelling waves, which is important in order to achieve single-mode operation since two counter-propagating monochromatic beams overlapping causes spacial hole burning. However, this arrangement allows propagation of laser radiation in both the clockwise and anti-clockwise directions. In order to prevent lasing in the unwanted direction, a unidirectional device is placed in the laser path. The unidirectional device consists of a crystal plate inside a strong magnetic field. Propagation through this plate will cause a change of several degrees to the polarisation of the electric field. The field experiences a second polarisation effect when interacting with mirror M2, which is out of the plane of polarisation. Reflection out of this plane causes a rotation of the polarisation vector which is dependent on the direction of the laser propagation. In the counter-clockwise case, the effect is equal and opposite to the effect from the unidirectional device; if the field is propagating in the clockwise direction these effects are cumulative and the field will suffer losses at each Brewster surface due to a decrease in transmission [52].

Mode selection

The cavity of the dye laser allows travelling waves with frequency peaks separated by $\Delta\nu = c/L$ where L is the cavity length. In order to select only one of these frequencies, the laser makes use of several frequency selective elements within the cavity. The first of these elements is the Birefringent Filter (BiFi). The BiFi allows for a broad-range frequency selection which sets the laser up to an approximate wavelength of operation, further elements are then used to choose the frequency more selectively. The BiFi in the Matisse 2 DS consists of three quartz plates of varying thicknesses which are stacked upon each other. As the laser light travels through these plates, its polarisation will be rotated and the magnitude of such a

rotation is dependent on the wavelength of the travelling wave. There are therefore only a finite number of wavelengths which will experience no reflective losses at the Brewster angles within the laser cavity after transmission through the BiFi. Tuning of the BiFi is then simple to achieve through a small rotation of the plates.

A second frequency-sensitive piece of equipment present in the laser cavity is the thick etalon. The thick etalon is formed of two prisms aligned such that their bases are parallel (see Figure 6.7) with an air gap between. The position of one prism is controlled by the use of a piezoelectric actuator which allows for the size of this air gap to be altered. For this reason, the thick etalon is also referred to as the piezo etalon. Working in tandem with the gross frequency selection of the BiFi, selection of the appropriate distance between the two glass prisms allows for the selection of a particular laser mode of operation since the constructive or destructive interference at each prism surface is a function of their separation [53].

The combination of both the BiFi and the thick etalon is not enough to guarantee the single-mode operation of the laser and so the thin etalon works to provide a more selective range of frequencies. The thin etalon has a free spectral range of about 250 GHz, compared to the ≈ 20 GHz of the thick etalon. The horizontal tilt of the thin etalon (with respect to the laser beam) is controlled by a step motor [52]. To ensure the laser is operating at the correct wavelength, the frequency of the light is measured by a HighFinesse WSU/10 wavemeter [50] and tuned by moving the tuning mirror (TM in Figure 6.7) which changes the cavity length.

6.3.2 Laser Stabilisation

A full scan of a hyperfine spectrum can take place over a large range of time, from a few minutes to a few hours. In order to accurately take a measurement of the

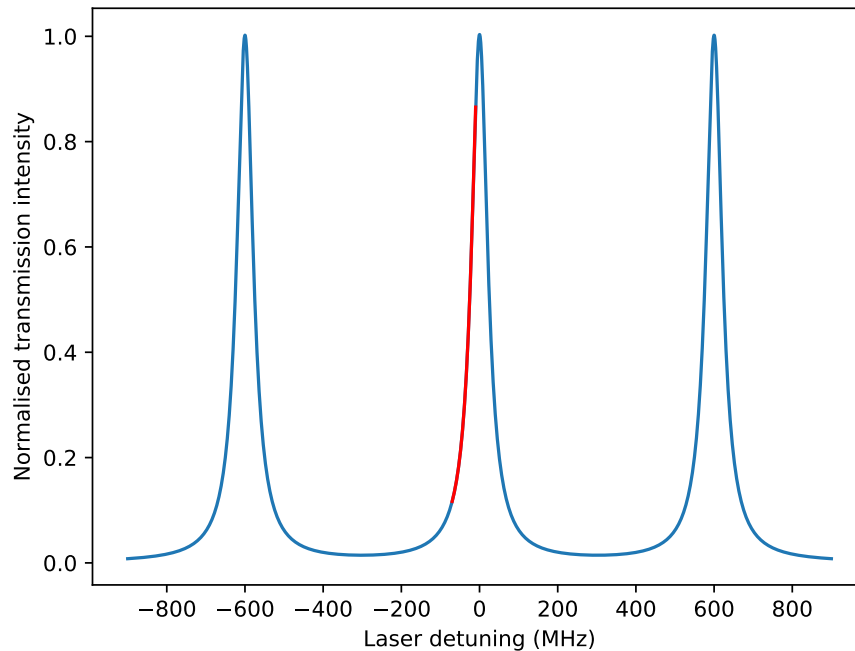


FIGURE 6.8: An example transmission profile of a reference cavity. The laser frequency can be ‘locked’ to the side of a transmission peak, shown in red. This figure is based off the figure from Ref [52].

frequency of the hyperfine peaks, it is important that the frequency of the spectroscopic laser remains as stable as possible across the length of the scan. To achieve this, the laser is ‘locked’ to the transmission of a reference cavity. Specifically, the laser frequency is locked to the side profile of a peak in the spectrum (see Figure 6.8) and a control loop feeds information to a fast piezo actuator, upon which a mirror is mounted. A change in intensity of the reference peak corresponds to a change in the frequency of the laser. For example, if the laser were locked to the left hand side of a peak, an increase in intensity would correspond to an increase in frequency and a decrease in intensity would correspond to a decrease in laser frequency. An accurate measurement of this therefore allows for the appropriate signal to be sent to the fast piezo and the laser frequency to be restabilised to the required value. It is important to note that this method only works for small perturbations in laser frequency such that the change in laser frequency is smaller than the reference peak shape. For larger changes in frequency (known as losing

the laser lock), manual intervention is required [52].

6.3.3 Pulsed Lasers

The laser light utilised for the pumping part of the two spectroscopic schemes in this work was provided by a pulsed Ti:Sa laser and transported down in to the cooler-buncher via a series of mirrors from the upstairs laser laboratory. The Ti:Sa laser functions in a very similar way to the dye laser; it is a tunable laser which operates in a bow-tie cavity and is pumped by an external laser. The Ti:Sa differs to the dye laser mainly by the use of a Titanium:Sapphire crystal as a gain medium. The high thermal conductivity of a Ti:Sa crystal allows for high laser power to be generated, without the worry of degrading the molecules in a dye. The Ti:Sa crystal also benefits from having a large intrinsic emission spectrum and so enables access to a wide variety of laser wavelengths (with the appropriate mirror sets matched to the wavelength of the light in order to maximise reflection) [52].

The pulsed nature of the laser light provided by the Ti:Sa laser allows for a higher efficiency in frequency doubling (see below) since the efficiency of the second harmonic generation is related to the power of the incoming light. Since the Ti:Sa light is pulsed, its energy is deposited over a short amount of time and therefore has a higher instantaneous power.

6.3.4 Second Harmonic Generation

In order to produce light in the ultra-violet region of the electromagnetic spectrum, laser light from the dye laser is passed through a frequency doubling crystal, which is chosen to meet the needs of the specific spectroscopic scheme. Such a crystal is a so-called ‘non-linear’ material whose properties can alter the polarisation of the

light.

For a linear material, the induced polarisation, \vec{P} is given by

$$\vec{P} = \epsilon_0 \chi^{(1)} \vec{E}, \quad (6.1)$$

where $\chi^{(1)}$ is the linear susceptibility and \vec{E} is the electric field [54]. For a non-linear material, each component of the polarisation ($k = (x, y, z)$) is given by

$$P_k = \epsilon_0 \left(\chi_{ik}^{(1)} E_i + \chi_{ijk}^{(2)} E_i E_j + \dots \right), \quad (6.2)$$

where the values $\chi^{(n)}$ are the tensors of the n^{th} order non-linear process. For an input field given by $E_i = \epsilon_i \exp(-i\omega t) + c.c.$, the second order polarisation term is

$$P_k = \chi_{ijk}^{(2)} \left(\epsilon_i \epsilon_j \exp(-2i\omega t) + \epsilon_i^* \epsilon_j^* \exp(2i\omega t) + \epsilon_i^* \epsilon_j + \epsilon_i \epsilon_j^* \right). \quad (6.3)$$

The interaction of electromagnetic radiation with a non-linear material will then therefore create a component of the resulting field with a frequency of exactly double that of the input field. This phenomenon is an effect named Second Harmonic Generation (SHG). A similar result can also be shown for higher order harmonics, though it is assumed that these effects are small enough, in most cases, to be negligible.

In the case of the spectroscopic laser light, the frequency doubling is achieved by making use of a ‘WaveTrain’ frequency doubling cavity where laser light propagates in a ring and can therefore make multiple passes through the SHG crystal to increase the efficiency of the doubling [55]. For the pulsed laser system, the WaveTrain is not necessary since the instantaneous power of each laser pulse is sufficiently high to achieve a reasonable doubling efficiency.

Chapter 7

Collinear Laser Spectroscopy of Yttrium Isotopes

It has long been known that the $A \approx 100$ region of the nuclear chart demonstrates a strong onset of deformation. Due to this, the region has been the subject of many studies over the last two decades [8, 49, 56–62] which have shown that this large onset of deformation is present in many isotopic chains at $N = 60$ with the phenomenon appearing to reach its apex in the yttrium chain.

In 2007, a campaign began to study the shape transition within the yttrium chain by collecting hyperfine spectra from the semi-magic nucleus ^{89}Y up to ^{102}Y [8]. The mean-square deformation parameter, $\langle\beta_2^2\rangle$, was extracted from a measurement of the mean-square charge radius by

$$\delta\langle r^2\rangle^{A,A'} = \delta\langle r^2\rangle_{\text{sph}}^{A,A'} + \langle r^2\rangle_{\text{sph}} \frac{5}{4\pi} \delta\langle\beta_2^2\rangle, \quad (7.1)$$

where $\langle r_{\text{sph}}\rangle$ is the radius of a spherical nucleus with equal volume. It was shown that as neutrons are added above the $N = 50$ shell closure, nuclei become slowly more deformed as the neutron number increases towards $N = 60$ (see Figure 7.1).

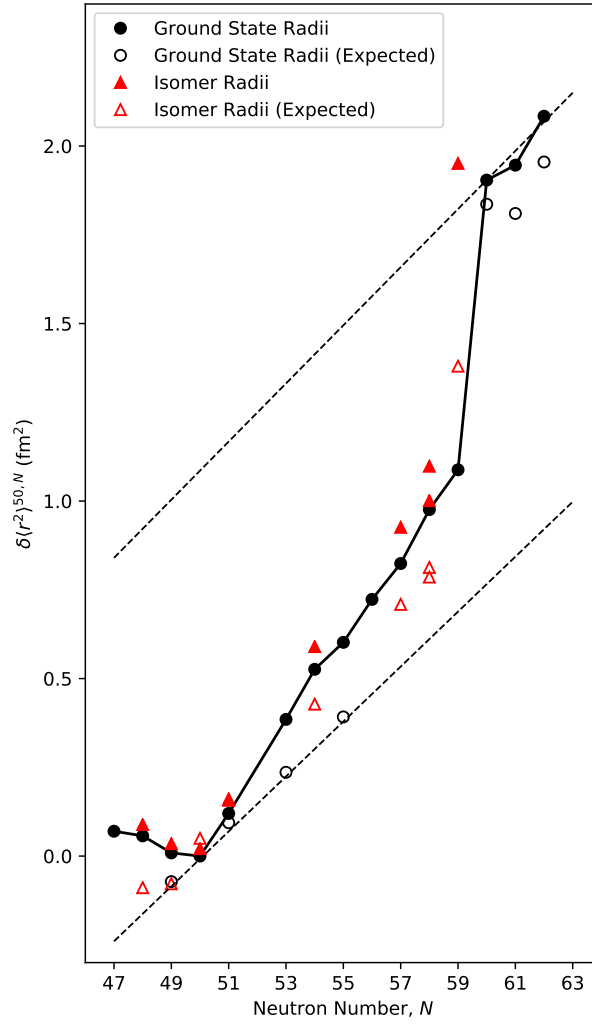


FIGURE 7.1: The radii of the Y isotopic chain as measured in Ref [8]. The dashed lines represent the expected charge radii from the liquid droplet model for $\beta_2 = 0$ and $\beta_2 = 0.43$.

Complementary measurements of the quadrupole moments allowed for the extraction of the quadrupole deformation parameter, $\langle\beta_2\rangle$, by

$$Q_0 \approx \frac{5Z \langle r^2 \rangle_{\text{sph}}}{\sqrt{5\pi}} \langle\beta_2\rangle (1 + 0.36 \langle\beta_2\rangle), \quad (7.2)$$

which further demonstrated the weakly oblate nature of these nuclei and, with comparison to the values of deformation extracted from the radii, help to demonstrate an increase in β -softness with increasing neutron number (as seen from the

departure of the trend from the mean-square charge radius predicted by the deformed liquid drop model, Figure 7.1).

Above $N = 60$, a sudden shape transition manifests as the nuclear shape changes from this softly deformed oblate shape to a rigid prolate deformation. Critically, it was found that at the site of the shape transition there was a clear shape coexistence between the ground state of ^{98}Y and its 241 keV isomer. The isomer ^{98m}Y was particularly interesting since the static quadrupole deformation (extracted from the hyperfine B parameter) alone did not fully account for this change of shape and the deformation appeared to be much more dynamic in nature than those isotopes both above and below the point of transition.

The knowledge of nuclear spin is critical to the measurement of nuclear properties by laser spectroscopy and whilst unambiguous spin identification is normally possible through laser spectroscopic measurements, in the case of the 2007 study a $J = 0 \rightarrow J = 1$ transition at 363 nm was used. Whilst efficient as a probe of magnetic and quadrupole moments, such a transition contains a maximum of only three hyperfine resonances (as seen in Figure 7.2) and hence a nuclear spin has to be assumed in the fitting process. At the time of the publication of the study, the spin was assumed to be either 4 or 5 and so a set of hyperfine parameters were extracted for each of these possible spins. Whilst the lack of a positively assigned nuclear spin caused ambiguities in the nuclear electromagnetic moments, the presence of the shape coexistence remained a certainty since the measured isomer shift (the change in transition frequency, and hence a measure of the change in nuclear size, between a ground state and its isomer) was largely unaffected.

More recent studies from the GAMMASPHERE array claimed a more likely spin as high as $I = 7$. The work found that the feeding of certain levels in ^{98}Zr (which was the basis for the previous assignment of $I = (4, 5)$) was not observed.

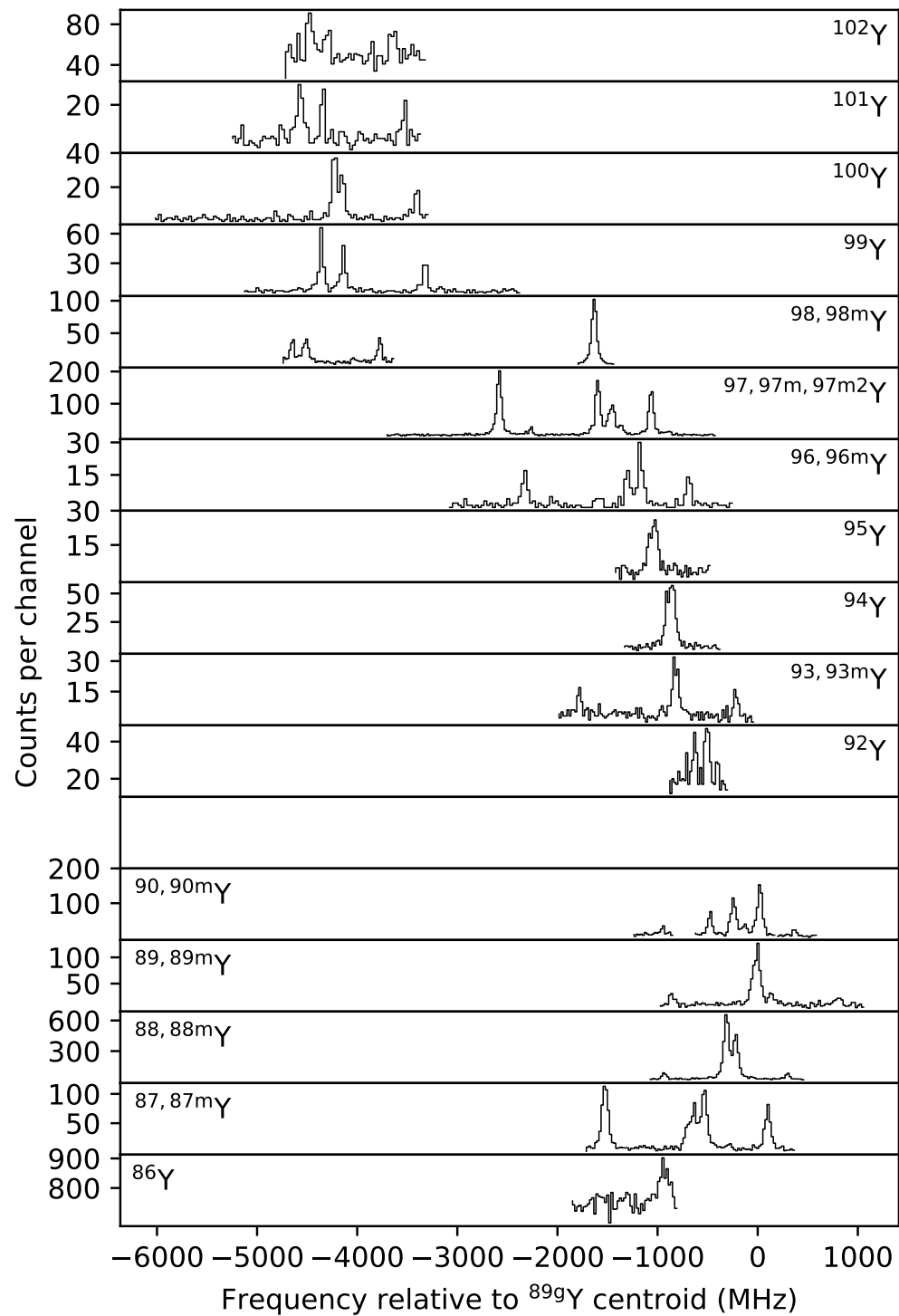


FIGURE 7.2: The previously measured spectra of Y isotopes on the $J = 0 \rightarrow J = 1$ line. It is important to note the sudden shift in centroid between ^{98}Y and its isomer, clearly demonstrating the shape coexistence [8].

It was, however, observed that the β decay of ^{98m}Y populated a state in ^{98}Zr with a spin of 7^+ as well as having a 43% branch to a 6^+ state which is consistent with an allowed Gamow-Teller transition. The conclusion was therefore that the state was likely to have a spin of $I = (6, 7)$ rather than $I = (4, 5)$ [63].

To investigate this hypothesis further and to unambiguously characterise the shape coexistence, a campaign began at the IGISOL-IV facility to measure the spin of ^{98m}Y using laser spectroscopic techniques. During this experiment, an electronic transition between higher J states than those used previously was probed, since such a transition yields many more hyperfine resonances. Whilst this effect causes the transition to be much less efficient (since the resonant counts are split across more peaks), accurate calculations of the spectrum in each scenario allow for a spin assignment without the need to measure every peak. Furthermore, yields in the region are expected to be four times higher for IGISOL-IV compared to IGISOL-III [64] which enables a much higher count rate than in previous measurements. This chapter presents this work and subsequent analysis.

7.1 Experimental Setup

Since the main fallback of the previous study on the 363 nm line was the inability to measure all nuclear parameters without assuming knowledge of at least one, a different methodology was adopted in this study. Instead of probing a $J = 0 \rightarrow J = 1$ transition, a transition was chosen between two states of higher J value, the $J = 2 \rightarrow J = 1$ transition at 321 nm. The resulting hyperfine spectrum would then include sufficient peaks to determine the nuclear spin of the excited state alongside its magnetic and quadrupole moments. This transition has previously been used to successfully measure the spin of ^{100m}Y in a paper published in 2010 [56].

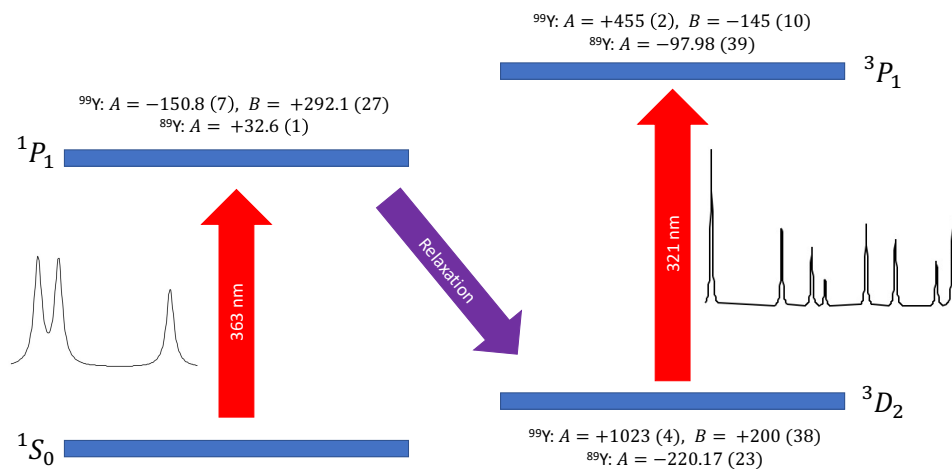


FIGURE 7.3: The pumping scheme for yttrium. Electrons are excited on the 363 nm line before relaxing in to the $3D_2$ state for spectroscopy. All hyperfine parameters [8, 56] quoted are measured in MHz.

In order to prepare the radioactive ion beam for study on this new line, the configuration of the electrons first had to be manipulated to probe a transition which starts from a metastable state. To achieve this, the technique of optical pumping was adopted; the ions are excited with laser light whilst they are held in the cooler before de-exciting in to a long-lived isomeric state which then forms the basis of the spectroscopic line (see Figure 7.3).

In this particular case, the ions were excited within the cooler on the same 363 nm line as used in the last experiment by laser light provided by a pulsed Ti:Sa laser. From the excited $1P_1$ state, the electrons relax into states of lower energies for which a transition is allowed. Should electrons de-excite back in to the ground state, they are re-excited in to the $1P_1$ state and the pumping process repeats. Where the electron decays in to a state which cannot decay to the ground state, the electron cannot be re-excited by the pumping laser light. Should this happen for any other state than the $3D_2$ state of interest, the ion is then no longer available for spectroscopy (unless the electron can move to the ground state through collisional de-excitation or similar mechanisms). It is therefore important

to choose a pumping scheme which preferentially decays in to a suitable state in order to maximise spectroscopic efficiency. The most intensely populated state (other than the ground state) from the decay of the 1P_1 state is the 3D_2 level with a branching ratio (BR) of approximately 36%, calculated from the tabulated Einstein A coefficients in atomic databases [65]. This is calculated as the ratio of the transition strength of the $J = 1 \rightarrow J = 2$ (with a wavelength of 377.6 nm) and the sum of all other transition strengths from the 27517 cm^{-1} level except the ground state (since any de-excitation in to this state is re-excited by the pumping laser), that is

$$\text{BR} = \frac{A_{378}}{A_{374} + A_{378} + A_{512} + A_{733} + A_{745} + A_{788}}, \quad (7.3)$$

where A_i is the Einstein A coefficient to the transition from the 1P_1 state with wavelength i nm.

Upon arrival at the light collection region, the ions are further excited from this 3D_2 state to the 3P_1 state, this time with laser light provided by a frequency-doubled continuous wave dye laser.

7.2 Initial Predictions

In order to identify the spin of the system, calculations of the hyperfine structure in the $^3D_2 \rightarrow ^3P_1$ transition of ^{98m}Y were made for spin values ranging from 4 – 9. Such predictions can be performed by making use of the hyperfine parameters of the electronic levels in ^{98m}Y extracted from fitting the spectrum and the ratios between each of these parameters for the relevant transitions in the pumping scheme, all of which are available from previous work on this isotopic chain. As shown by Ref. [56], the hyperfine anomaly in yttrium is known to be less than 1% and it

I	$A(^1P_1)$	$B(^1P_1)$	$\delta\nu^{98g,98m}$
4	-88.21(48)	+325.4(32)	-2747(2)
5	-73.64(39)	+339.8(34)	-2735(2)
6	-63.13(33)	+349.6(36)	-2727(2)
7	-55.22(29)	+356.7(37)	-2721(2)
8	-49.05(25)	+362.0(38)	-2717(2)
9	-44.12(23)	+366.2(39)	-2713(2)

TABLE 7.1: A table of the fitted hyperfine parameters for ^{98m}Y on the 363 nm $^1S_0 \rightarrow ^1P_1$ transition for nuclear spins ranging from $I = 4 - 9$. Hyperfine parameters are quoted in MHz.

is thus a reasonable assumption that these ratios remain constant across the chain.

To begin, A and B parameters and the isomer shifts were extracted from the previous ^{98}Y data (measured from the $^1S_0 \rightarrow ^1P_1$ line) for each of the spins concerned and extended to higher spin values. The results of this fitting process can be found in Table 7.1.

To calculate the ratio between parameters in the relaxation phase of the pumping scheme, values were taken from Refs. [8] and [56]. In these experiments, data have been taken which allow for the extraction of the A parameter in ^{89}Y and both the A and B parameters in ^{99}Y for both the 1P_1 and the 3D_2 states. A measurement of the B parameters is not possible for ^{89}Y since it is known to have a nuclear spin of $I = 1/2$ and therefore the hyperfine spectrum exhibits no quadrupole splitting. The data from Ref. [56] also allow us to calculate a ratio of the hyperfine parameters for the $^3D_2 \rightarrow ^3P_1$ transition. The A ratios deduced from values measured in ^{89}Y are

$$A(^1P_1)/A(^3D_2) = -0.1481(5) \quad , \quad A(^3P_1)/A(^3D_2) = +0.445(2), \quad (7.4)$$

and the B ratios, from ^{99}Y are

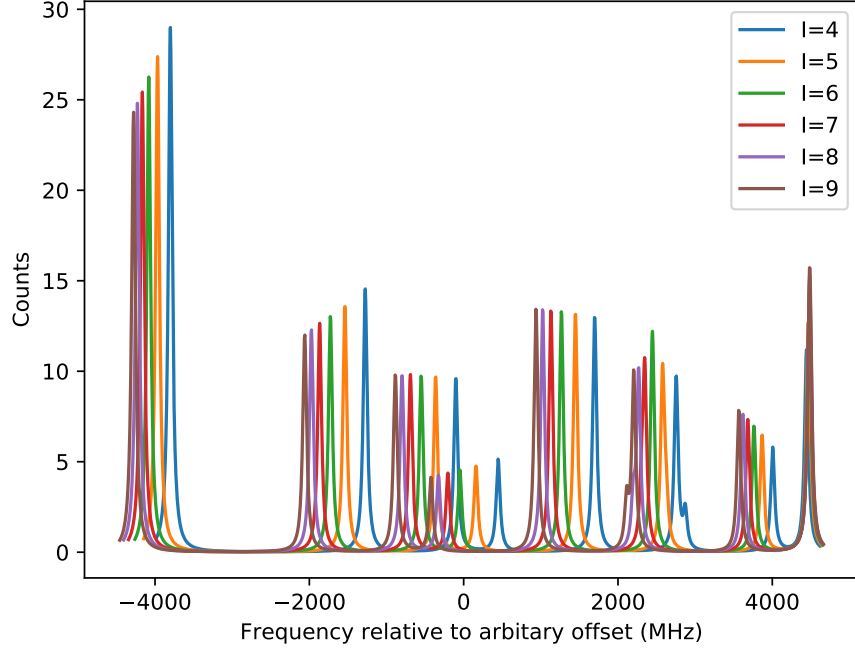


FIGURE 7.4: The calculated hyperfine spectra for ^{98m}Y for $I = 4 - 9$. It is clear that a confirmation of the nuclear spin is viable from the measurement of the left hand peak only.

$$B(^1P_1)/B(^3D_2) = +1.46(28) \quad , \quad B(^3P_1)/B(^3D_2) = -0.73(15). \quad (7.5)$$

Knowledge of the ratios of the atomic F factors of the 321 nm and 363 nm transition (which are available from the gradient of the King plot shown in the 2010 literature [56] and the F factor quoted in the 2007 study [8]) also allow for the estimation of the isomer shift in the system since

$$\frac{\delta V_{363}^{A,A'}}{\delta V_{321}^{A,A'}} = \frac{F_{363} \delta \langle r^2 \rangle^{A,A'}}{F_{321} \delta \langle r^2 \rangle^{A,A'}} = \frac{F_{363}}{F_{321}} = m_{\text{KP}}, \quad (7.6)$$

where m_{KP} is the gradient of a King plot. With these ratios and the fitted data from Table 7.1, the hyperfine spectrum of ^{98m}Y for the spectroscopic transition can be calculated and used to predict the locations of the resonance peaks.

Figure 7.4 shows the simulated spectra for ^{98m}Y for spins $I = 4 - 9$. It can be seen that the spin of the system can be inferred by considering the relative spacings of all of the hyperfine peaks. More than this, it is clear that it is not necessary to measure the entire hyperfine structure of the 321 nm line to achieve a spin assignment since the location of many peaks for differing nuclear spins are well resolved. With enough accuracy in the predictions, the spin of the system can be determined from the location of only the most intense peak. Since a $J = 2 \rightarrow J = 1$ transition demonstrates a splitting of the fine structure into many hyperfine levels (therefore distributing the total resonant counts across many hyperfine peaks), this method of measurement is of high importance since the ability to concentrate on narrow scan regions allows a high efficiency, thus enabling a sufficient measurement despite the much lower count rate.

7.3 Measurement of ^{98m}Y on the 321 nm Line

Based on the measurements thus far, calculations were performed to determine the necessary tuning voltages to Doppler shift the bunches of yttrium into resonance with the laser light for the second most intense hyperfine peak (which is predicted to have almost the same location for each spin and so the most certain location to search). The scans were set up (with a track measuring the ground state resonance once every three ‘sweeps’ in order to ensure that count rates were maintained), yet the measurement proved unfruitful. In fact, a measurement lasting one whole shift (8 hours) yielded no signal for the peak as shown in Figure 7.5.

In the hopes of finding a solution to the problem that had presented itself, the 363 nm data were further re-examined. The calculated Racah intensities show a doublet of roughly equal height in the spectrum (see Figure 7.6) and, since the fitting could not be constrained by any fixed ratios due to the absence of hyperfine splitting in a $J = 0$ state, it seemed possible that these peaks were cross-identified.

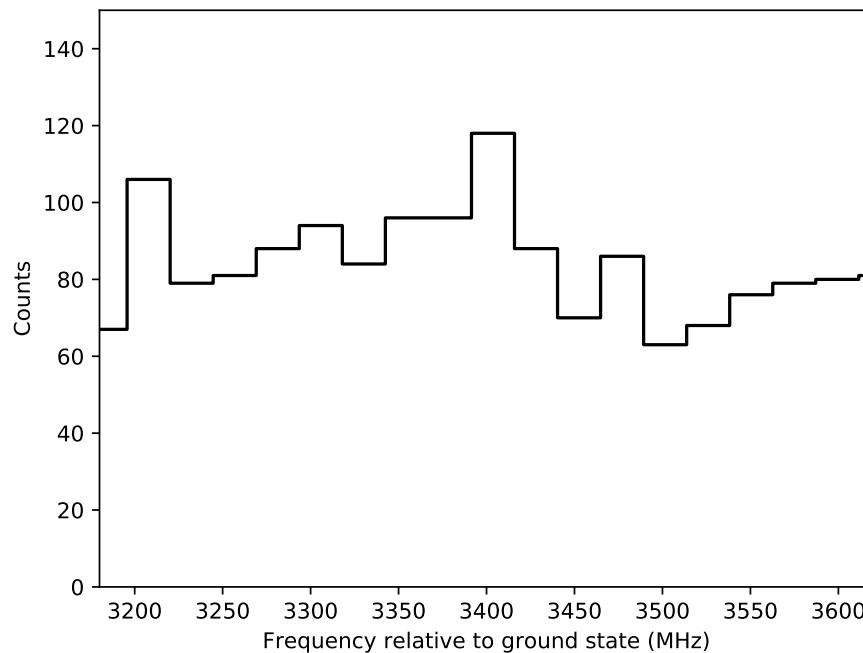


FIGURE 7.5: The measured spectra of ^{98m}Y showing no discernable counts where the peak was expected to occur.

Table 7.2 presents the possible permutations of peak orders. A $J = 0 \rightarrow J = 1$ transition allows for three hyperfine transitions and therefore $3! = 6$ possible orderings in frequency. Scenario e) is the previously assumed situation. Scenarios a), b) and c) are unlikely since they would give moments which are not in line with other isotopes in the chain as reported in previous work [8]. Scenario f) also does not seem likely since it would give a much smaller magnetic moment than expected from the trend in the chain. The most obvious scenario to try first would then be Scenario d). With this new peak matching, the previous data were refitted for spins 4 – 9 (see Table 7.3, which replaces 7.1), hyperfine simulations were created once again and the experimental settings recalculated. The new simulations can be found in Figure 7.7. The newly calculated hyperfine spectra show that it is still possible to determine the nuclear spin without the need to measure a full hyperfine spectrum.

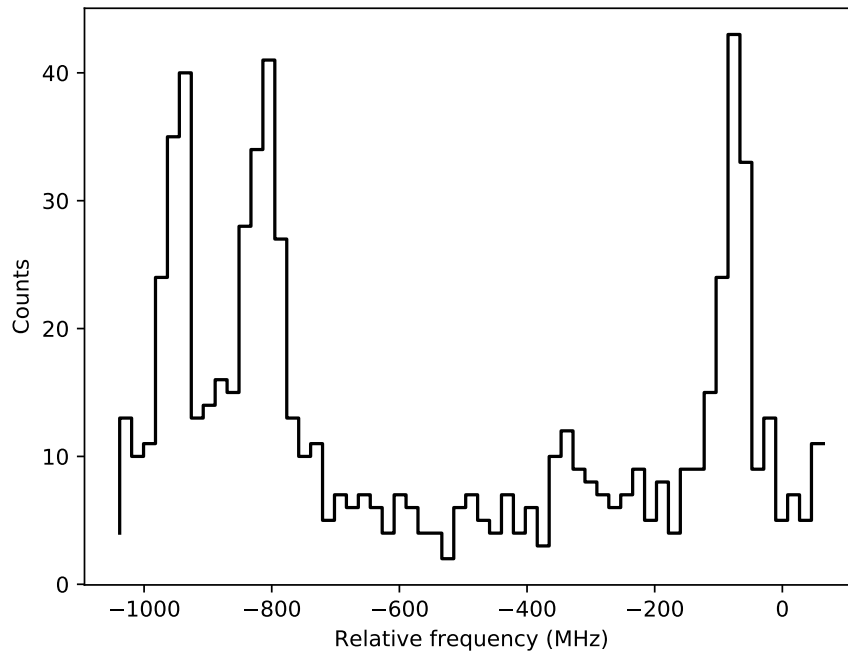


FIGURE 7.6: The previously measured ^{98m}Y spectrum from 2007.

After just one hour of scanning, the first hyperfine resonance was successfully measured, confirming that there was indeed a peak misidentification in the 2007 work. During the final hours of the experiment, a further three hyperfine resonances were measured several times, each with a reference track of the ground state. These reference measurements mean that a well defined measure of the isomer shift could be extracted without concerns of experimental drifts between

TABLE 7.2: The fitted values for all six permutations of the peaks (the spectrum on which these fits were performed is shown in Figure 7.6) for a spin of $I = 7$ as suggested by Urban *et al.* [63], possibilities for other spins with Scenario d) can be found in Table 7.3. The ν values are relative to an arbitrary constant. Peak 0 represents the $F = 7 \rightarrow F = 6$ transition, Peak 1 represents the $F = 7 \rightarrow F = 7$ and Peak 2: $F = 7 \rightarrow F = 8$.

Scenario	Peak Order	A (MHz)	B (MHz)	$\delta\nu^{98g,98m}$ (MHz)
a)	0 1 2	+60.58(29)	+293.7(37)	-563.2(17)
b)	0 2 1	+1.84(27)	-876.3(40)	-595.9(17)
c)	1 0 2	+53.37(27)	+519.6(39)	-569.3(17)
d)	1 2 0	-44.37(27)	+572.8(39)	-634.7(17)
e)	2 1 0	-55.22(29)	+356.7(37)	-640.8(17)
f)	2 0 1	-16.21(27)	-866.5(40)	-608.0(17)

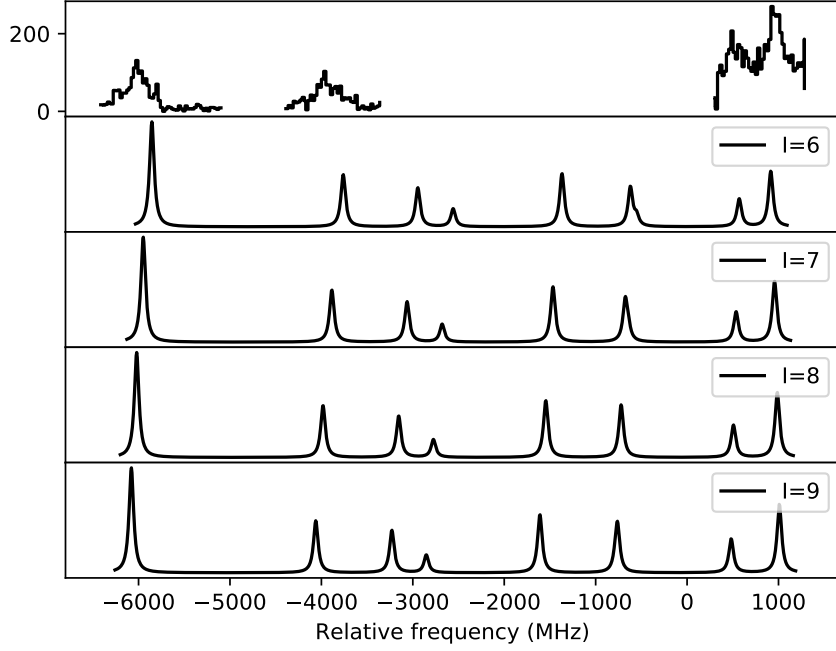


FIGURE 7.7: A comparison of the measured hyperfine spectra for ^{98m}Y to the calculated spectra which replaces Figure 7.4. The result shows ambiguity in the nuclear spin, which could align with $I = 7$ or 8.

measurements. The location of these peaks, as predicted by Scenario d), discounts the possibility of any other scenario and therefore removes any ambiguity arising from the order of the peaks in the extraction of the nuclear moments and the charge radius (Figure 7.7).

With the resonances successfully measured and the peak order of the 363 nm

I	$A(^1P_1)$	$B(^1P_1)$	$\delta\nu^{98m,98g}$
4	-68.19(45)	+508.8(34)	-2737(2)
5	-57.98(37)	+537.7(36)	-2727(2)
6	-50.30(31)	+557.9(38)	-2720(2)
7	-44.37(27)	+572.8(39)	-2715(2)
8	-39.66(24)	+584.3(40)	-2711(2)
9	-35.85(21)	+593.4(41)	-2708(2)

TABLE 7.3: The newly fitted hyperfine parameters for ^{98m}Y on the 363 nm $^1S_0 \rightarrow ^1P_1$ transition which replaces Table 7.1. All hyperfine parameter values are quoted in MHz.

spectrum unambiguously defined, the measured 321 nm data were compared to the simulated positions of the hyperfine peaks for extraction of the nuclear spin. Upon comparison of the measured data to the calculated spectra, there seemed to be ambiguity in the final result. Since the simulation of the hyperfine structure in ^{98m}Y relies so heavily on the precision of the ^{99}Y data measured on the 321 nm line, due to the need to extract the B ratio from this spectrum and the atomic F factor from the King plot, the original data files were re-examined. An inspection of the data showed that two of the hyperfine peaks in the spectrum critical to the fitting process (since extraction of the B ratio requires at least 4 peaks, or 5 where the ratio of the A parameters is not left to vary) had not been fully measured, leading to uncertainty in the fit itself (see Figure 7.8). A remeasurement of the hyperfine spectrum of the 321 nm transition of ^{99}Y would enable a more precise calibration of the ratios and of the King plot, therefore allowing a more confident spin assignment in ^{98m}Y .

7.4 Remeasurement of ^{99}Y

In October 2019, the hyperfine spectrum of ^{99}Y was remeasured on the 321 nm line. A total of six hyperfine peaks were successfully measured (Figure 7.9) which allowed for a more complete measurement of the previous spectrum, including the addition of an extra peak for more statistics. In the fit, all hyperfine parameters were left unconstrained so that the ratios of the parameters could be extracted from the results and used in the analysis of ^{98m}Y . The results of this fit are shown in Table 7.4.

To calculate the isotope shift in ^{99}Y , measurements of the ground state of ^{98}Y were taken. Once fitted, the centroids of these $I = 0$ peaks then allowed for a calculation of the shift between ^{98}Y and ^{99}Y and in turn ^{89}Y and ^{99}Y through

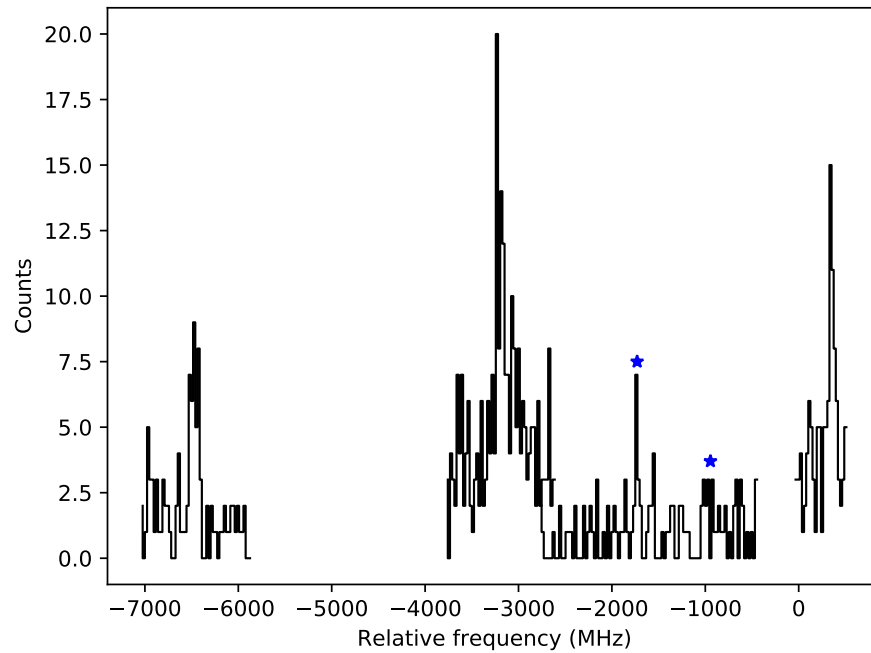


FIGURE 7.8: The previously measured ^{99}Y spectrum as measured on the 321 nm line. The blue stars indicate the approximate position of the two not yet fully measured peaks.

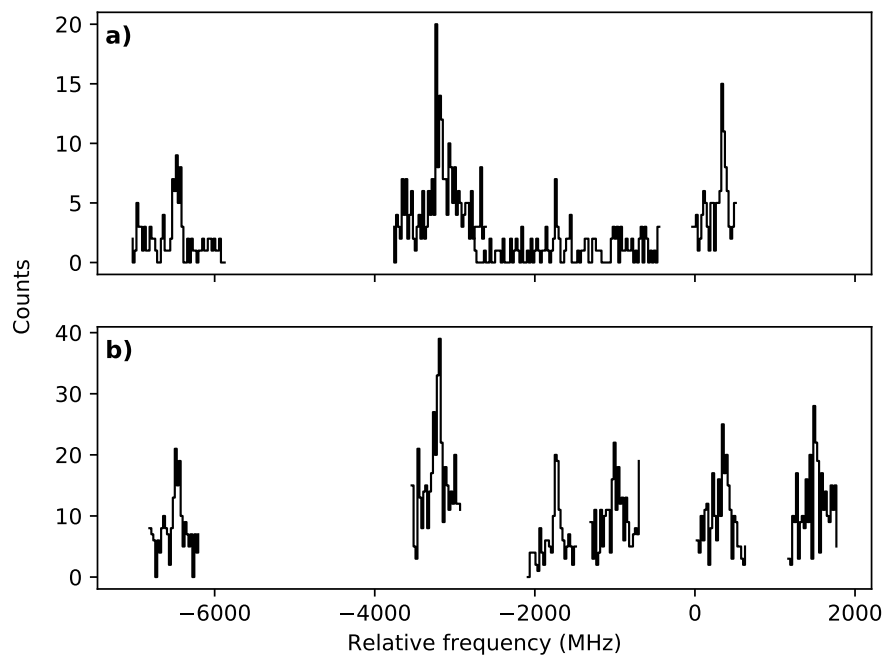


FIGURE 7.9: The previously measured ^{99}Y spectrum on the 321 nm line (a) compared to the 321 nm spectrum which was measured in late 2019 (b).

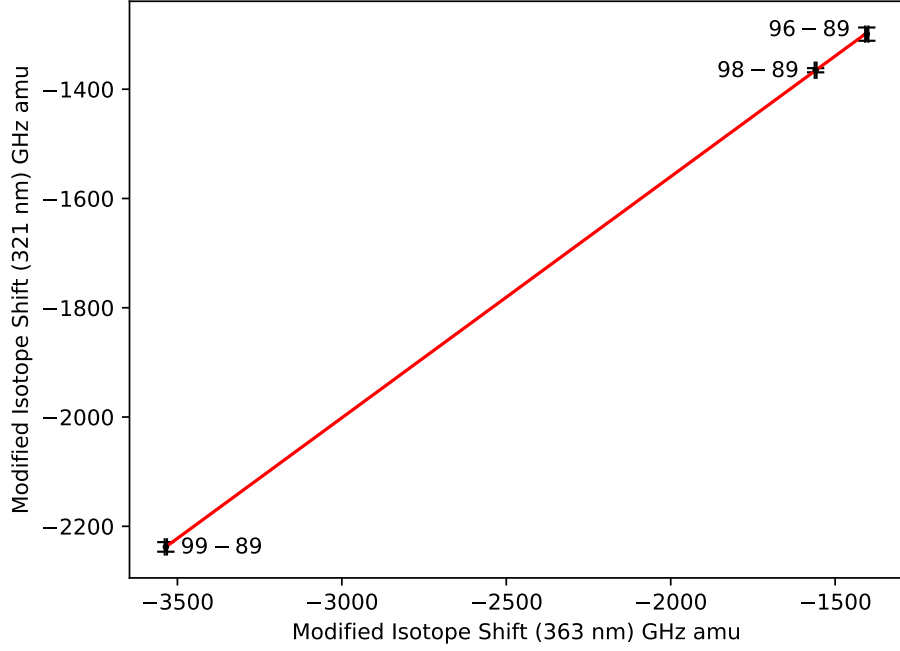


FIGURE 7.10: The King plot for the computation of the F and M factors of the 321 nm atomic transition.

$$\delta\nu^{89,99} = \delta\nu_{\text{lit}}^{89,98} + \delta\nu^{98,99}, \quad (7.7)$$

where $\delta\nu_{\text{lit}}^{89,98}$ is the isotope shift between ^{89}Y and $^{98g.s.}\text{Y}$, taken from literature [56]. This isotope shift can then be utilised in the King plot technique as described above. A fit was performed using the *ODR* package within SciPy [41] which gave new atomic factors of $F = -1404(25)$ MHz·fm $^{-2}$ and $M = +112(18)$ GHz·amu compared to the previous factors of $F = -1343(25)$ MHz·fm $^{-2}$ and $M = +107(17)$ GHz·amu. The new King plot is shown graphically in Figure 7.10.

The newly measured values are presented in Table 7.4. The newly calibrated

TABLE 7.4: The previously and newly measured hyperfine parameters of ^{99}Y . All values for hyperfine parameters are in MHz.

I	$A(^3P_1)$	$B(^3P_1)$	$A(^3D_2)$	$B(^3D_2)$	$\delta\nu^{89,99}$
5/2 (old)	+455 (2)	-145 (10)	+1023 (4)	+200 (38)	-2550 (10)
5/2 (new)	+459 (4)	-118 (10)	+1028 (3)	+176 (25)	-2549 (10)

hyperfine ratios ($A_l/A_u = +2.237$, $B_l/B_u = -0.149$) were then used in both creating new calculations of the hyperfine parameters of ^{98m}Y in order to correctly assign the spin and to constrain the ratios of the hyperfine parameters in the fitting procedure of ^{98m}Y (see Section 7.5 below).

7.5 Re-analysis of ^{98m}Y on the 321 nm Line

With the newly measured hyperfine ratios from ^{99}Y and the F_{321} factor recalibrated, a complete calculation of the hyperfine spectra of ^{98m}Y on the 321 nm line can be performed for multiple spin values, as shown in Figure 7.11. It is clear with the improved calibration that the measured peaks align best with the spectrum as calculated for $I = 7$.

Furthermore, since multiple peaks were successfully measured, a simultaneous fit of all measured hyperfine peaks from the isomeric state of ^{98m}Y was performed according to the equation

$$\gamma = \zeta + \alpha_u A_u + \beta_u B_u - 2.237\alpha_l A_u - (-1.490)\beta_l B_u, \quad (7.8)$$

where $\zeta = \nu_{g,s} + \delta\nu^{g.s.,m}$ is the centroid of the isomeric structure built from the isomer shift $\delta\nu^{g.s.,m}$ (which is shared between all runs) and $\nu_{g,s}$, the centroid of the ground-state peak which was measured as a track for each run (and is free to vary to account for any experimental drifts).

In Table 7.5, the results from the fitting procedure are compared to those calculated with the new hyperfine ratios and the atomic F_{321} factor. As with the graphical representation, it can be seen that these values seem to only agree for all parameters when $I = 7$ and therefore this spin value is assigned to the state. A further evaluation of the confidence in this assignment is discussed in the section

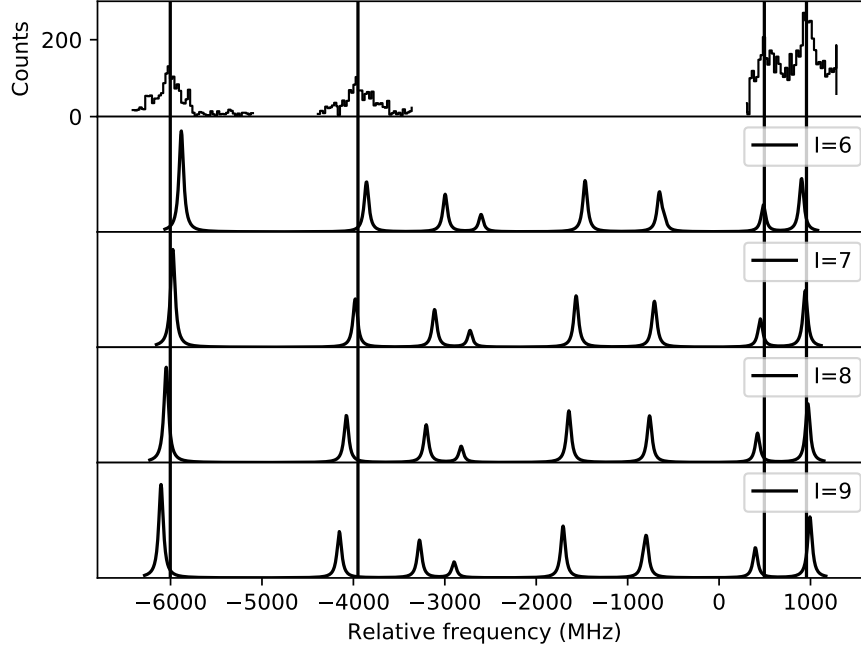


FIGURE 7.11: The fully corrected simulation of the hyperfine structure of ^{98m}Y , created using the newly measured F and M factors and B ratio from ^{99}Y , all from this work. Solid vertical lines indicate the locations of the peaks.

below.

The final results of the upper state hyperfine parameters on both the 321 nm line and the 363 nm line with the new peak reassignment and $I = 7$ are presented in Table 7.6.

TABLE 7.5: LHS: The fitted hyperfine parameters of ^{98m}Y for possible spins $I = 6 - 9$ for measurements on the 321 nm line. RHS: The parameters calculated for the 321 nm line from the measurements taken on the 363 nm line (with updated calibration) and the known ratios of hyperfine parameters. All hyperfine values are quoted in MHz.

I	$A(^3P_1)$	$B(^3P_1)$	$\delta\nu^{g.s.,m}$	$A(^3P_1)_{\text{calc.}}$	$B(^3P_1)_{\text{calc.}}$	$\delta\nu_{\text{calc.}}^{g.s.,m}$
6	+155.97 (18)	-204.3 (42)	-1267 (4)	+151.2 (12)	-226 (49)	-1200 (3)
7	+135.20 (16)	-247.7 (44)	-1204 (4)	+133.4 (11)	-232 (50)	-1198 (3)
8	+119.27 (14)	-282.5 (45)	-1155 (4)	+119.2 (10)	-237 (51)	-1196 (3)
9	+106.67 (12)	-311.1 (46)	-1116 (4)	+107.8 (9)	-240 (52)	-1195 (3)

TABLE 7.6: The newly extracted hyperfine parameters of the upper states in ^{98m}Y on the 363 nm and 321 nm lines from this work. The isotope shift for ^{98m}Y is measured against its ground state.

Isotope	A_u (MHz)	B_u (MHz)	$\delta\nu^{g.s.,m'}$ (MHz)
^{98m}Y (363 nm)	-44.37 (27)	+572.8 (39)	-2715 (2)
^{98m}Y (321 nm)	+135.20 (16)	-247.7 (44)	-1204 (4)

7.6 Extraction of Nuclear Properties

With this spin assignment and the new peak ordering, the nuclear parameters μ and Q_s could now be unambiguously extracted from the old 363 nm data by means of the ratios of hyperfine components from

$$\mu = \mu_{\text{ref}} \frac{IA}{I_{\text{ref}}A_{\text{ref}}}, \quad (7.9)$$

$$Q_s = Q_{s,\text{ref}} \frac{B}{B_{\text{ref}}}, \quad (7.10)$$

where A_{ref} and B_{ref} are the hyperfine parameters of the same atomic level in a reference isotope and μ_{ref} and $Q_{s,\text{ref}}$ are its known magnetic and quadrupole moments. In this case, the stable isotope ^{89}Y was used as a reference for the magnetic moment ($\mu_{89} = -0.1374154(2)\mu_N$, $A_{89} = +32.6(1)$ MHz [8]). ^{89}Y could not be used as a reference isotope for the quadrupole moments since its spectrum does not exhibit quadrupole splitting due to having an $I = 1/2$ nucleus and so the hyperfine B parameter of ^{90}Y was used as a reference for the extraction of the quadrupole moment instead ($Q_{s,90} = -0.125(11)$ b, $B_{90} = -23.5(15)$ MHz [8]). These extracted properties may be found in Table 7.7.

Whilst the relationship between B and Q_s is independent of I , correct extraction of B from the hyperfine spectrum is reliant on the correct spin assignment of I , just as it is with A and ν . It therefore stands to reason that the values extracted for these parameters from each of the data sets should match when the

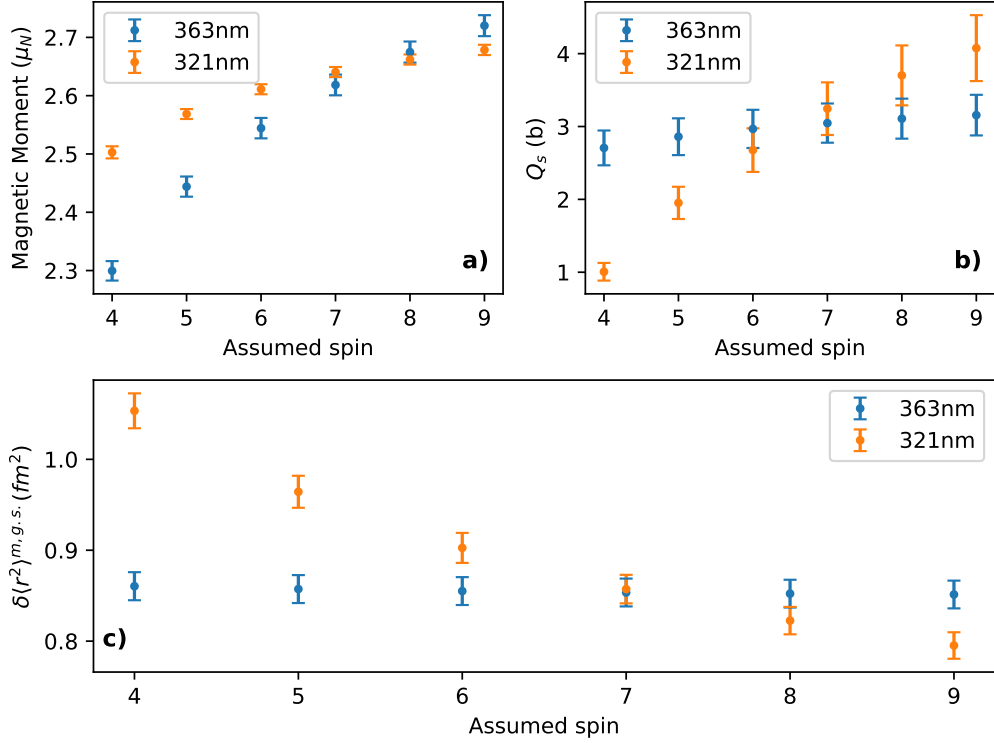


FIGURE 7.12: The extracted nuclear parameters of ^{98m}Y for various nuclear spins as measured on two different atomic lines. The extracted parameters agree best for $I = 7$.

correct nuclear spin is used in the fitting routine. Figure 7.12 shows that these parameters, extracted from the 363 nm and the 321 nm lines match best when $I = 7$ is used, again supporting the $I = 7$ assignment for this metastable state. It is important to note that the error bars in Figure 7.12 are somewhat artificially inflated due to the error on each data point containing the same error from the reference moment and hyperfine parameter. Note that in this figure, ^{99}Y had to be used as a reference for B on the 321 nm transition as the only other spectrum measured on the 321 nm line which exhibits quadrupole splitting.

TABLE 7.7: The measured nuclear properties of ^{98m}Y . The spectroscopic quadrupole moment of ^{90}Y acted as a reference for the value extracted for ^{98m}Y .

Isotope	I	μ (μ_N)	Q_s (b)	$\delta\langle r^2 \rangle^{89,A'}$ (fm^2)
^{98m}Y	7	+2.62(2)	+3.05(27)	+1.94(10)

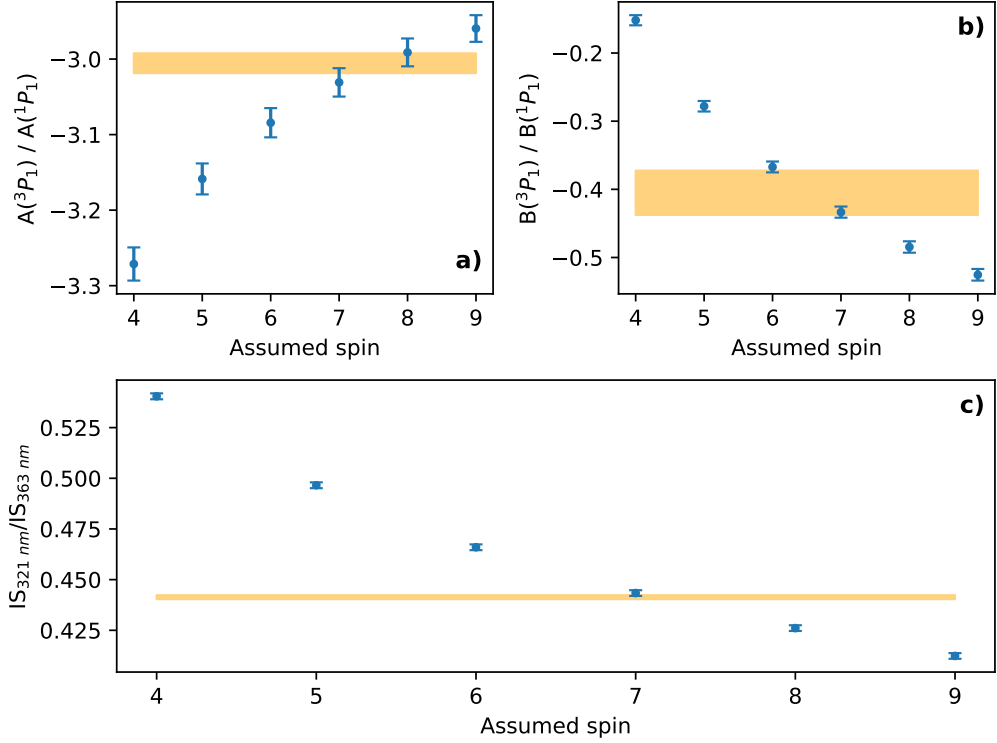


FIGURE 7.13: The ratios of A parameters (a), B parameters (b) from the 3P_1 and 1P_1 states, and isomer shifts (c) for varying spins of ^{98m}Y on the 321 nm and the 363 nm lines, shown relative to the known ratios and gradient of the King plot.

To combat these inflated errors, the atomic properties may be made use of since the ratios of hyperfine parameters between any two states should be constant across the yttrium chain, as previously stated. The ratio between the newly measured hyperfine parameters for the 3P_1 state and the values for the 1P_1 state can then be compared against the known values of these ratios: $A(^3P_1)/A(^1P_1) = -3.006(13)$ (taken from ^{89}Y as before) and $B(^3P_1)/B(^1P_1) = -0.405(33)$ (taken from ^{99}Y). This method allows for a comparison of results without the artificial inflation of error on the data points from the errors associated with reference isotope. A comparison of these values for varying spins can be seen in the top two panels of Figure 7.13 which show the ratios as calculated for various spins of ^{98m}Y and a shaded region representing the known ratio $\pm 1\sigma$. Furthermore, the ratio of isomer shifts in ^{98}Y can be compared to the gradient of the King plot directly, since its value is equivalent to F_{363}/F_{321} (Equation 7.6). The panel a) alone would suggest

a spin of 7 or 8, panel **b**) suggests 6 and 7 and panel **c**) agrees only for a spin of 7. This therefore also reinforces the assignment since all known values can only be consistent for an $I = 7$ state for the isomer in ^{98}Y .

7.7 Calculating Deformation

In order to quantify the deformation of the isomeric state, the intrinsic quadrupole moment must first be calculated. This calculation can be performed using

$$Q_0 = \frac{3\Omega^2 - I(I+1)}{(I+1)(2I+3)} Q_s, \quad (7.11)$$

where Ω is the projection of the nuclear spin along the nuclear symmetry axis. Here, we assume $\Omega = I$.

The intrinsic quadrupole moment allows for the extraction of the static quadrupole deformation parameter $\langle\beta_2\rangle$ since, for axially symmetric deformed nuclei,

$$Q_0 \approx \frac{5Z \langle r^2 \rangle_{\text{sph}}}{\sqrt{5\pi}} \langle\beta_2\rangle (1 + 0.36 \langle\beta_2\rangle). \quad (7.12)$$

Here, $\langle r^2 \rangle_{\text{sph}}$ is the charge radius of a spherical nucleus of the same volume as predicted by the liquid droplet model [32]. For ^{98m}Y , the $\langle\beta_2\rangle$ value is found to be 0.431. The change in mean-square charge radius can be described by

$$\delta \langle r^2 \rangle^{A,A'} = \delta \langle r^2 \rangle_{\text{sph}}^{A,A'} + \langle r^2 \rangle_{\text{sph}} \frac{5}{4\pi} \delta \langle \beta_2^2 \rangle, \quad (7.13)$$

where $\langle\beta_2^2\rangle$ is the mean-square quadrupole deformation. A measure of the contribution of the static deformation can be extracted from Equation 7.13 by replacing $\langle\beta_2^2\rangle$ with $\langle\beta_2\rangle^2$. Any discrepancy between the value and those measured experimentally is indicative of the presence of dynamic deformation. Such information

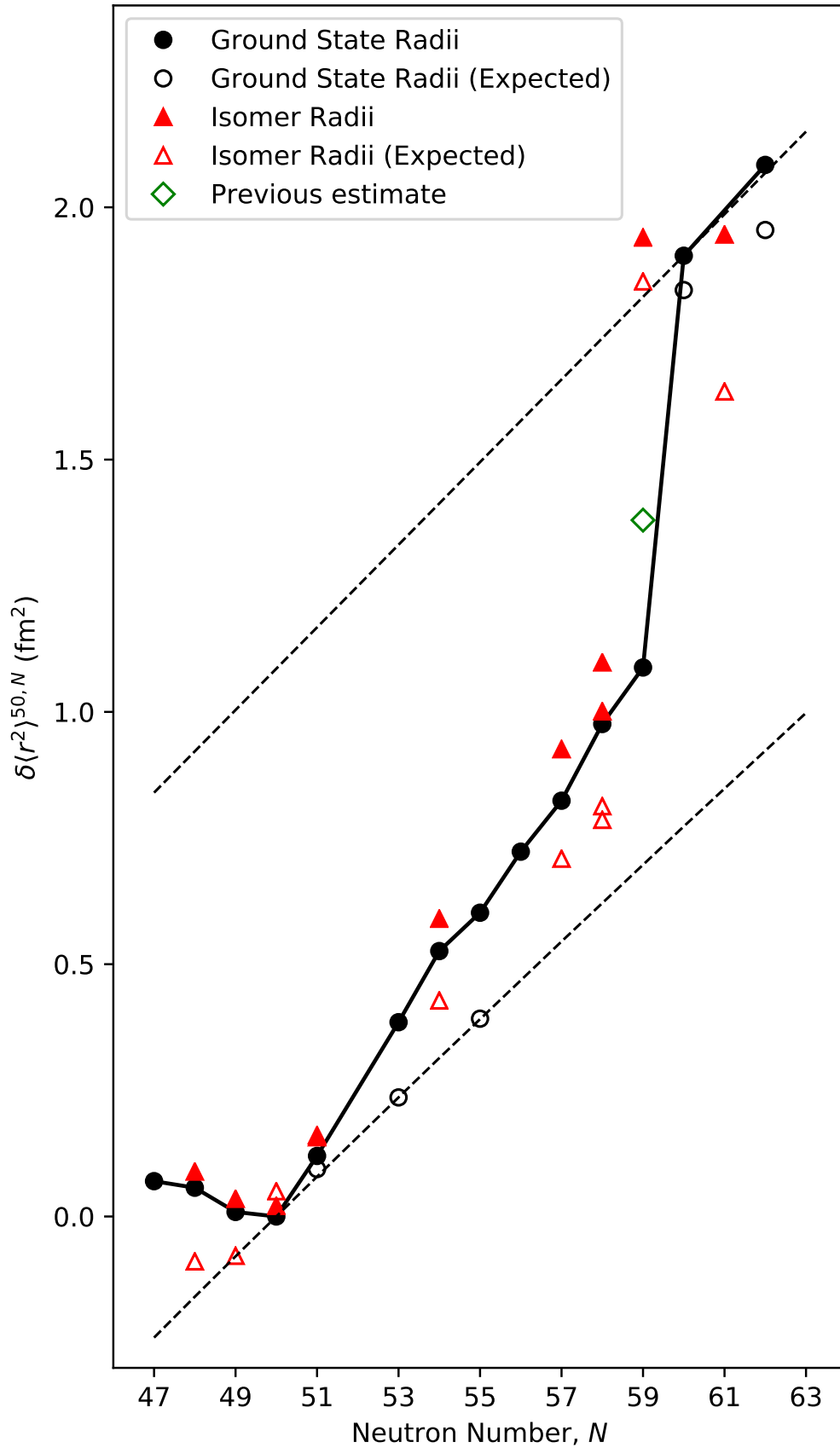


FIGURE 7.14: The measured and expected change in charge radii for the yttrium chain. The difference between the two values shows the extent of dynamic deformation present in the nucleus. The values for ^{98m}Y presented here are a correction to the values in Ref. [8]. The lower and upper dashed lines represent the isodeformation lines for $\beta_2 = 0$ and $\beta_2 = 0.43$, respectively.

is displayed in Figure 7.14.

With the previously calculated moments, ^{98m}Y was believed to exhibit a highly dynamic deformation due to an apparently large discrepancy between the static estimate of the mean-square charge radius and that measured from the isotope shift. The new assignment of peaks in the hyperfine structure presented in this work greatly changes the extracted quadrupole moment and, whilst the centroid of the structure (and therefore the extracted value of the charge radius) differs only slightly, this shows a much more static deformation in the isomer than was previously thought.

7.8 Comparison to Energy Density Functional Calculations

Calculations for the charge radii of Y isotopes from $A = 75$ to $A = 106$ have been performed using three EDFs: UNEDF0, UNEDF2 and F(Δr ,HFB). Figure 7.15 compares the results of the calculations to the nuclear parameters extracted both from this work and from Ref [8]. Several observations are clear from an examination of the graph.

Firstly, the rapid change in the shape of the nuclei is predicted at the correct location for both the UNEDF0 and UNEDF2 functionals. However, the Fayans functional does not predict an onset of deformation, rather a smooth increase in charge radius across the chain. This effect can also be seen in Figure 7.16 where the static deformation is expected to stay close to zero as neutron number increases away from $N = 50$ for the Fayans functional calculations whereas the

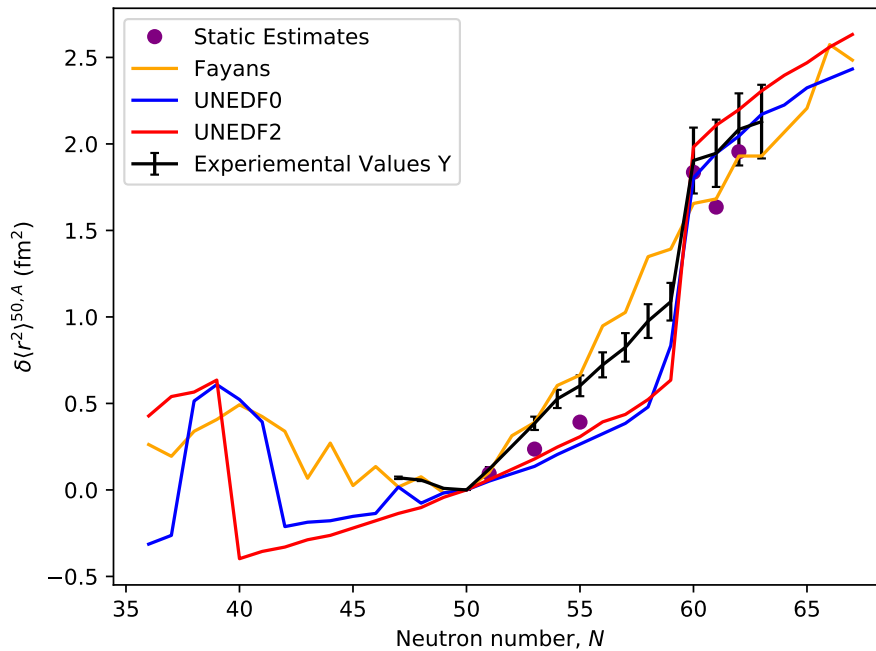


FIGURE 7.15: The charge radii of the Y chain compared to the theoretical predictions from DFT calculations.

UNEDF functionals reproduce the high onset of deformation well.

Secondly, whilst the Fayans functional matches the experimentally measured charge radii well for nuclei from to $N = 50 - 55$, UNEDF0 and UNEDF2 generate underpredictions for these values and are more comparable with the static estimates of charge radii calculated as in Section 7.7. Between $N = 55$ and $N = 60$, none of the functionals correctly predict the charge radii as the Fayans calculations continue to increase smoothly whilst the UNEDF0 and UNEDF2 calculations continue to underestimate the values.

Finally, all three functionals reproduce the charge radii after the shape change agreeing well with the measured radii within the conservative 10% error bars displayed.

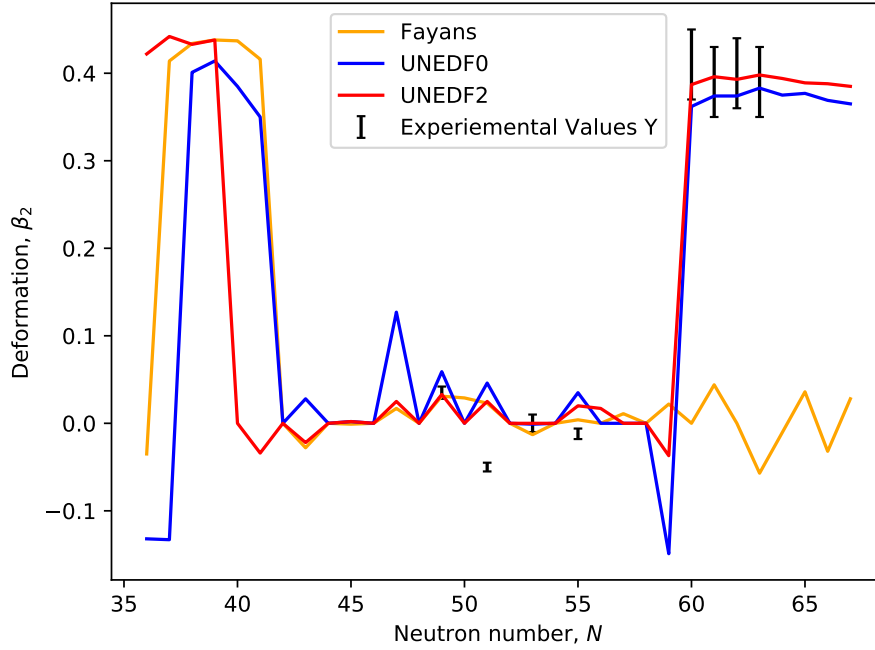


FIGURE 7.16: The β_2 deformation parameter of the Y chain compared to the theoretical predictions from DFT calculations.

A further interesting feature of these calculations is their behaviour below $N = 60$. Whilst the $F(\Delta r, \text{HFB})$ calculations fail to reproduce the onset of deformation at $N = 60$, they do recreate the kink in the charge radii observed at the $N = 50$ shell closure. On the other hand, the UNEDF functionals, which do predict the large $N = 60$ shape change, do not produce the same kink.

For odd A nuclei, such as yttrium, it is unfortunately not possible to calculate the potential energy surface unambiguously with respect to deformation due to the nature of quasiparticle blocking procedure used in the calculations. As the calculations are performed, the Nilsson orbital containing the odd particle needs to be defined - this is usually an orbital close to the Fermi surface. A large change in the deformation, e.g. from oblate to prolate as in ^{98m}Y , dramatically changes the order of the Nilsson orbitals and thus changes the blocked orbital [66]. Such plots are however possible to calculate for even-even nuclei and the surfaces for

Sr ($Z = 38$) and Zr ($Z = 40$) are shown in Appendix A. It can be seen that at $N \approx 60$, the UNEDF functionals begin to predict a potential energy minimum around $\beta_2 = 0.4$ which is concurrent with the findings of this study with Y where ^{98m}Y was found to have a deformation of $\langle\beta_2\rangle = 0.431$. In contrast, the Fayans functional predicts a minimum on potential energy around $\langle\beta_2\rangle = 0$ and hence does not predict an onset of deformation at $N = 60$.

Going forwards, the calculation of the nuclear properties of the ground and isomeric states would be an interesting laboratory with which to test the ability of large-scale Monte Carlo shell model interactions, such as A3DA-m which has been previously used to calculate the electromagnetic moments of zinc isotopes [67] and the deformation of shape-coexisting states in ^{64}Ni [68].

7.9 Conclusions

In summary, a total of five peaks in the hyperfine structure of the $J = 2 \rightarrow J = 1$ transition at 321 nm of ^{98m}Y have been measured for the first time. These measurements have allowed for a spin assignment of $I = 7$ for the isomeric state to be confirmed. Furthermore, the data confirms a peak misassignment in the previous 363 nm ($J = 0 \rightarrow J = 1$) data from literature. With the new spin assignment and peak order, these data were refit and the new electromagnetic moments extracted.

Studies of the atomic F and M factors of the 321 nm transition also showed inaccuracies in the values published in literature. To this end, a remeasurement of ^{99}Y was also performed on the $J = 2 \rightarrow J = 1$ line as a calibration of these atomic factors as well as the ratio of the hyperfine B parameters of the 3P_1 and 3D_2 states. With this isotope shift, the F and M factors were newly extracted, yielding $F = -1404(25)$ MHz \cdot fm $^{-2}$ and $M = +112(18)$ GHz \cdot amu.

With the correctly extracted electromagnetic moments, the extent of the shape coexistence in ^{98}Y could be fully quantified. The data show that the deformation of the isomeric state (which was previously thought to be very dynamic in nature) takes on a rigid, prolate shape comparable to isotopes after the $N = 60$ boundary.

Finally, the charge radii of the Y chain were compared to state-of-the-art Energy Density Functional calculations using three different EDFs: UNEDF0, UNEDF2 and F(Δr ,HFB). These results show that UNEDF0 and UNEDF2 fail to reproduce the dynamic nature of the yttrium isotopes between $N = 50$ and $N = 60$ but do predict the onset of deformation at $N = 60$. On the other hand, F(Δr ,HFB), does well at predicting the charge radii of the chain close to $N = 50$ but fails to produce the rapid change at $N = 60$. All three models compare well with charge radii measured after the shape change.

Chapter 8

Collinear Laser Spectroscopy of Niobium Isotopes

In past work which detailed the first example of optical pumping in an ion beam cooler for laser spectroscopy, a change of shape at $N = 60$, similar to that in yttrium, was measured in the niobium ($Z = 41$) chain [49]. This change differed from the one measured for $Z = 39$ in that the magnitude of the jump in mean-square charge radius was smaller in niobium and the nuclei demonstrated a considerable degree of β -softness both before and after the change, whereas the isotopes in yttrium become more rigidly deformed after the transition. Although the key isotope of ^{100}Nb , which sits at the critical point of this change, was missing from the investigation, the observation was still evident from measurements of the mean-square charge radii of ^{99}Nb and ^{101}Nb which differ significantly. This change exhibits many of the same shape properties as that in yttrium (which can additionally be extracted from the quadrupole moments), the nuclei become increasingly oblate deformed with a high level of β -softness before a sudden change to a prolate shape. As with ^{98}Y , ^{100}Nb has 59 neutrons and a low-lying isomeric state and so it is possible that a similar shape coexistence occurs in this isotope.

Just two neutrons higher, ^{102}Nb is an ideal case for the study of the nuclear structure after this shape change. Not only does it contain long-lived ground and isomeric states which make it ideal for laser spectroscopy (as in ^{100}Nb) but it is also an isotone of ^{100}Y which, as explained later in Chapter 9, has presented itself as another candidate for shape coexistence.

Previous studies of the β decay properties of ^{100}Nb have suggested nuclear spins of 1^+ and 5^+ [69] for the 1.5 s and 2.99 s states, respectively. Measurements of the β decay of the two states suggest that the 1^+ state is the ground state of the system [70]. In ^{102}Nb , spins of 1^+ and (4^+) have been suggested for the 4.3 s and 1.3 s isomeric states respectively, though the order of these states is the matter of some debate. In this thesis, the high-spin state is taken to be the ground state of the system as quoted in the Nuclear Data Sheets [71].

8.1 Setup

In order to avoid an electronic $J = 0 \rightarrow J = 1$ (286 nm) transition from the ground state, which would give only three hyperfine peaks (and therefore a spin assignment would not be possible), an optical pumping scheme was used to probe a $4d^3(4F)5s \ ^5F_1 \rightarrow 4d^3(4F)5p \ ^5F_1$ transition (291 nm). This scheme was first investigated as part of the first use of optical pumping inside an ion cooler [49]. Electrons are excited from a 5D_0 ground state in to a 3D_1 state (with 286 nm laser light) before subsequently relaxing. A schematic of this process can be found in Figure 8.1. During this relaxation process, the electron may de-excite in to a number of different high-lying energy levels above the 5F_1 state. Where this occurs, population of the 5F_1 state may still be achieved by the process of collisional de-excitation. Whilst inside the cooler, ions collide with the helium atoms in the buffer gas, decreasing the electronic energy to the lower 5F_1 state in a process known as ‘quenching’. Such schemes have been found to completely depopulate the ground

state, allowing for a maximum efficiency of spectroscopy. The measurement is also aided by the fact that the $J = 1 \rightarrow J = 1$ transition (with an Einstein A value of $1.201 \times 10^8 \text{ s}^{-1}$) is an order of magnitude stronger than the $J = 0 \rightarrow J = 1$ transition ($A = 1.630 \times 10^7 \text{ s}^{-1}$) [65]. The lower efficiency of the pumping line has little effect on the scheme since the interaction time in the cooler is significantly longer (100s of ms bunch accumulation time compared to a few μs as the bunch travels through the LCR) and a higher powered laser beam can be used without creating any negative effects such as power broadening and increased laser scatter counts. Again, the pumping light was provided by a pulsed Ti:Sa laser whilst the spectroscopic light was provided by a frequency-doubled Matisse 2 DS dye laser.

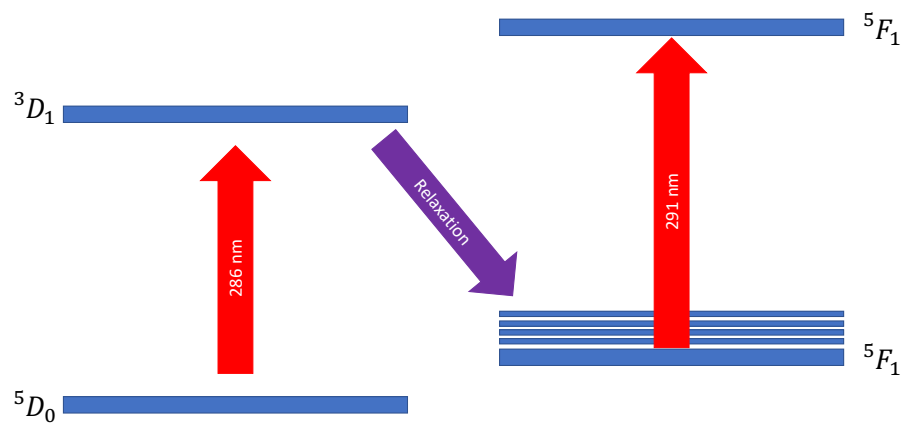


FIGURE 8.1: The chosen optical pumping scheme for niobium isotopes.

8.2 Preparatory Work

8.2.1 Revisiting the Previous Study of Niobium

In order to decrease the number of fitting parameters, and hopefully increase the quality of the fit, fixing the ratio of hyperfine parameters to known values is commonplace in those isotopic chains which demonstrate minimal hyperfine anomaly.

Such ratios also have use in determining the nuclear spin of a system unambiguously which, in turn, allows for the correct extraction of magnetic dipole and electric quadrupole moments of the nuclei as well as the change in mean-square charge radii.

Previous studies at the JYFL laboratory on niobium isotopes allow access to data for the stable isotope ^{93}Nb . Whilst these data have been fitted previously, a technique was used in which the intensities of the peaks are fixed to the so-called Racah intensities - the relative intensities of the peaks (compared to the most intense) as expected from angular momenta rules. This is especially useful when peaks are not well resolved within a spectrum and separate peak intensities are difficult to extract. When intensities of the peaks do not match those predicted perfectly, fitting spectra in this way can cause less accurate fits and so a technique wherein each peak is allowed its own free intensity is preferred. Since good precision will be necessary in the spin determination of $^{100,102}\text{Nb}$, the data were refitted allowing for free peak intensities.

A data set was fitted using a routine in which peaks were allowed to vary their intensities freely whilst sharing a FWHM. The ratios of the hyperfine parameters extracted from the fit are $A_l/A_u = -0.9610(1)$ and $B_l/B_u = +0.440(22)$. The specific fitted values can be found in Table 8.1 and the fit is shown in Figure 8.2.

TABLE 8.1: The measured hyperfine parameters in ^{93}Nb . The errors shown are derived from the statistical errors which are taken from the fitting process.

A_u (MHz)	A_l (MHz)	B_u (MHz)	B_l (MHz)
+1198.10(10)	-1151.42(10)	+52.96(82)	+23.28(82)

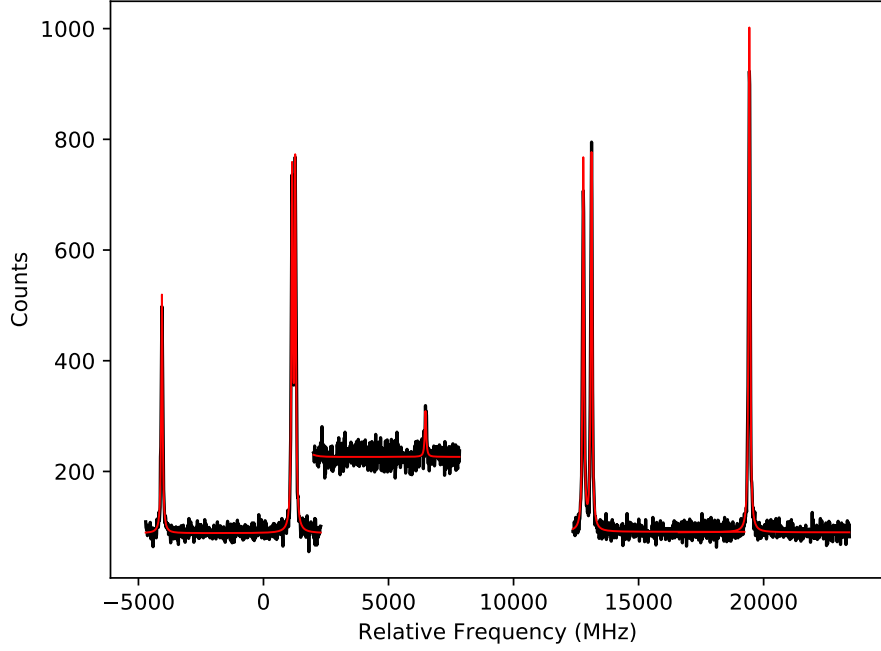


FIGURE 8.2: The previously measured spectrum of ^{93}Nb (black) with the new fit (red).

8.2.2 Empirical Estimates

Since the light provided by the dye laser is precise to the order of MHz [72] (compared the THz frequency of the light provided) and scanning over hyperfine structure takes place in 2 V steps (equivalent to roughly 30 MHz in the reference frame of the ion), it is important to create accurate estimates for the location of frequency peaks in order to make efficient use of the allocated beam time. Using an empirical estimate for the magnetic moment of odd-odd nuclei (Equation 8.1 and explained further in Section 2.2) and information from nearby isotopes, predictions of the magnetic moments of ^{100}Nb and ^{102}Nb were created in order to predict the hyperfine structure.

$$\mu(I) = \frac{I}{2} \left[\frac{\mu(I_\pi)}{I_\pi} + \frac{\mu(I_\nu)}{I_\nu} + \left(\frac{\mu(I_\pi)}{I_\pi} - \frac{\mu(I_\nu)}{I_\nu} \right) \frac{I_\pi(I_\pi + 1) - I_\nu(I_\nu + 1)}{I(I + 1)} \right]. \quad (8.1)$$

For example, such an estimate was performed for the ground and isomeric states in ^{100}Nb , which contains 41 protons and 59 neutrons. The effects of the 41st proton (excluding residual effects) can be seen in the neighbouring niobium isotopes where valence neutrons are fully paired and hence their contributions to the magnetic moment should be small. ^{99}Nb (41 protons, 58 neutrons) has been measured to have a magnetic moment of $+5.97 \mu_N$ and a spin of $I = 9/2$ [49]. Likewise, ^{99}Zr also contains 59 neutrons but a fully paired set of valence protons; the magnetic moment and spin of ^{99}Zr is $\mu = -0.93 \mu_N$ and $I = 1/2$ [62]. Using these values, a likely magnetic moment of ^{100}Nb is then $+5.04 \mu_N$ with a spin of $I = 5$, a spin in line with the suggested value [69].

For the predicted 1^+ state, the same $9/2$ proton orbital is used, coupled to a neutron $7/2$ orbital as measured in an excited state in ^{101}Zr [73] with a magnetic moment of $\mu = 0.6 \mu_N$. This gives the required spin and parity of $I = 1^+$ and a magnetic moment of $\mu = 3.35 \mu_N$.

A similar calculation can be made for ^{102}Nb , which is expected to share the properties of isotopes after the shape change. For ^{102}Nb , values for the unpaired proton are therefore taken from ^{101}Nb ($\mu = +3.19 \mu_N$, $I = 5/2$) [49]. The same unpaired neutron is present in ^{103}Mo with values $\mu = -0.27 \mu_N$ and $I = 3/2$ [60] and gives a likely spin and moment in ^{102}Nb of $\mu = +2.92 \mu_N$ and $I = 4$. For the same orbitals and a spin value of $I = 1$ for ^{102}Nb , a magnetic moment of $\mu = 2.37 \mu_N$ is predicted.

Since hyperfine splitting is dominated by the effects of the magnetic moment, it is assumed that the quadrupole moment will not cause any shifts large enough to be taken in to account in the estimation of the hyperfine structure, especially due to the likely deviations from these estimates.

8.3 Measurement and Analysis

Over the experimental campaign, a total of four new states were measured in niobium: a ground and isomeric state in both ^{100}Nb and ^{102}Nb . An example of the data taken in these measurements is shown in Figure 8.3. Alongside these measurements, scans of the $F = 7/2 \rightarrow 7/2$ peak of ^{101}Nb were also taken to act as a reference and calibrate the isotope shift. To begin, the peaks were measured individually whilst the search for the resonances was ongoing and then, once all peaks had been found and attributed to a spin state, the peaks of each state were re-measured as one set using the ‘tracks’ feature of the new DAQ.

Once measured, the spectra could then be fitted according to

$$\gamma = \zeta + \alpha_u A_u + \beta_u B_u - \alpha_l A_l - \beta_l B_l. \quad (8.2)$$

Here, $\zeta = \nu_{101} + \delta\nu^{101,A}$ where ν_{101} is the centroid of the hyperfine structure of ^{101}Nb and other symbols take the meanings as defined in Equation 3.12 .

For each of the newly measured states, the correct spin must be identified in order to achieve a reliable extraction of the atomic and nuclear properties. To confirm the spins of the states, an interim spin investigation was performed for each state before extraction of the final nuclear properties.

8.3.1 ^{100}Nb

As stated in Chapter 3, the ratio of hyperfine coefficients along an isotopic chain should remain constant if the hyperfine anomaly is negligible. Any large deviations from this ratio are indicative of an incorrect spin assignment and hence the nuclear spin of an isotope can be assigned if only one spin allows for a consistent

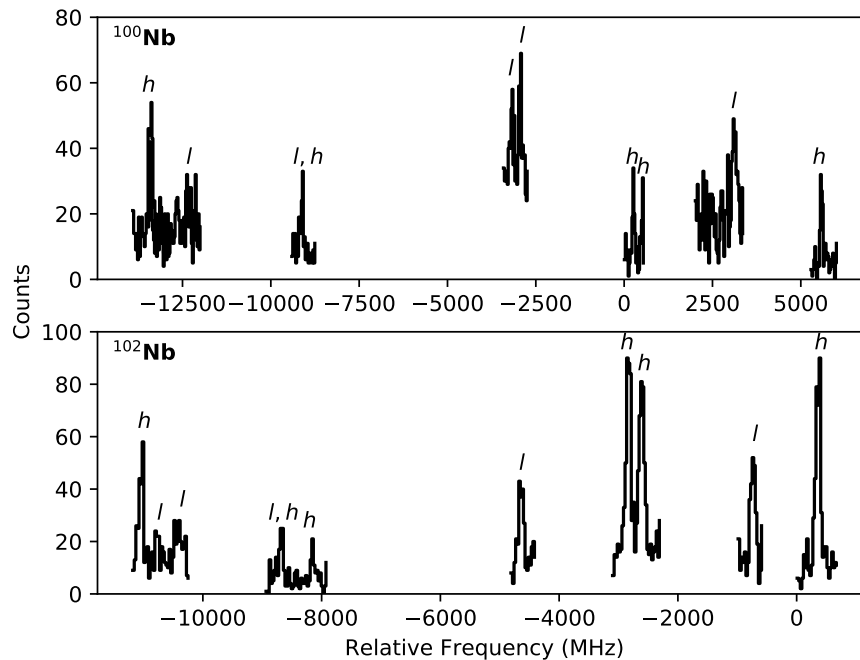


FIGURE 8.3: The measured data for $^{100,102}\text{Nb}$. Peaks identified with an l are from the low-spin state, with a h the high-spin state and the peak labelled with l, h contains a contribution from both states.

extraction of the hyperfine ratios.

To begin, the four resolved peaks which were measured individually for the low-spin state of ^{100}Nb (all peaks labelled with just an l in the top panel of Figure 8.3) were fitted according to a model where the ratios of the hyperfine parameters were fixed to $A_l/A_u = -0.9610$ and $B_l/B_u = +0.440$. This method was chosen over one where the parameters are all allowed to vary freely since one would need at least 5 peaks to fully define the system in this way. This fit was performed for $I = 1$ and $I = 2$ and, as can be seen in Figure 8.4, it was only possible to fit each peak in the low-spin state for $I = 1$ and hence the spin of the system is assigned as such.

In order to assign a nuclear spin to the high-spin state, all measured spectra of ^{100}Nb (including both states) were then fitted simultaneously. This fit was performed three times where the spin of the high-spin state was set to either

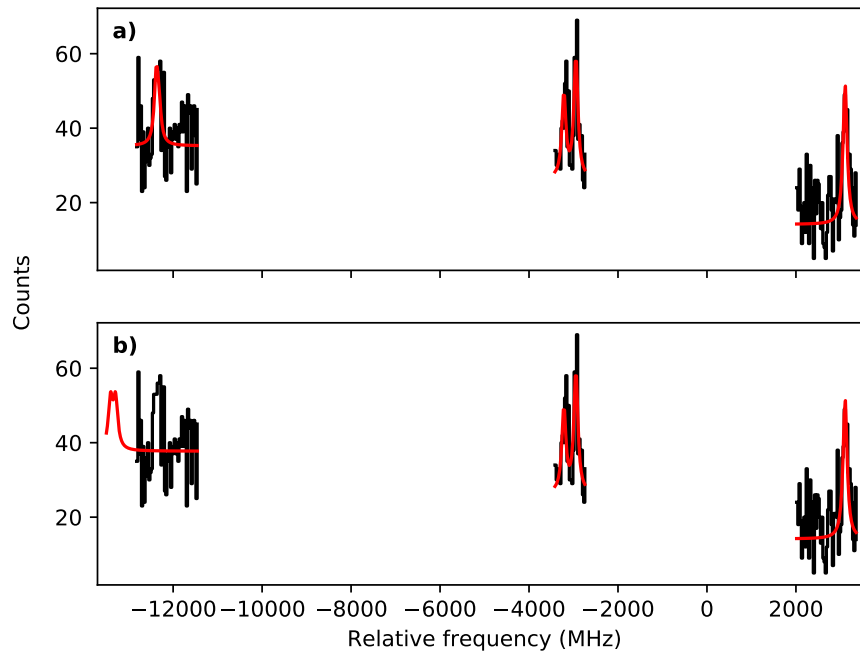


FIGURE 8.4: Assigning the spin of the low-spin state in ^{100}Nb . In Panel **a)**, the peaks are fit with a spectrum as generated with $I = 1$. Panel **b)** shows the same measured spectrum, only fit with $I = 2$. It is evident that all peaks cannot be fit simultaneously unless $I = 1$. Note that in Panel **b)**, the intensity of the left-most peak has been manually increased from the fitted value to demonstrate its position.

$I = 4, 5$ or 6 (one integer of spin either side of the suggested value) and, in all cases, its hyperfine parameters were left unconstrained. For the low-spin state, the spin was always kept at $I = 1$ and the ratios of the parameters fixed to $A_l/A_u = -0.9610$ and $B_l/B_u = +0.440$. Including all the data for the low-spin state in this fit allowed for a more confident description of the line shape of the unresolved peak since the low-spin peak location can be well defined. The ratios of the parameters of the high-spin state can be seen in Table 8.2. Whilst the closest match for the B_l/B_u ratio is given for $I = 5$, the large fitted errors on the B value meant that this method proved to be relatively unreliable.

As an alternative test of the nuclear spin, a run where all located high-spin peaks were measured at once, using the tracks feature of the DAQ, was fitted

TABLE 8.2: The measured hyperfine ratios for the high-spin state in ^{100}Nb , the errors shown are derived from the statistical errors from the fitting process. The known values are $A_l/A_u = -0.9610(1)$ and $B_l/B_u = +0.440(22)$.

I	A_l/A_u	B_l/B_u
4	-0.9659(13)	-2.70(54)
5	-0.9662(13)	+0.26(16)
6	-0.9663(13)	-0.408(75)

with the hyperfine ratios A_l/A_u and B_l/B_u fixed within the program to those extracted from ^{93}Nb in the preparatory studies of this work. A single peak with a free centroid parameter was added in to this model to account for the effect of the unresolved low-spin peak. When using this method, it was only possible to fit all hyperfine peaks simultaneously for $I = 5$, whilst the use of other spins would not allow for the correct relative spacing between peaks to occur when these ratios were forced (see Figure 8.5). It can therefore be confirmed that the spin state for the high-spin isomer of ^{100}Nb is $I = 5$. A discussion of one possibility for a residual discrepancy in the comparison of the B ratios is discussed later in Section 8.6.

Final Extraction of ^{100}Nb Hyperfine Parameters

With the spins of the two states confirmed, all ^{100}Nb spectra were fitted simultaneously using a χ^2 minimisation routine with the ratios of the hyperfine parameters of both states fixed to $A_l/A_u = -0.9610$ and $B_l/B_u = +0.440$. The results from these fits are presented in Table 8.3 and shown graphically in Figure 8.6.

TABLE 8.3: The measured hyperfine parameters for ^{100}Nb . The errors shown are derived from the statistical errors from the fitting process. The hyperfine parameters for the lower atomic state can be extracted from the fixed ratios of $A_l/A_u = -0.9610(1)$ and $B_l/B_u = +0.440(22)$.

Isotope	I	A_u (MHz)	B_u (MHz)	$\delta\nu^{101,A}$ (MHz)
^{100}Nb	1	+3153.6(50)	+12.1(56)	+1428(8)
^{100m}Nb	5	+881.95(41)	+44.0(51)	+1437(4)

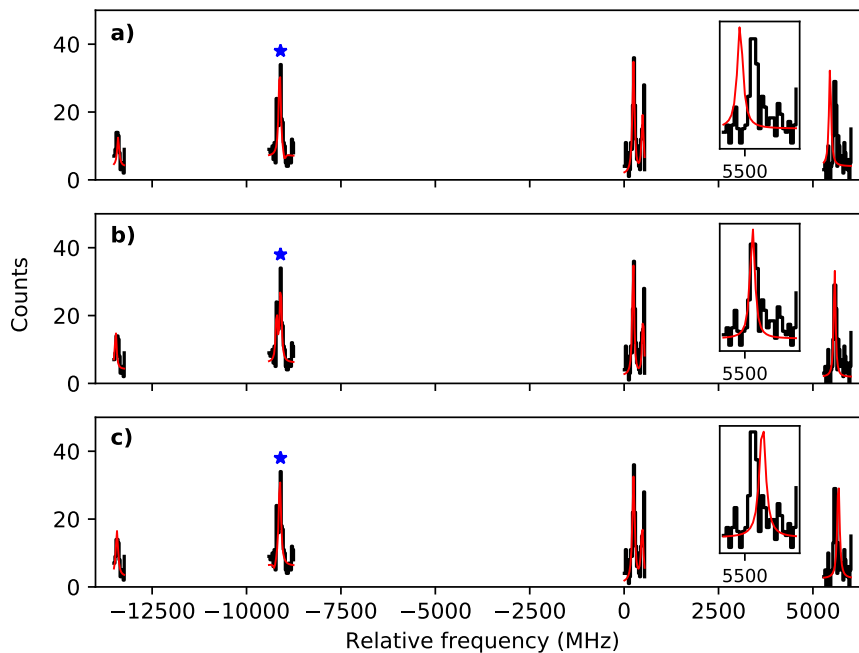


FIGURE 8.5: Assigning the spin of the high-spin state in ^{100}Nb where the peak indicated by a blue star contains a contribution from the low-spin state. In Panel **a)**, the peaks are fitted with a spectrum as generated with $I = 6$. Panel **b)** shows the same measured spectrum, only fitted with $I = 5$ and Panel **c)** with $I = 4$. It is evident that all peaks cannot be fit simultaneously unless $I = 5$. Note that in Panels **a)** and **c)**, the intensity of the right-most peak has been manually increased from the fitted value to demonstrate its position.

8.3.2 ^{102}Nb

As in ^{100}Nb , the low-spin state was fitted first to confirm its spin and extract interim values for the hyperfine parameters in order to define the location of the unresolved low-spin peak. This was possible since it can be seen from Figure 8.3 that four peaks in the low-spin state are fully isolated from the high-spin structure.

All of the files containing measurements of peaks in the low-spin isomer's hyperfine structure were fitted against a model in which the ratios of the A and B parameters were fixed and was performed for both $I = 1$ and $I = 2$. Again, it was not possible to carry out the previous tests of leaving all ratios free and comparing to known values in this case, since at least five peaks are needed to fit

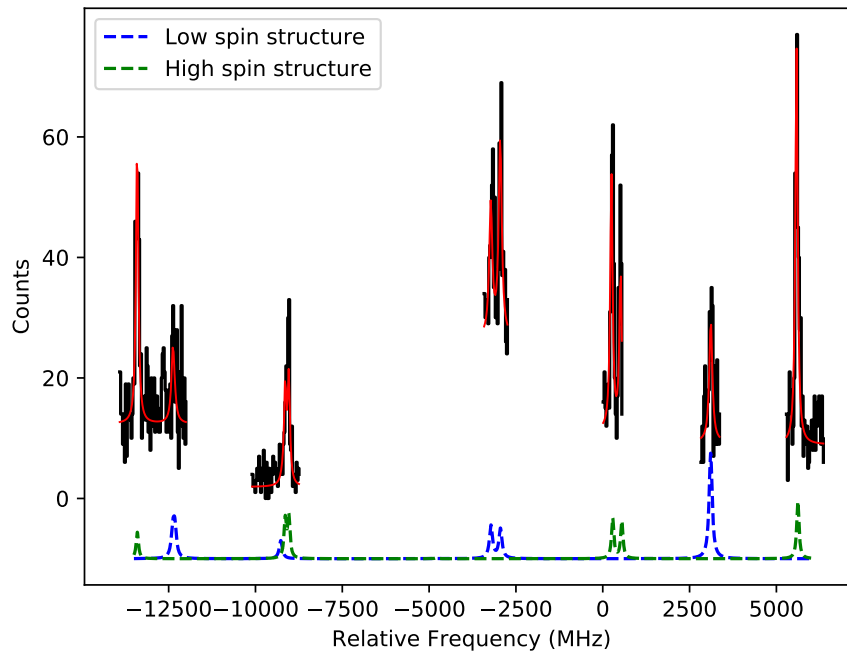


FIGURE 8.6: Examples of measured peaks of both states in ^{100}Nb and their fits. The example structures underneath are calculated from Racah intensities to show the locations of the peaks of each structure.

A_u , A_l , B_u , B_l and the centroid simultaneously with no extra constraints. As seen in Figure 8.7, it was once again seen that every peak not could be fitted simultaneously under constraint of both the A and B hyperfine parameter ratios for $I = 2$ and therefore $I = 1$ is assigned to this nuclear state.

With the spin of the low-spin state confirmed, it was then possible to perform an investigation in to the spin of the second state. To do this, a model was constructed and fitted simultaneously to all measured spectra of the high-spin state in

TABLE 8.4: The measured hyperfine ratios for the high-spin state in ^{102}Nb . The errors shown are derived from the statistical errors from the fitting process. The known values are $A_l/A_u = -0.9610(1)$ and $B_l/B_u = +0.440(22)$.

I	A_l/A_u	B_l/B_u
3	-0.9679(15)	+0.041(15)
4	-0.9633(15)	+0.349(21)
5	-0.9604(15)	+0.669(30)
6	-0.9585(15)	+1.003(43)

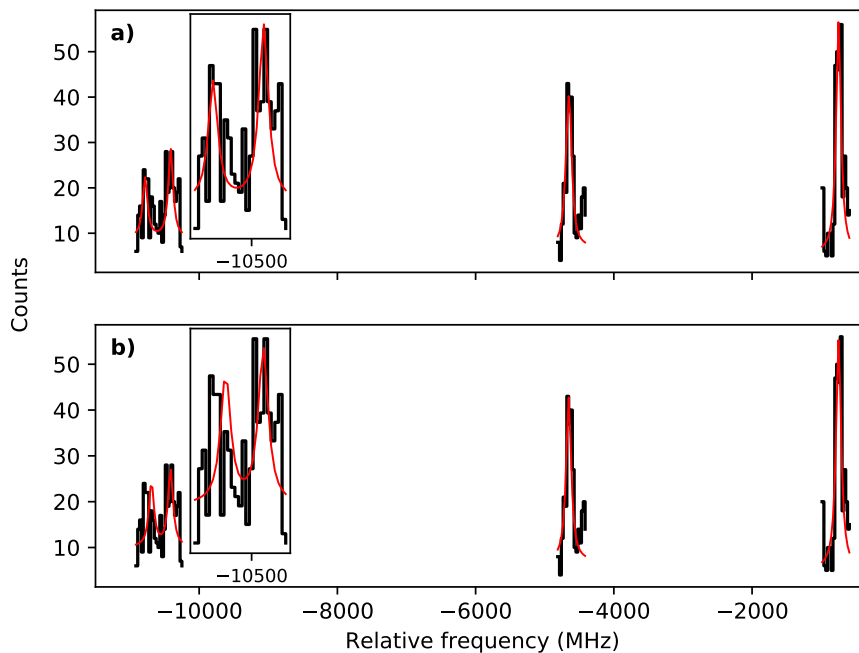


FIGURE 8.7: The measured spectrum of ^{102}Nb and the fitted spectra for $I = 1$ and $I = 2$. Panel **b)** shows the fit when $I = 2$, the inset shows the location of the leftmost peak has not been correctly fit. It is important to note that the intensity of this peak has been manually increased from the fitted value as a demonstration of its location.

^{102}Nb alongside the low-spin data (for the low-spin state the ratios of the hyperfine parameters were fixed whilst the hyperfine parameters of the upper state were left as free parameters). As before, by including the data of the low-spin state in this fit the location of the unresolved peak could be well defined. The fit was repeated for values of nuclear spin between $I = 3 - 6$ for the high-spin state whilst the spin of the low-spin state was kept constant at $I = 1$.

The ratios from these fits are presented in Table 8.4. It can be seen that no solid conclusions can be drawn from these ratios alone (again, a possible reason for this is discussed in Subsection 8.6) although $I = 4$ and $I = 5$ remain good candidates since no other spins give a B ratio in the region of that expected.

Towards the end of the beam time, a re-measurement of the located peaks was

taken of six resonant peaks from the high-spin state (including only one peak from the low-spin state, which was unavoidable due to its unresolved nature) in a single run in order to increase statistics and reduce uncertainties which may occur due to drifts in experimental conditions. This file was fitted against a model hyperfine structure of the high-spin state with spins $I = 4, 5$ and the ratios of the hyperfine parameters fixed to $A_l/A_u = -0.9610$ and $B_l/B_u = +0.440$. To account for the presence of the low-spin peak, the model was again improved by adding on a second spectrum containing only one peak with a free centroid to account for the presence of the low-spin peak.

With these constraints on the hyperfine ratios, it was not possible to fit all peaks simultaneously for $I = 5$ (as evidenced in Figure 8.8). It was, however, possible to achieve a good fit for $I = 4$ and hence the spin of the high-spin state in ^{102}Nb is confirmed as such.

Final Extraction of ^{102}Nb Hyperfine Parameters

With the spins of $^{102,102m}\text{Nb}$ confirmed, all data taken for both states in ^{102}Nb were fitted simultaneously with a model which contained contributions from both states in order to accurately describe the shape of the overlapping peaks. In this fit, the ratios of the hyperfine parameters in both the low- and high-spin states are fixed to $A_l/A_u = -0.9610$ and $B_l/B_u = +0.440$. The values from this fit may be found in Table 8.5 and shown graphically in Figure 8.9.

TABLE 8.5: The measured hyperfine parameters for ^{102}Nb . The errors shown are derived from the statistical errors from the fitting process. The hyperfine parameters for the lower atomic state can be extracted from the fixed ratios of $A_l/A_u = -0.9610(1)$ and $B_l/B_u = +0.440(22)$.

Isotope	I	A_u (MHz)	B_u (MHz)	$\delta\nu^{101,A}$ (MHz)
^{102}Nb	4	+644.77(40)	-265.8(35)	-158(3)
^{102m}Nb	1	+2008.1(17)	-55.4(23)	-179(6)

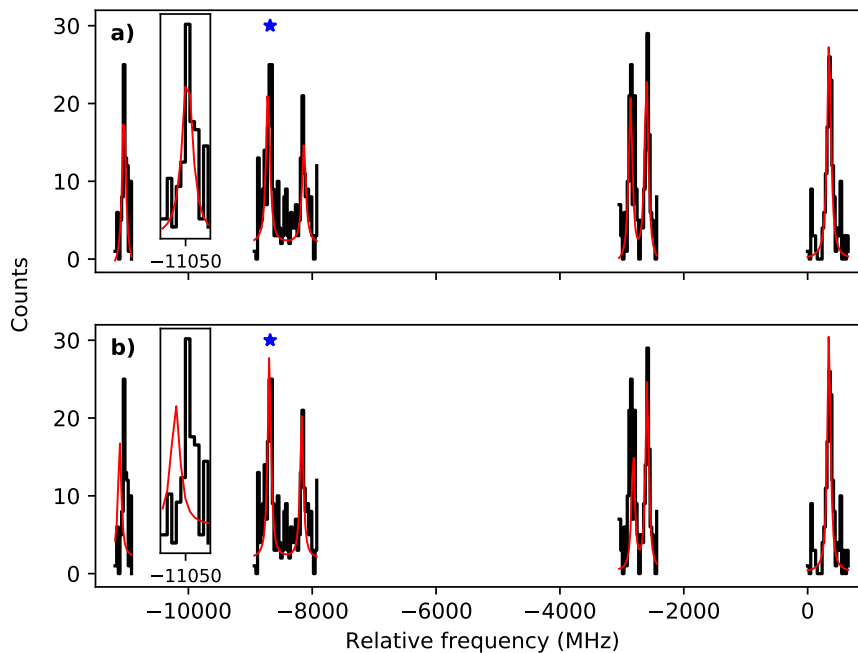


FIGURE 8.8: The measured spectrum of ^{102m}Nb and the fitted spectra for $I = 4$ (Panel **a**) and $I = 5$ (Panel **b**). It is important to note that the intensity of the leftmost red peak in Panel **b**) has been manually increased from the fitted value as a demonstration of its location, whereas intensities of the other peaks are taken from the fitting routine. The spectrum also includes one peak from the $I = 1$ state which overlaps in frequency which is signified by a blue star.

8.4 Nuclear Properties

As in Chapter 7, the nuclear electromagnetic moments were extracted from the ratios of the measured parameters and a reference isotope. In this case, the isotope ^{93}Nb was used for calibration since the hyperfine parameters and moments were previously known [49]. These values are $\mu_{93} = +6.1705(3) \mu_N$, $Q_{s,93} = -0.32(2) \text{ b}$, $A_{u,93} = +1197.5(2) \text{ MHz}$ and $B_{u,93} = +52.9(8) \text{ MHz}$. The extracted properties for $^{100,100m,102,102m}\text{Nb}$ may be found in Table 8.6.

As detailed in Chapter 7, the measured spectroscopic quadrupole moments and changes in mean-square charge radii can be used in tandem in order to measure the deformation of the nuclear system, allowing us to compare values across the

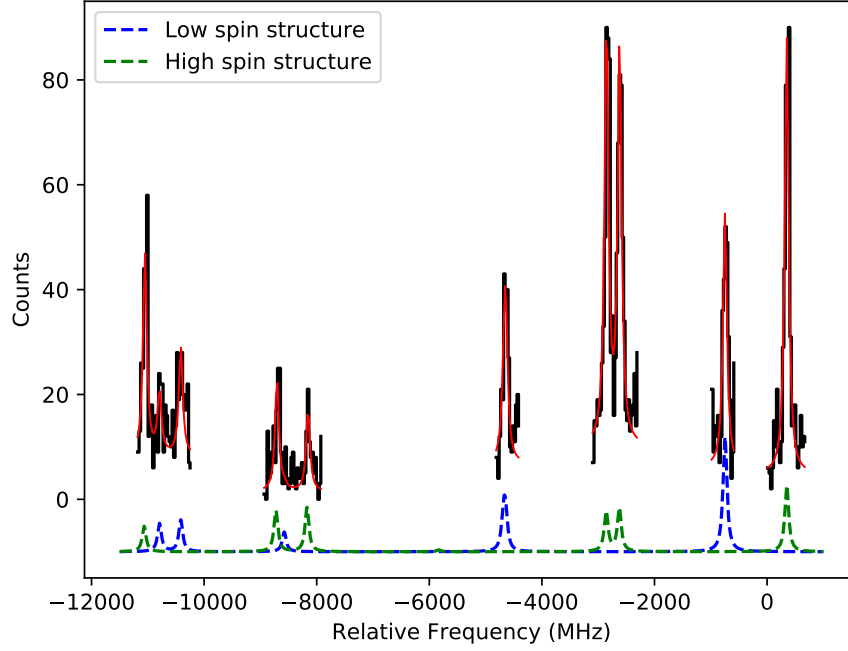


FIGURE 8.9: Examples of measured peaks of both states in ^{102}Nb and their fits. The example structures underneath are calculated from Racah intensities to show the locations of the peaks of each structure.

isotopic chain. The mean-square charge radii for niobium isotopes are easily extracted from the centroids of the hyperfine structures, as the atomic F and M factors have been previously established during the early work on the chain as $F = -2430 \text{ MHz} \cdot \text{fm}^{-2}$ and $M = +716 \text{ GHz} \cdot \text{amu}$ [49], and are shown in Table 8.6 and graphically in Figure 8.10.

TABLE 8.6: The nuclear moments for Nb extracted from the hyperfine parameters of its atomic states. The errors shown are derived from the statistical errors from the fitting process and the quoted error on the reference values of $\mu_{93} = +6.1705(3) \mu_N$, $Q_{s,93} = -0.32(2) \text{ b}$, $A_{u,93} = +1197.5(2) \text{ MHz}$ and $B_{u,93} = +52.9(8) \text{ MHz}$.

Isotope	I	$\mu (\mu_N)$	$Q_s (\text{b})$	$\delta \langle r^2 \rangle^{101,A} (\text{fm}^2)$
^{100}Nb	1	+3.611(6)	-0.07(3)	-0.610(7)
$^{100\text{m}}\text{Nb}$	5	+5.049(3)	-0.27(4)	-0.613(6)
^{102}Nb	4	+2.953(2)	+1.61(11)	+0.064(1)
$^{102\text{m}}\text{Nb}$	1	+2.299(2)	+0.34(3)	+0.073(2)

The magnetic moments extracted from the hyperfine spectra compare favourably to those from the empirical estimates, suggesting a pure configuration in all isotopic and isomeric states. For example, the $I = 5$ state in ^{100}Nb was suggested to be composed of a $s_{1/2}$ neutron as in the neighbouring ^{99}Zr nucleus [62] and a $g_{9/2}$ proton as in common with ^{99}Nb [49, 74]. A combination of these nucleons gave an estimated magnetic moment of $+5.04 \mu_N$ compared to the extracted value of $+5.049(3) \mu_N$. Indeed, even the extracted nuclear moment of ^{102m}Nb which differs the most from the empirical estimate (an estimate of $+2.368 \mu_N$ compared to a measured value of $+2.299 \mu_N$) still lies remarkably close agreement.

As in yttrium, the expected mean-square charge radius from static deformation effects can be calculated through the droplet model and compared to those measured from the experiment. Figure 8.10 demonstrates the differences between these two values. It is found that ^{100}Nb behaves much like its previously measured neighbour ^{99}Nb in that it shows a large degree of dynamic oblate deformation comparable to that seen in the yttrium chain (with the low- and high-spin states having a value of $Q_0 = -0.73(35)$ b and $Q_0 = -0.46(6)$ b, respectively) but demonstrates no sign of shape coexistence between the ground and isomeric states of the nucleus which is perhaps surprising due to the isotonic relationship between ^{100}Nb and ^{98}Y . Unlike the Y chain which demonstrates a rapid change to a rigidly deformed prolate system, the Nb chain demonstrates a similar rapid change in shape, moving to Q_0 values of $+3.35(25)$ b and $+3.16(21)$ b for the low- and high-spin states respectively, but retains its considerable softness afterwards (as shown in Figure 8.10).

8.5 Systematics of the $Z = 40$ Region

Figure 8.11 shows the measured mean-square charge radii for seven isotopic chains in the $Z = 40$ region: krypton, rubidium, strontium, yttrium, zirconium, niobium

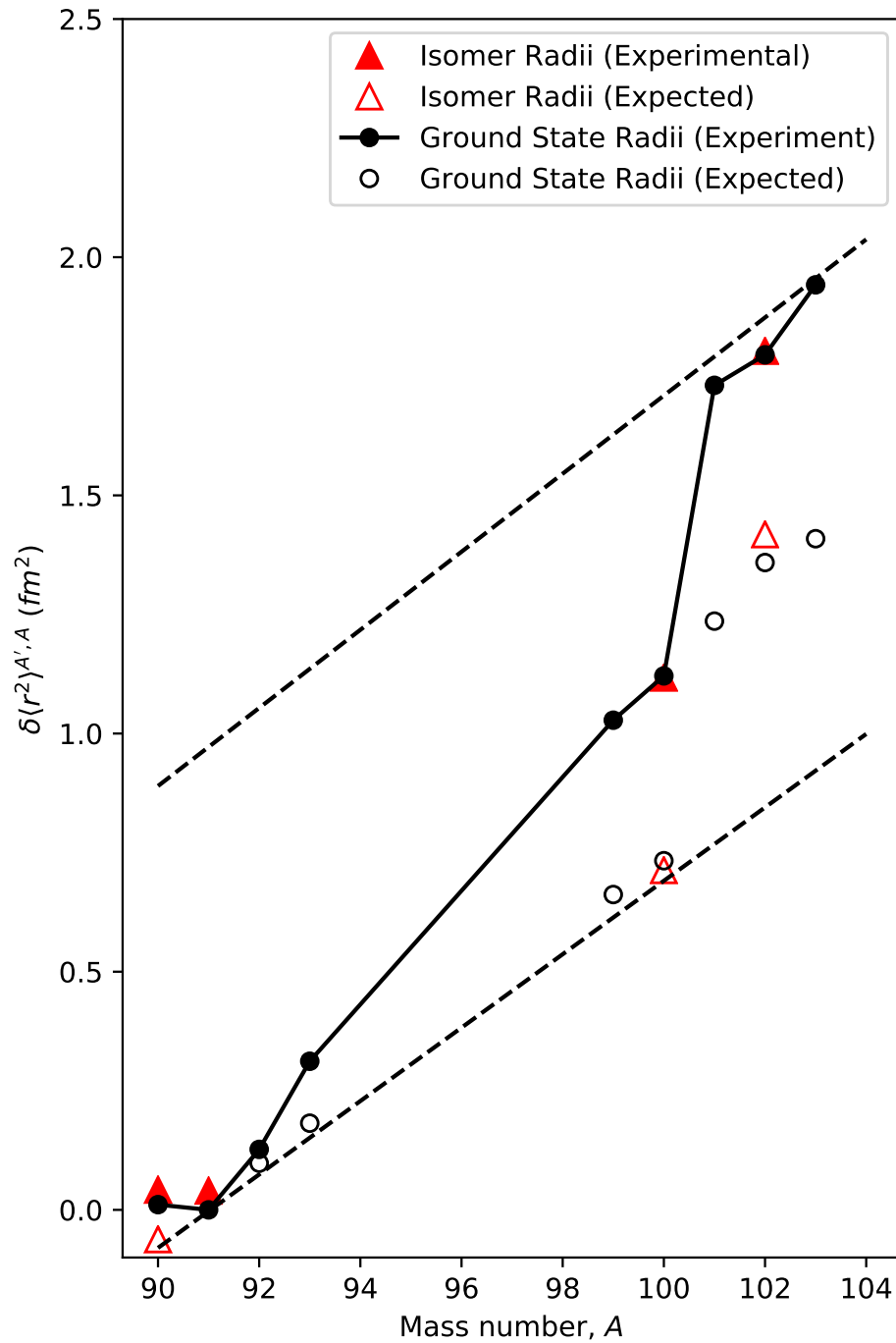


FIGURE 8.10: The measured charge radii of the Nb isotopes compared to the values expected from the liquid drop model assuming static deformation only. The lower and upper dashed black lines represent the isodeformation lines for $\beta_2 = 0$ and $\beta_2 = 0.4$ respectively. Values for $^{99,101,103}\text{Nb}$ are taken from [49].

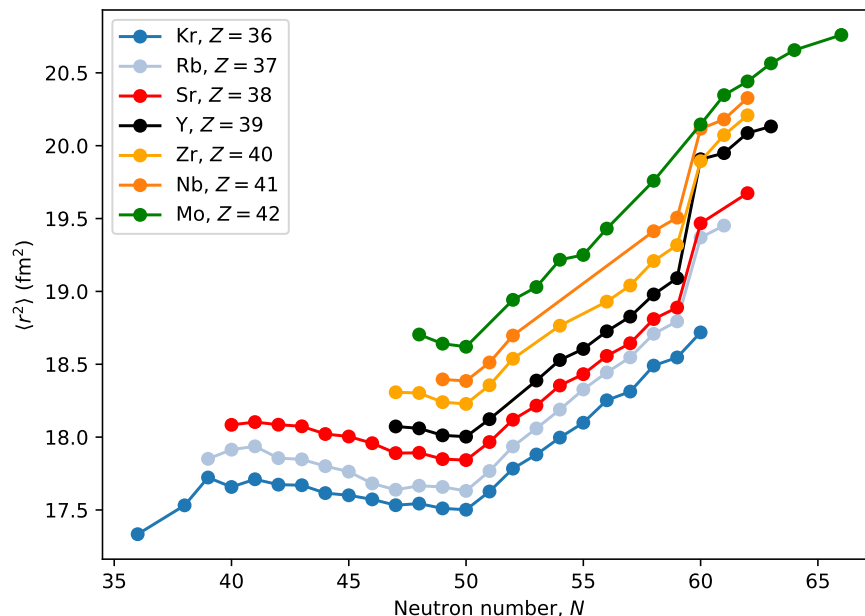


FIGURE 8.11: The measured charge radii of isotopic chains in the $Z = 40$ region. Data for changes in charge radii are taken from Refs. [8, 49, 60, 62, 76–78] and absolute charge radii are taken from Ref. [79]

and molybdenum ($Z = 36 - 42$). It is clear that each chain between $Z = 37$ and $Z = 41$ demonstrates a shape change at $N = 60$ due to the large jump in the value of the charge radius. Whilst the effect is strong in all of these chains, it is at its largest in the yttrium chain. The newly measured charge radii of $^{100,102}\text{Nb}$ fit the trends in this chain well with ^{100}Nb lying just before the shape change as expected from the other $N = 59$ nuclei. Although the known Nb radii follow the trends of the region, relatively few radii in this chain have been measured in the region between the $N = 50$ shell closure and $N = 60$ compared to its neighbouring chains. The large change in deformation appears to ‘wash out’ in the $Z = 42$ molybdenum chain, where an onset of triaxiality has been suggested to occur [75].

8.6 Conclusions

This chapter presents the first measurements of ^{100}Nb , ^{100m}Nb , ^{102}Nb and ^{102m}Nb and, alongside previous measurements in the chain, helps to build a picture of

the nuclear landscape in this region. When fitting the hyperfine structure measurements from these states, the extracted ratios of the hyperfine parameters did not agree well with those from the stable ^{93}Nb studies taken before. It is possible that this is due to experimental drifts which have not been accounted for between the measurements of each of the scan regions in ^{93}Nb , which was only measured once. A remeasurement of this structure with the new ‘track’ functionality in the recently installed data acquisition system at IGISOL-IV could help to remedy this situation. Regardless, in each of the states it was possible to determine the nuclear spin (through constraint of the ratios of the hyperfine parameters) and it was also possible to extract magnetic dipole and electric quadrupole moments.

The magnetic dipole moments compare favourably with the empirical estimates of the dipole moments of neighbouring isotopes while the quadrupole moments (together with complementary measurements of the isotope shift) show no sign of shape coexistence in either ^{100}Nb or ^{102}Nb , unlike the one clearly present in ^{98}Y . The chain also differs with respect to yttrium in that the dynamic nature of the deformation does not disappear with the shape change but the difference between the measured mean-square charge radii and those from the liquid droplet model remain large.

Many mean-square charge radii of niobium are yet to be measured in the $N = 50 - 60$ region. These measurements would perhaps be interesting to confirm that the niobium chain indeed follows the same gentle increase in deformation as the rest of the region.

Chapter 9

Summary and Future Work

9.1 Conclusion

This thesis has presented the first measurement of the low-lying isomeric state in ^{98}Y on the $^3D_2 \rightarrow ^3P_1$ atomic transition. Not only has the work allowed for an unambiguous spin assignment for this state of $I = 7$ but also for a correct calculation of the nuclear electromagnetic moments owing to a peak misidentification in the previous analysis. Further to these assignments, this work also details the remeasurement of ^{99}Y for the purposes of recalibrating the ratios of the hyperfine parameters on the $^3D_2 \rightarrow ^3P_1$ transition and a newly performed King plot, yielding values of the atomic F and M factors of the transition as $F_{321} = -1404(25) \text{ MHz} \cdot \text{fm}^{-2}$ and $M_{321} = +112(18) \text{ GHz} \cdot \text{amu}$. The newly confirmed spin and moments then allowed for a re-analysis of the previous 363 nm data and subsequent extraction of the properties of the shape coexistence present in the system. Previously, it was thought that the isomer demonstrated a highly dynamic deformation due to a large difference in the measured value of the mean-square charge radius and the radius predicted by a deformed droplet model under the assumption of static deformation alone. These new measurements show that the deformation is, in fact, much more static than previously believed and much

more in line with the type of deformation present after the shape change at $N = 60$.

Furthermore, a total of four niobium states were successfully measured with laser spectroscopy for the first time: $^{100,100m}\text{Nb}$ and $^{102,102m}\text{Nb}$. For each of these states, a nuclear spin could be successfully assigned to the state and the magnetic dipole and electric quadrupole moments extracted. Complementary measurements of the change in mean-square charge radius were also taken from the spectra which help to continue to build up a picture of the deformation present in the region. Similar to the yttrium chain, the $Z = 41$ Nb isotopes demonstrate a large onset of deformation at $N = 60$ but the transition differs in that the high dynamic component of the deformation remains present after the shape change. Moreover, no shape coexistence between the ground states and low-lying isomeric states measured in this work appears to be present.

In the case of Y, this work was compared to state-of-the-art theoretical calculations in an Energy Density Functional framework. Specifically, calculations were performed using the UNEDF0 and UNEDF2 Skyrme-like functionals as well as the recently developed $F(\Delta r, \text{HFB})$ Fayans functional. This comparison showed that the $F(\Delta r, \text{HFB})$ functional fails to reproduce the large onset of deformation observed in the charge radii of the Y isotopes, whilst the UNEDF0 and UNEDF2 calculations demonstrate a shape change at $N \approx 60$. These latter functionals, however, fail to accurately reproduce the upwards kink observed at $N = 50$, a phenomenon well described by the Fayans functional.

9.2 Outlook

In a campaign by the JYFLTRAP group, which performs high-precision mass measurements at the IGISOL facility, the masses of many neutron-rich yttrium

isotopes were measured [80]. In particular, measurements of ^{100}Y demonstrated the possibility of the presence of two states inside the trap: a ground state and an isomer. However, a laser spectroscopy experiment in the same lab saw no signs of a second state during their investigation. One possible explanation for this observation would be a very different state of the isomer to the ground state, as in ^{98}Y . This shape change would result in a large isomer shift and therefore a large difference in the centroids of the structure, potentially shifting the hyperfine structure of this second state outside of the scanning range of the previous study. Furthermore, a re-analysis of the ^{100}Y data with the newly calibrated F and M factors could confirm the current spin assignment of $I = 4$.

As seen in Figure 7.16, another region of high deformation is expected in the Y chain around $N \approx 40$. Indeed, this high level of deformation has already been observed in the neighbouring strontium chain [77] one proton lower, and in the rubidium chain [78] below that. Tests of production rates using the heavy-ion guide at the IGISOL facility has show that, using fusion evaporation reactions, isotopes as neutron deficient ^{82}Y could be successfully created at high rates [45]. The possibility of using laser spectroscopy to probe these states is therefore promising and would be an ideal methodology to investigate this region of high deformation around $N, Z \approx 40$.

It can be seen in Figure 8.10 that a large portion of the niobium isotopes between the shell closure at $N = 50$ and the shape change at $N = 60$ have not yet been measured by laser spectroscopy. Since the niobium chain appears to share some similarity to the behaviour of the nearby yttrium isotopes, it would be interesting to probe this region and compare the behaviour of the two chains, especially as the shape change in niobium does not appear to share the same properties yttrium due to maintaining its large degree of softness after the shape transition. It would also be interesting to extend measurements of the charge radius of niobium

past $A = 103$ to see if the high degree of β -softness continues to be present or if the chain begins to behave more like the rigid yttrium isotopes in the same $A \approx 100$ region. Furthermore, a remeasurement of the stable isotope ^{93}Nb would allow for a better calibration of the ratios of the hyperfine parameters and provide improved confidence in the spin assignments in this work.

The sudden onset of deformation has been shown to not occur in the molybdenum chain ($Z = 42$), indicating that this appears to be the upper limit for this phenomenon. Recently, a proposal has been accepted by the JYFL PAC [81] to study $^{90-113}\text{Tc}$, crossing this $N = 60$ critical point. These studies hope to demonstrate the nature of these effects in odd Z nuclei.

Appendix A

Potential Energy Surfaces From EDFs

This appendix shows the potential energy surfaces for many isotopes of Sr ($Z = 38$) and Zr ($Z = 40$) as calculated from Density Functional Theory using three functionals: UNEDF0, UNEDF2 and F(Δr ,HFB). All figures in this appendix are courtesy of Markus Kortelainen [66].

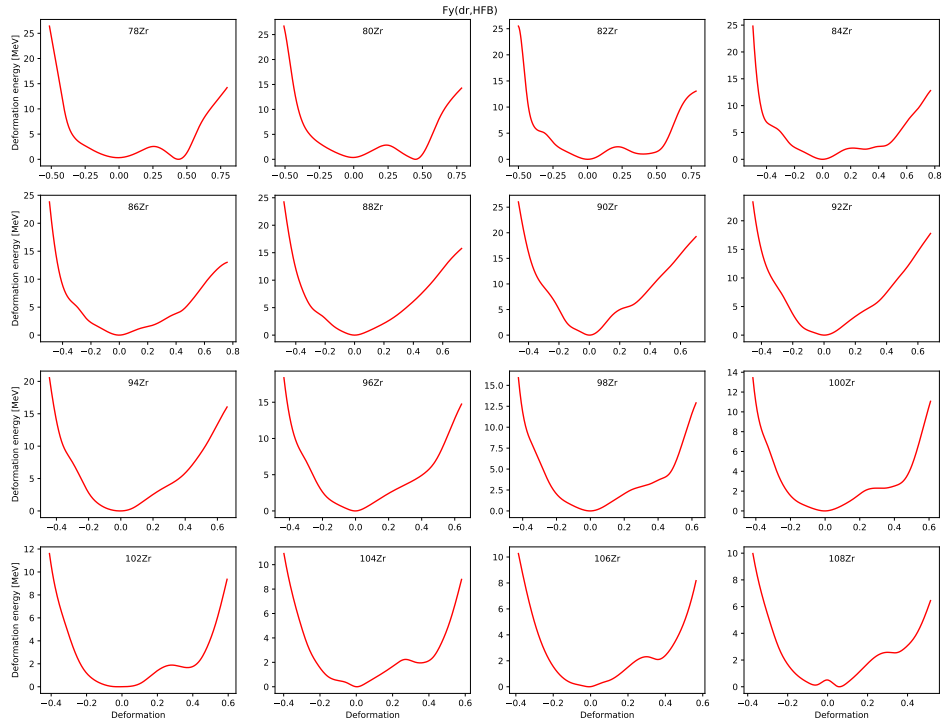


FIGURE A.1: The potential energy surface with respect to the deformation parameter β_2 for $^{78-108}\text{Zr}$ as calculated by the $\text{Fy}(\Delta r, \text{HFB})$ functional.

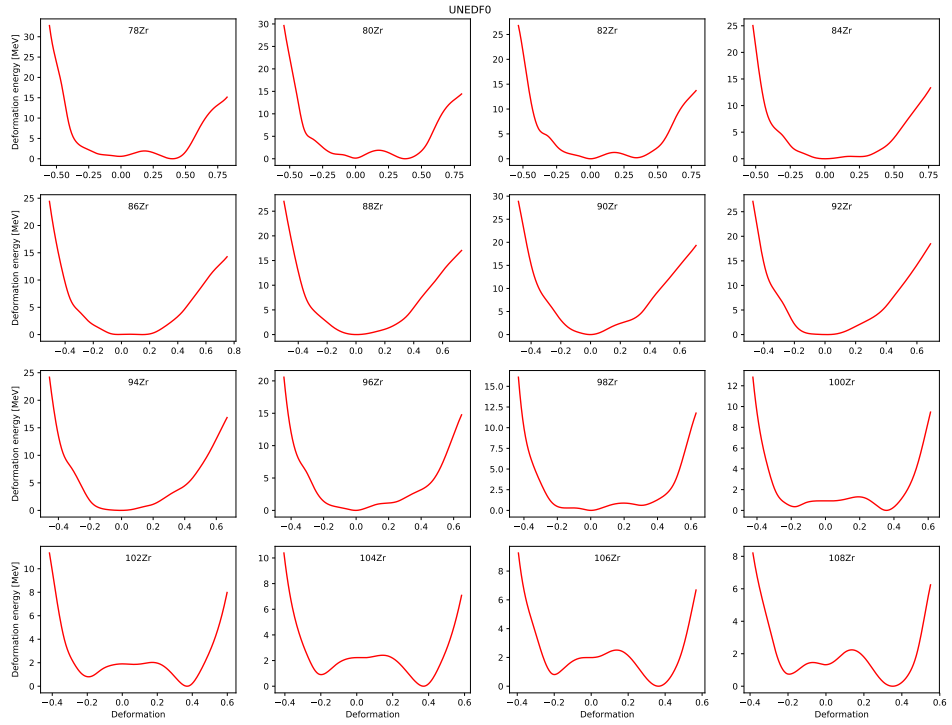


FIGURE A.2: The potential energy surface with respect to the deformation parameter β_2 for $^{78-108}\text{Zr}$ as calculated by the UNEDF0 functional.

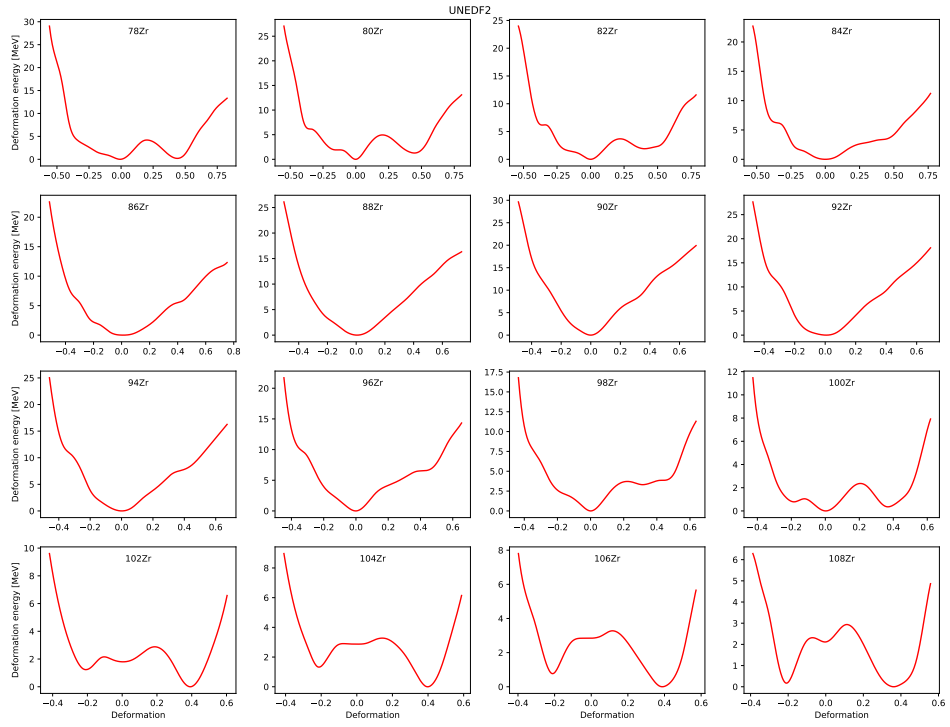


FIGURE A.3: The potential energy surface with respect to the deformation parameter β_2 for $^{78-108}\text{Zr}$ as calculated by the UNEDF2 functional.

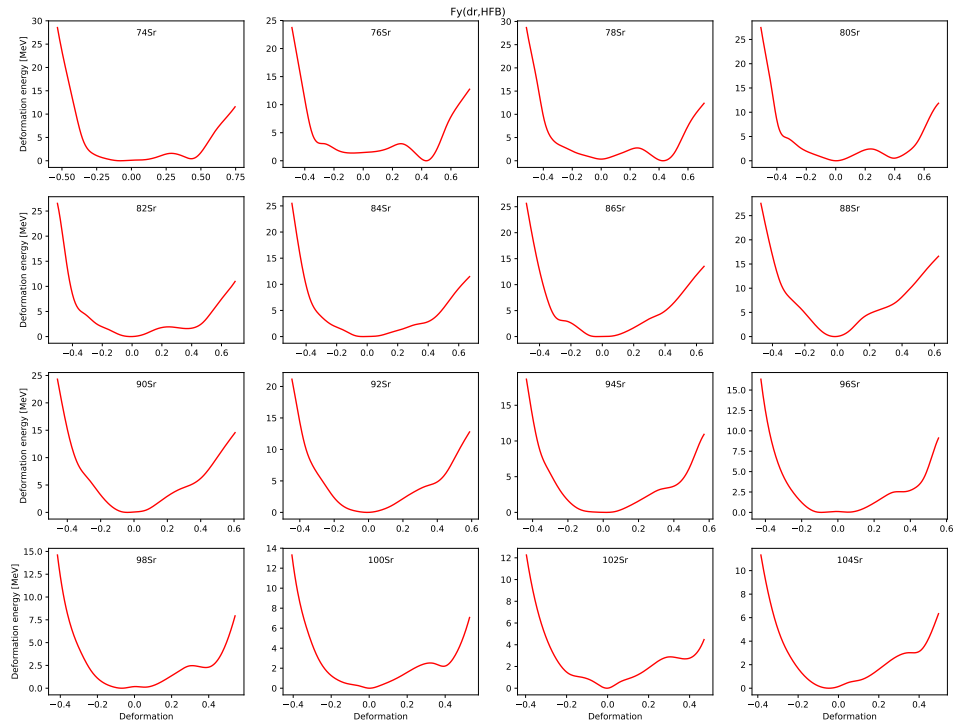


FIGURE A.4: The potential energy surface with respect to the deformation parameter β_2 for $^{74-104}\text{Sr}$ as calculated by the Fy(Δr ,HFB) functional.

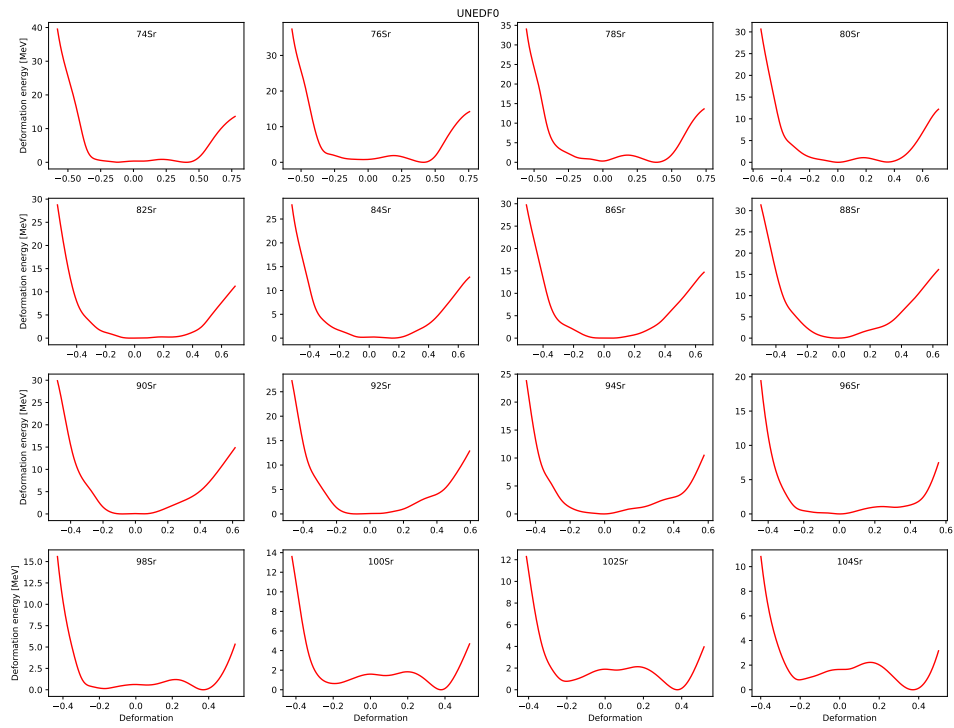


FIGURE A.5: The potential energy surface with respect to the deformation parameter β_2 for $^{74-104}\text{Sr}$ as calculated by the UNEDF0 functional.

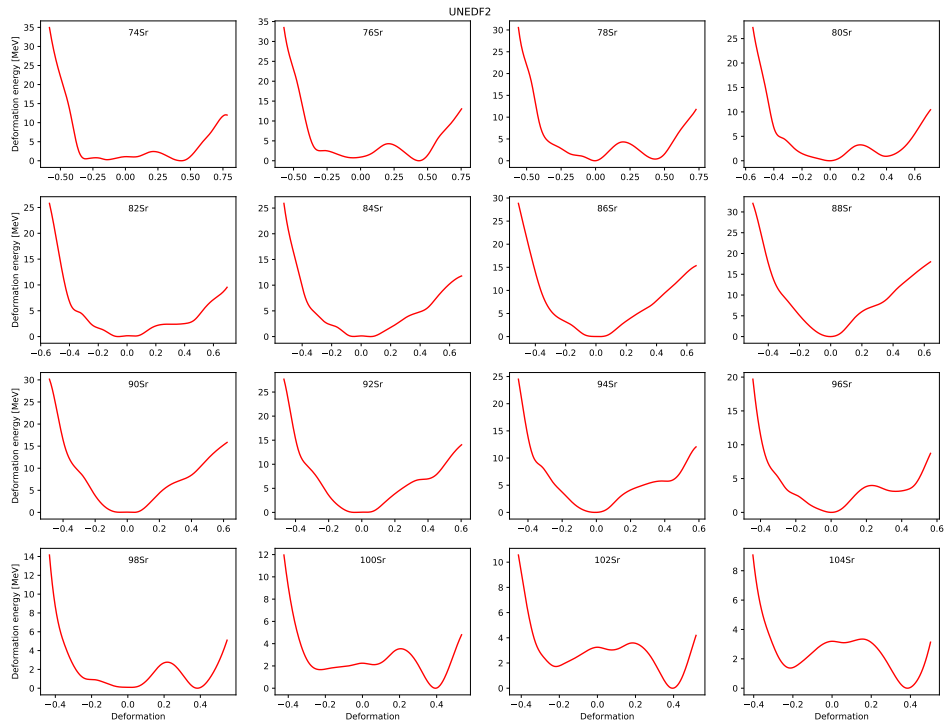


FIGURE A.6: The potential energy surface with respect to the deformation parameter β_2 for $^{74-104}\text{Sr}$ as calculated by the UNEDF2 functional.

References

- [1] K. S. Krane. *Introductory Nuclear Physics*. Wiley, New York, NY, 1988. URL <https://cds.cern.ch/record/359790>.
- [2] B. Cheal and K. T. Flanagan. Progress in laser spectroscopy at radioactive ion beam facilities. *Journal of Physics G: Nuclear and Particle Physics*, 37(11):113101, sep 2010. doi: 10.1088/0954-3899/37/11/113101. URL <https://doi.org/10.1088/0954-3899/37/11/113101>.
- [3] F.G. Kondev, M. Wang, W.J. Huang, S. Naimi, and G. Audi. The NUBASE2020 evaluation of nuclear physics properties. *Chinese Physics C*, 45(3):030001, mar 2021. doi: 10.1088/1674-1137/abddae. URL <https://doi.org/10.1088/1674-1137/abddae>.
- [4] The Colourful Nuclide Chart. URL <https://people.physics.anu.edu.au/~ecs103/chart/>.
- [5] J. Al-Khalili. *Halo Nuclei*. 2053-2571. Morgan & Claypool Publishers, 2017. ISBN 978-1-6817-4581-7. doi: 10.1088/978-1-6817-4581-7. URL <http://dx.doi.org/10.1088/978-1-6817-4581-7>.
- [6] R. D. Page, P. J. Woods, R. A. Cunningham, T. Davinson, N. J. Davis, S. Hofmann, A. N. James, K. Livingston, P. J. Sellin, and A. C. Shotter. Discovery of new proton emitters ^{160}Re and ^{156}Ta . *Phys. Rev. Lett.*, 68:1287–1290, Mar 1992. doi: 10.1103/PhysRevLett.68.1287. URL <https://link.aps.org/doi/10.1103/PhysRevLett.68.1287>.

-
- [7] Z. Ren and H. Toki. Superdeformation in the newly discovered super-heavy elements. *Nuclear Physics A*, 689(3):691–706, 2001. ISSN 0375-9474. doi: [https://doi.org/10.1016/S0375-9474\(00\)00689-8](https://doi.org/10.1016/S0375-9474(00)00689-8). URL <https://www.sciencedirect.com/science/article/pii/S0375947400006898>.
- [8] B. Cheal et al. The shape transition in the neutron-rich yttrium isotopes and isomers. *Physics Letters B*, 645(2):133 – 137, 2007. ISSN 0370-2693. doi: <https://doi.org/10.1016/j.physletb.2006.12.053>. URL <http://www.sciencedirect.com/science/article/pii/S037026930601608X>.
- [9] E. Rutherford. *Philosophical Magazine*, 90(sup1):31–37, 1919.
- [10] J. Chadwick. *Nature*, 129(3252):312–312, 1932.
- [11] G. Gamow. Mass defect curve and nuclear constitution. *Proceedings of the Royal Society of London. Series A, Containing Papers of a Mathematical and Physical Character*, 126(803):632–644, March 1930. doi: 10.1098/rspa.1930.0032. URL <https://doi.org/10.1098/rspa.1930.0032>.
- [12] M. G. Mayer. On closed shells in nuclei. *Phys. Rev.*, 74:235–239, Aug 1948. doi: 10.1103/PhysRev.74.235. URL <https://link.aps.org/doi/10.1103/PhysRev.74.235>.
- [13] C. Wraith. *The Evolution of Nuclear Structure in Odd-A Zinc Isotopes*. PhD thesis, 2018. URL <https://livrepository.liverpool.ac.uk/id/eprint/3029031>.
- [14] G. Neyens. Nuclear magnetic and quadrupole moments for nuclear structure research on exotic nuclei. *Reports on Progress in Physics*, 66(4):633–689, Mar 2003. doi: 10.1088/0034-4885/66/4/205. URL <https://doi.org/10.1088/0034-4885/66/4/205>.
- [15] B. Cheal, T. E. Cocolios, and S. Fritzsche. Laser spectroscopy of radioactive isotopes: Role and limitations of accurate isotope-shift calculations. *Phys.*

-
- Rev. A*, 86:042501, Oct 2012. doi: 10.1103/PhysRevA.86.042501. URL <https://link.aps.org/doi/10.1103/PhysRevA.86.042501>.
- [16] S. Thummerer, W. von Oertzen, B. Gebauer, S. M. Lenzi, A. Gadea, D. R. Napoli, C. Beck, and M. Rousseau. The population of deformed bands in ^{48}Cr by emission of ^8Be from the $^{32}\text{S} + ^{24}\text{Mg}$ reaction. *Journal of Physics G: Nuclear and Particle Physics*, 27(7):1405–1420, jun 2001. doi: 10.1088/0954-3899/27/7/303. URL <https://doi.org/10.1088/0954-3899/27/7/303>.
- [17] M. A. Alwaleedi. *Band structures of ^{131}Ce* . PhD thesis, 2013. URL https://livrepository.liverpool.ac.uk/15073/4/AlwaleediMoh_Dec2013_15073.pdf.
- [18] K. Heyde and J. L. Wood. Shape coexistence in atomic nuclei. *Rev. Mod. Phys.*, 83:1467–1521, Nov 2011. doi: 10.1103/RevModPhys.83.1467. URL <https://link.aps.org/doi/10.1103/RevModPhys.83.1467>.
- [19] M. Taylor et al. A triplet of differently shaped spin-zero states in the atomic nucleus ^{186}Pb . *Nature: international weekly journal of science*, 405:430–433, May 2000. ISSN 0028-0836.
- [20] T. Otsuka, A. Gade, O. Sorlin, T. Suzuki, and Y. Utsuno. Evolution of shell structure in exotic nuclei. *Rev. Mod. Phys.*, 92:015002, Mar 2020. doi: 10.1103/RevModPhys.92.015002. URL <https://link.aps.org/doi/10.1103/RevModPhys.92.015002>.
- [21] H. Heylen et al. High-resolution laser spectroscopy of $^{27-32}\text{Al}$. *Phys. Rev. C*, 103:014318, Jan 2021. doi: 10.1103/PhysRevC.103.014318. URL <https://link.aps.org/doi/10.1103/PhysRevC.103.014318>.

-
- [22] K. Hebeler. Ab initio frameworks in nuclear physics: from basic concepts to current developments. Lecture notes, 19th STFC Nuclear Physics Summer School, 2017.
- [23] G. Colò. Density Functional Theory (DFT) for atomic nuclei: a simple introduction, 2018.
- [24] M. Kortelainen et al. Nuclear energy density optimization: Shell structure. *Phys. Rev. C*, 89:054314, May 2014. doi: 10.1103/PhysRevC.89.054314. URL <https://link.aps.org/doi/10.1103/PhysRevC.89.054314>.
- [25] N. Schunck, editor. *Energy Density Functional Methods for Atomic Nuclei*. 2053-2563. IOP Publishing, 2019. ISBN 978-0-7503-1422-0. doi: 10.1088/2053-2563/aae0ed. URL <http://dx.doi.org/10.1088/2053-2563/aae0ed>.
- [26] M. Kortelainen, T. Lesinski, J. Moré, W. Nazarewicz, J. Sarich, N. Schunck, M. V. Stoitsov, and S. Wild. Nuclear energy density optimization. *Phys. Rev. C*, 82:024313, Aug 2010. doi: 10.1103/PhysRevC.82.024313. URL <https://link.aps.org/doi/10.1103/PhysRevC.82.024313>.
- [27] M. Bender, P.-H. Heenen, and P.-G. Reinhard. Self-consistent mean-field models for nuclear structure. *Rev. Mod. Phys.*, 75:121–180, Jan 2003. doi: 10.1103/RevModPhys.75.121. URL <https://link.aps.org/doi/10.1103/RevModPhys.75.121>.
- [28] M. Kortelainen et al. Nuclear energy density optimization: Large deformations. *Phys. Rev. C*, 85:024304, Feb 2012. doi: 10.1103/PhysRevC.85.024304. URL <https://link.aps.org/doi/10.1103/PhysRevC.85.024304>.
- [29] S. A. Fayans. Towards a universal nuclear density functional. *Journal of Experimental and Theoretical Physics Letters*, 68(3):169–174, 1998. doi: 10.1134/1.567841. URL <https://doi.org/10.1134/1.567841>.

-
- [30] P.-G. Reinhard and W. Nazarewicz. Toward a global description of nuclear charge radii: Exploring the Fayans energy density functional. *Phys. Rev. C*, 95:064328, Jun 2017. doi: 10.1103/PhysRevC.95.064328. URL <https://link.aps.org/doi/10.1103/PhysRevC.95.064328>.
- [31] A. J. Miller, K. Minamisono, A. Klose, D. Garand, C. Kujawa, J. D. Lantti, Y. Liu, B. Maaß, P. F. Mantica, W. Nazarewicz, W. Nörtershäuser, S. V. Pineda, P. G. Reinhard, D. M. Rossi, F. Sommer, C. Sumithrarachchi, A. Teigelhöfer, and J. Watkins. Proton superfluidity and charge radii in proton-rich calcium isotopes. *Nature Physics*, 15(5):432–436, 2019. doi: 10.1038/s41567-019-0416-9. URL <https://doi.org/10.1038/s41567-019-0416-9>.
- [32] P. Campbell, I.D. Moore, and M.R. Pearson. Laser spectroscopy for nuclear structure physics. *Progress in Particle and Nuclear Physics*, 86:127–180, 2016. ISSN 0146-6410. doi: <https://doi.org/10.1016/j.pnpnp.2015.09.003>. URL <https://www.sciencedirect.com/science/article/pii/S0146641015000915>.
- [33] T.J. Mertzimekis, K. Stamou, and A. Psaltis. An online database of nuclear electromagnetic moments. *Nuclear Instruments and Methods in Physics Research Section A: Accelerators, Spectrometers, Detectors and Associated Equipment*, 807:56–60, 2016. ISSN 0168–9002. doi: <http://dx.doi.org/10.1016/j.nima.2015.10.096>. URL <http://www.sciencedirect.com/science/article/pii/S0168900215013352>.
- [34] W. H. King. *Isotope Shifts in Atomic Spectra*. Springer US Imprint Springer, Boston, MA, 1984. ISBN 978-1-4899-1788-1.
- [35] L. V. Vormawah. *Collinear laser spectroscopy of scandium and yttrium isotopes at IGISOL IV*. PhD thesis, 2017. URL https://livrepository.liverpool.ac.uk/3009054/1/200564282_Aug2017.pdf.

-
- [36] P. Aufmuth, K. Heilig, and A. Steudel. Changes in mean-square nuclear charge radii from optical isotope shifts. *Atomic Data and Nuclear Data Tables*, 37(3):455 – 490, 1987. ISSN 0092-640X. doi: [https://doi.org/10.1016/0092-640X\(87\)90028-3](https://doi.org/10.1016/0092-640X(87)90028-3). URL <http://www.sciencedirect.com/science/article/pii/0092640X87900283>.
- [37] K. Chrysalidis et al. In-source laser spectroscopy of dysprosium isotopes at the isolde-rilis. *Nuclear Instruments and Methods in Physics Research Section B: Beam Interactions with Materials and Atoms*, 463:472–475, 2020. ISSN 0168-583X. doi: <https://doi.org/10.1016/j.nimb.2019.04.021>. URL <https://www.sciencedirect.com/science/article/pii/S0168583X19302058>.
- [38] P. Campbell. Lasers and photonics. Lecture notes, University of Manchester, 2017.
- [39] N.V. Vitanov, B.W. Shore, L. Yatsenko, K. Böhmer, T. Halfmann, T. Rickes, and K. Bergmann. Power broadening revisited: theory and experiment. *Optics Communications*, 199(1):117–126, 2001. ISSN 0030-4018. doi: [https://doi.org/10.1016/S0030-4018\(01\)01495-X](https://doi.org/10.1016/S0030-4018(01)01495-X). URL <https://www.sciencedirect.com/science/article/pii/S003040180101495X>.
- [40] Collisional Broadening. URL <https://sciencedemonstrations.fas.harvard.edu/presentations/collisional-broadening>.
- [41] P. Virtanen and SciPy 1.0 Contributors. SciPy 1.0: Fundamental Algorithms for Scientific Computing in Python. *Nature Methods*, 17:261–272, 2020. doi: [10.1038/s41592-019-0686-2](https://doi.org/10.1038/s41592-019-0686-2).
- [42] Á. Koszorús et al. Charge radii of exotic potassium isotopes challenge nuclear theory and the magic character of $N = 32$. *Nature Physics*, 2021. doi: [10.1038/s41567-020-01136-5](https://doi.org/10.1038/s41567-020-01136-5). URL <https://doi.org/10.1038/s41567-020-01136-5>.

-
- [43] M. Laatiaoui et al. Atom-at-a-time laser resonance ionization spectroscopy of nobelium. *Nature*, 538(7626):495–498, 2016. ISSN 0028-0836. doi: 10.1038/nature19345.
- [44] L. J. Vormawah et al. Isotope shifts from collinear laser spectroscopy of doubly charged yttrium isotopes. *Phys. Rev. A*, 97:042504, Apr 2018. doi: 10.1103/PhysRevA.97.042504. URL <https://link.aps.org/doi/10.1103/PhysRevA.97.042504>.
- [45] P. Karvonen, I.D. Moore, T. Sonoda, T. Kessler, H. Penttilä, K. Peräjärvi, P. Ronkanen, and J. Äystö. A sextupole ion beam guide to improve the efficiency and beam quality at IGISOL. *Nuclear Instruments and Methods in Physics Research Section B: Beam Interactions with Materials and Atoms*, 266(21):4794–4807, 2008. ISSN 0168-583X. doi: <https://doi.org/10.1016/j.nimb.2008.07.022>. URL <https://www.sciencedirect.com/science/article/pii/S0168583X08009191>.
- [46] M. Vilén et al. A new off-line ion source facility at IGISOL. *Nuclear Instruments and Methods in Physics Research Section B: Beam Interactions with Materials and Atoms*, 463:382–383, 2020. ISSN 0168-583X. doi: <https://doi.org/10.1016/j.nimb.2019.04.051>. URL <https://www.sciencedirect.com/science/article/pii/S0168583X19302344>.
- [47] R. G. Wilson. Surface ionization ion sources. *IEEE Transactions on Nuclear Science*, 14(3):72–74, 1967. doi: 10.1109/TNS.1967.4324525.
- [48] A. Nieminen et al. On-line ion cooling and bunching for collinear laser spectroscopy. *Phys. Rev. Lett.*, 88:094801, Feb 2002. doi: 10.1103/PhysRevLett.88.094801. URL <https://link.aps.org/doi/10.1103/PhysRevLett.88.094801>.
- [49] B. Cheal et al. Laser Spectroscopy of Niobium Fission Fragments: First Use of Optical Pumping in an Ion Beam Cooler Buncher. *Phys. Rev. Lett.*,

-
- 102:222501, Jun 2009. doi: 10.1103/PhysRevLett.102.222501. URL <https://link.aps.org/doi/10.1103/PhysRevLett.102.222501>.
- [50] R.P. de Groote et al. Upgrades to the collinear laser spectroscopy experiment at the IGISOL. *Nuclear Instruments and Methods in Physics Research Section B: Beam Interactions with Materials and Atoms*, 463:437 – 440, 2020. ISSN 0168-583X. doi: <https://doi.org/10.1016/j.nimb.2019.04.028>. URL <http://www.sciencedirect.com/science/article/pii/S0168583X19302125>.
- [51] M. Wang, G. Audi, F. G. Kondev, W.J. Huang, S. Naimi, and Xing Xu. The AME2016 atomic mass evaluation (II). tables, graphs and references. *Chinese Physics C*, 41(3):030003, mar 2017. doi: 10.1088/1674-1137/41/3/030003. URL <https://doi.org/10.1088/1674-1137/41/3/030003>.
- [52] Sirah Laser und Plasmatechnik GmbH. *Matisse User's Guide Version 1.10*.
- [53] R. Paschotta. Etalons. URL <https://www.rp-photonics.com/etalons.html>.
- [54] M. J. A. de Dood. Second Harmonic Generation, January 2006. URL http://users.uj.edu.pl/~ufdzierz/PracFot/SHG_Dood.pdf.
- [55] Spectra-Physics. WaveTrain 2 CW Frequency Doublers. URL <https://www.spectra-physics.com/f/wavetrain-2-cw-frequency-doubler>.
- [56] K. Baczynska et al. Nuclear spin determination of ^{100m}Y by collinear laser spectroscopy of optically pumped ions. *Journal of Physics G: Nuclear and Particle Physics*, 37(10):105103, jul 2010. doi: 10.1088/0954-3899/37/10/105103. URL <https://doi.org/10.1088/0954-3899/37/10/105103>.
- [57] J.-M. Régis et al. Abrupt shape transition at neutron number $N = 60$: $B(E2)$ values in $^{94,96,98}\text{Sr}$ from fast $\gamma - \gamma$ timing. *Phys. Rev. C*, 95:054319, May 2017.

-
- doi: 10.1103/PhysRevC.95.054319. URL <https://link.aps.org/doi/10.1103/PhysRevC.95.054319>.
- [58] A. de Roubin et al. Nuclear deformation in the $A \approx 100$ region: Comparison between new masses and mean-field predictions. *Phys. Rev. C*, 96:014310, Jul 2017. doi: 10.1103/PhysRevC.96.014310. URL <https://link.aps.org/doi/10.1103/PhysRevC.96.014310>.
- [59] J. E. García-Ramos and K. Heyde. Quest of shape coexistence in Zr isotopes. *Phys. Rev. C*, 100:044315, Oct 2019. doi: 10.1103/PhysRevC.100.044315. URL <https://link.aps.org/doi/10.1103/PhysRevC.100.044315>.
- [60] F. C. Charlwood et al. Nuclear charge radii of molybdenum fission fragments. *Physics Letters B*, 674(1):23 – 27, 2009. ISSN 0370-2693. doi: <https://doi.org/10.1016/j.physletb.2009.02.050>. URL <http://www.sciencedirect.com/science/article/pii/S0370269309002470>.
- [61] J. Dudouet et al. ${}^{96}_{36}\text{Kr}_{60}$ -Low-Z Boundary of the Island of Deformation at $N = 60$. *Phys. Rev. Lett.*, 118:162501, Apr 2017. doi: 10.1103/PhysRevLett.118.162501. URL <https://link.aps.org/doi/10.1103/PhysRevLett.118.162501>.
- [62] H. L. Thayer et al. Collinear laser spectroscopy of radioisotopes of zirconium. *Journal of Physics G: Nuclear and Particle Physics*, 29(9):2247–2262, aug 2003. doi: 10.1088/0954-3899/29/9/318. URL <https://doi.org/10.1088/0954-3899/29/9/318>.
- [63] W. Urban et al. Shape coexistence in the odd-odd nucleus ${}^{98}\text{Y}$: The role of the $g_{9/2}$ neutron extruder. *Phys. Rev. C*, 96:044333, Oct 2017. doi: 10.1103/PhysRevC.96.044333. URL <https://link.aps.org/doi/10.1103/PhysRevC.96.044333>.
- [64] B. Cheal et al. Laser spectroscopy of scandium isotopes across $N = 28$.

-
- [65] R.L. Kurucz and B. Bell. Atomic spectral line database. *Atomic Line Data Kurucz CD-ROM 23*. Cambridge, Mass. Smithsonian Astrophysical Observatory, 1995.
- [66] M. Kortelainen. Private Communication, 2021.
- [67] C. Wraith et al. Evolution of nuclear structure in neutron-rich odd-zn isotopes and isomers. *Physics Letters B*, 771:385–391, 2017. ISSN 0370-2693. doi: <https://doi.org/10.1016/j.physletb.2017.05.085>. URL <https://www.sciencedirect.com/science/article/pii/S0370269317304483>.
- [68] N. Mărginean et al. Shape coexistence at zero spin in ^{64}Ni driven by the monopole tensor interaction. *Phys. Rev. Lett.*, 125:102502, Sep 2020. doi: 10.1103/PhysRevLett.125.102502. URL <https://link.aps.org/doi/10.1103/PhysRevLett.125.102502>.
- [69] J. Suhonen and G. Lhersonneau. β decay of the 5^+ isomer of the odd-odd nucleus ^{100}Nb . *Phys. Rev. C*, 64:014315, Jun 2001. doi: 10.1103/PhysRevC.64.014315. URL <https://link.aps.org/doi/10.1103/PhysRevC.64.014315>.
- [70] S. Rinta-Antila et al. Decay study of neutron-rich zirconium isotopes employing a penning trap as a spectroscopy tool. *The European Physical Journal A*, 31(1):1–7, 2007. doi: 10.1140/epja/i2006-10158-9. URL <https://doi.org/10.1140/epja/i2006-10158-9>.
- [71] D. De Frenne. Nuclear Data Sheets for $A = 102$. *Nuclear Data Sheets*, 110(8):1745 – 1915, 2009. ISSN 0090-3752. doi: <https://doi.org/10.1016/j.nds.2009.06.002>. URL <http://www.sciencedirect.com/science/article/pii/S0090375209000581>.
- [72] S. Geldhof. *Developments for High-Resolution Laser Spectroscopy and Application to Palladium Isotopes*. PhD thesis, 2017. URL <https://jyx.jyu.fi/handle/123456789/68849?show=full>.

-
- [73] R. Orlandi et al. Single-particle and collective degrees of freedom in ^{101}Zr and $^{103,105}\text{Mo}$. *Phys. Rev. C*, 73:054310, May 2006. doi: 10.1103/PhysRevC.73.054310. URL <https://link.aps.org/doi/10.1103/PhysRevC.73.054310>.
- [74] G. Lhersonneau and others. Level structure of ^{99}Nb . *Phys. Rev. C*, 57:2974–2990, Jun 1998. doi: 10.1103/PhysRevC.57.2974. URL <https://link.aps.org/doi/10.1103/PhysRevC.57.2974>.
- [75] R. Rodríguez-Guzmán, P. Sarriguren, L.M. Robledo, and S. Perez-Martin. Charge radii and structural evolution in sr, zr, and mo isotopes. *Physics Letters B*, 691(4):202–207, 2010. ISSN 0370-2693. doi: <https://doi.org/10.1016/j.physletb.2010.06.035>. URL <https://www.sciencedirect.com/science/article/pii/S0370269310007926>.
- [76] M. Keim, E. Arnold, W. Borchers, U. Georg, A. Klein, R. Neugart, L. Vermeeren, R.E. Silverans, and P. Lievens. Laser-spectroscopy measurements of 72–96kr spins, moments and charge radii. *Nuclear Physics A*, 586(2):219–239, 1995. ISSN 0375-9474. doi: [https://doi.org/10.1016/0375-9474\(94\)00786-M](https://doi.org/10.1016/0375-9474(94)00786-M). URL <https://www.sciencedirect.com/science/article/pii/037594749400786M>.
- [77] F. Buchinger and others. Systematics of nuclear ground state properties in $^{78-100}\text{Sr}$ by laser spectroscopy. *Phys. Rev. C*, 41:2883–2897, Jun 1990. doi: 10.1103/PhysRevC.41.2883. URL <https://link.aps.org/doi/10.1103/PhysRevC.41.2883>.
- [78] C. Thibault et al. Hyperfine structure and isotope shift of the D_2 line of $^{76-98}\text{Rb}$ and some of their isomers. *Phys. Rev. C*, 23:2720–2729, Jun 1981. doi: 10.1103/PhysRevC.23.2720. URL <https://link.aps.org/doi/10.1103/PhysRevC.23.2720>.
- [79] I. Angeli and K.P. Marinova. Table of experimental nuclear ground state charge radii: An update. *Atomic Data and Nuclear Data Tables*, 99(1):

69–95, 2013. ISSN 0092-640X. doi: <https://doi.org/10.1016/j.adt.2011.12.006>. URL <https://www.sciencedirect.com/science/article/pii/S0092640X12000265>.

- [80] U. Hager et al. Precision mass measurements of neutron-rich yttrium and niobium isotopes. *Nuclear Physics A*, 793(1):20–39, 2007. ISSN 0375-9474. doi: <https://doi.org/10.1016/j.nuclphysa.2007.06.011>. URL <https://www.sciencedirect.com/science/article/pii/S0375947407006070>.
- [81] X.F. Yang et al. Collective structures in the Tc isotopes investigated with new, combined in-cooler and collinear laser spectroscopy.